AD-A078 987 CALIFORNIA UNIV BERKELEY DEPT OF MECHANICAL ENGINEERING F/G 13/8
RIGID-PLASTIC FINITE-ELEMENT ANALYSIS OF PLASTIC DEFORMATION IN--ETC(U)
AUG 79 C C CHEN , S KOBAYASHI F33615-77-C-5111
UNCLASSIFIED AFML-TR-79-4105 NL

1 OF 2
AD
A078987

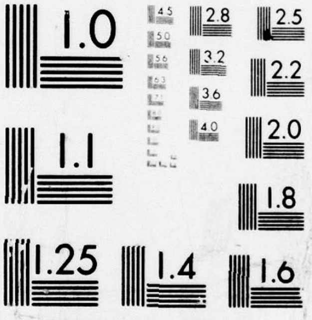

MICROCOPY RESOLUTION TEST CHART

NATIONAL BUREAU OF STANDARDS-1963-A

2

AFML-TR-79-4105

LEVEL II

RIGID-PLASTIC FINITE-ELEMENT ANALYSIS OF PLASTIC DEFORMATION IN METAL-FORMING PROCESSES

Mechanical Engineering
University of California
Berkeley, California

August 1979

TECHNICAL REPORT AFML-TR-79-4105
Technical Report May 1978-May 1979

Approved for public release; distribution unlimited.

AIR FORCE MATERIALS LABORATORY
AIR FORCE WRIGHT AERONAUTICAL LABORATORIES
AIR FORCE SYSTEMS COMMAND
WRIGHT-PATTERSON AIR FORCE BASE, OHIO 45433

NOTICE

When Government drawings, specifications, or other data are used for any purpose other than in connection with a definitely related Government procurement operation, the United States Government thereby incurs no responsibility nor any obligation whatsoever; and the fact that the Government may have formulated, furnished, or in any way supplied the said drawings, specifications, or other data, is not to be regarded by implication or otherwise as in any manner licensing the holder or any other person or corporation, or conveying any rights or permission to manufacture, use, or sell any patented invention that may in any way be related thereto.

This report has been reviewed by the Information Office (OI) and is releasable to the National Technical Information Service (NTIS). At NTIS, it will be available to the general public, including foreign nations.

This technical report has been reviewed and is approved for publication.

Harold L. Gegel

HAROLD L. GEGEL
Project Engineer

FOR THE COMMANDER

Henry C. Graham

HENRY C. GRAHAM
Acting Chief
Processing and High Temperature Materials Branch
Metals and Ceramics Division

"If your address has changed, if you wish to be removed from our mailing list, or if the addressee is no longer employed by your organization, please notify AFML/LLM ,W-PAFB, OH 45433 to help us maintain a current mailing list."

Copies of this report should not be returned unless return is required by security considerations, contractual obligations, or notice on a specific document.

UNCLASSIFIED

SECURITY CLASSIFICATION OF THIS PAGE (When Data Entered)

⑲ **REPORT DOCUMENTATION PAGE**	READ INSTRUCTIONS BEFORE COMPLETING FORM
1. REPORT NUMBER ⑱ AFML-TR-79-4105	2. GOVT ACCESSION NO.
	3. RECIPIENT'S CATALOG NUMBER
4. TITLE (and Subtitle) ⑥ RIGID-PLASTIC FINITE-ELEMENT ANALYSIS OF PLASTIC DEFORMATION IN METAL-FORMING PROCESSES,	⑨ 5. TYPE OF REPORT & PERIOD COVERED Technical Rep[redacted]t, May [redacted]78 - May [redacted]79,
	6. PERFORMING ORG. REPORT NUMBER
7. AUTHOR(s) ⑩ C. C. Chen [redacted] Shiro Kobayashi	8. CONTRACT OR GRANT NUMBER(s) ⑮ F33615-77-C-5111
9. PERFORMING ORGANIZATION NAME AND ADDRESS Department of Mechanical Engineering University of California Berkeley, California 94720	10. PROGRAM ELEMENT, PROJECT, TASK AREA & WORK UNIT NUMBERS 62102, 2418, 241804, ⑰ 04 ⑯ 24180406
11. CONTROLLING OFFICE NAME AND ADDRESS Air Force Materials Laboratory Air Force Systems Command Wright-Patterson Air Force Base, Ohio 45433	12. REPORT DATE ⑪ Aug[redacted]79
	13. NUMBER OF PAGES 131
14. MONITORING AGENCY NAME & ADDRESS(if different from Controlling Office) 400 426	15. SECURITY CLASS. (of this report) ⑫ 142
	15a. DECLASSIFICATION/DOWNGRADING SCHEDULE

16. DISTRIBUTION STATEMENT (of this Report)

Approved for public release; distribution unlimited.

17. DISTRIBUTION STATEMENT (of the abstract entered in Block 20, if different from Report)

18. SUPPLEMENTARY NOTES

19. KEY WORDS (Continue on reverse side if necessary and identify by block number)

Metal-forming processes, mechanics, closed-die forging, rigid-plastic analysis, ring compression

20. ABSTRACT (Continue on reverse side if necessary and identify by block number)

→ Metal-forming processes of extrusion, drawing, ring compression, and closed-die forging were analysed by the rigid-plastic finite-element method. According to the individual problem characteristics, the method was modified in order to deal with the steady-state configurations of the extrusion and drawing problems, the neutral flow point (or region) problems of ring compression, and the complexity in geometric changes of the closed-die forging problems. The present investigation is a complete study of the axisymmetric steady-state (continued) → over

DD FORM 1 JAN 73 1473 EDITION OF 1 NOV 65 IS OBSOLETE

SECURITY CLASSIFICATION OF THIS PAGE (When Data Entered)

400 426

extrusion and drawing processes, including multipass extrusion and drawing. Detailed deformation mechanics were revealed, showing the influence of the previous deformation history on the flow pattern in the current pass. To solve the neutral flow problems in ring compression, a variational formulation was developed for the case where the frictional stress is dependent on the relative velocity at the die-workpiece interface. The finite-element solutions of ring compression were then obtained under various friction conditions for several materials. Some of the results were compared with the approximate theoretical solutions and experimental results. It was concluded that this modified finite-element scheme does provide a useful tool for the analysis of neutral flow problems and for industrial applications. The closed-die forging problems are characterized by very complex geometries, large rigid portions, and rapid changes in velocity fields. Solutions for two extreme friction conditions (perfect lubrication and sticking) were obtained and compared with the experimental observations. The present work demonstrated the possibilities of solving the extremely complex problems by the rigid-plastic finite-element method.

PREFACE

This technical report covers the work performed under contract No. F33615-77-C-5111, from June 1, 1978 through May 30, 1979.

This project, with the University of California, Berkeley, California, was initiated under the project, "Mathematical Analysis of Metal-working Processes for Integrated Computer-aided Manufacturing," directed by Dr. Harold L. Gegel, LLM Air Force Materials Laboratory, Wright-Patterson Air Force Base, Ohio. Shiro Kobayashi, Professor of Mechanical Engineering, University of California, Berkeley, California, is the principal investigator.

TABLE OF CONTENTS

LIST OF ILLUSTRATIONS

LIST OF TABLES

Section I

INTRODUCTION

Metal-forming is a process in which the shape of a workpiece, consisting of a metal or its alloy, is altered into useful shapes, by using shaped dies under high pressure. The knowledge of the detailed deformation mechanics under various working conditions and the accurate determination of the forming load, as well as the values of stress and strain distributions, are extremely important to the proper design and control of forming processes. Because of large amounts of plastic deformation, the complexities in geometric changes, and the effects of the frictional force along the tool-workpiece interfaces, the exact mathematical closed-form solution for the metal-forming problem is usually very difficult to obtain, except for some special cases. Most of the closed-form solutions are therefore based on many assumptions, which may oversimplify the actual situations and limit their value in practical applications.

The closed-form solutions were usually made by one of the following methods [1], [2],* namely, Sach's [3], or slab, method; uniform deformation energy method [1], [4]; slip-line method [1], [2], [5], [6]; and bounding method [1], [2], [7], [8]. In the slab method, the homogeneous deformation, which states that the stresses only change in one direction and that the frictional constraint at the tool-workpiece interface does not affect the internal stress distribution, is assumed. The uniform

---

*Numbers in brackets correspond to the references listed at the end of this report.

deformation energy method calculates the average forming stress from plastic deformation by neglecting the redundant work involved in internal shearing processes due to nonuniform deformations. Both of these two methods can only provide the overall quantity, such as the forming load, but not the detailed stress and strain distributions. Furthermore, the assumption of homogeneous deformation oversimplifies the actual deformation pattern in most forming processes.

The first approach to the analysis of metal-working processes that did not assume homogeneous deformation was the slip-line method. This method permits a point-by-point calculation of stress for problems of plane-strain deformation in an idealized non-work-hardening rigid-plastic solid. Although the method provides information about local stress and velocity distributions, the method itself lacks uniqueness for constructing slip-line fields. Furthermore, the solutions are limited to rigid-perfectly plastic material under plane-strain forming conditions.

The bounding methods give estimated upper and lower limits of the required deformation force, according to kinematically admissible velocity fields (upper-bound) or statically admissible stress fields (lower-bound) provided for the forming processes. In order to have a mathematical closed-form solution, the provided admissible field must be mathematically expressible and the rigid-perfectly plastic material behavior is usually assumed. The construction of these admissible fields is usually very difficult, especially for geometrically complex forming processes. In addition, these methods lack the ability to efficiently deal with work-hardening materials and to reveal detailed deformation mechanics, such as the local stress and strain distributions.

In the last several years, due to rapid developments in computers, the closed-form solutions have become unnecessary, and various numerical techniques have been used for the analysis of metal-forming processes. The well-known finite-element methods [9], [10], [11] were applied to the problems of deformation in elastic-plastic solids for such processes as flat-punch indentation, upsetting, side pressing, and extrusion [12]-[16]. The elastic-plastic finite-element method offers many advantages in providing detailed deformation mechanics and in obtaining accurate solutions. Work-hardening material behavior and the interface friction constraint can also be treated efficiently by this method. In spite of the many advantages provided by this method, however, there still remain serious restrictions regarding computations. Since the method deals with elastic-plastic materials, elastic calculations are necessary at every step, as is constant checking to determine if any element, previously elastic, has reached the yielding stage. When an element reaches the yielding stage, the stiffness relations for that element change, thereby limiting increment size. Furthermore, the elastic-plastic property itself does not permit the use of large increments of deformation. Because of this requirement of small increments, the extensive computation time necessary to apply this method to metal-forming problems renders it cumbersome and uneconomical.

Recently, based on a variational principle similar to the upper-bound approach for rigid-plastic materials, Lee and Kobayashi [17] have developed a method called the rigid-plastic finite-element method (also called the matrix method). This method not only has all the advantages of the finite-element method, but it also permits large increments during deformation, therefore reducing computation time. Successful applications of this method were made, for example, in the prediction of workability in upsetting [18], [19] and the analysis of plane stress bore expanding [20]. Modifications of this method were made for sheet-metal problems in which large deformation and rotation are involved and the geometric nonlinearity cannot be neglected [21]. Parallel to the rigid-plastic finite-element method, based on a similar variational principle, Godbole and Zienkiewicz [25]-[27] and Price and Alexander [22]-[24] were able to solve the rigid-viscoplastic and viscous flow problems of plane-strain extrusion, compression, and flat-punch indentation.

To successfully apply the rigid-plastic finite-element method to the analyses of various forming processes, it requires suitable modifications according to the individual problem characteristics. An efficient method for dealing with the rigid elements inside the control volume is also required in order to avoid bad convergence characteristics. With a suitable choice of the convergence criterion, however, the computing time required to obtain the convergence solutions can also be reduced significantly. The present investigation is therefore aimed at improving and modifying this method to analyze various types of problems, such as steady-state problems of extrusion and drawing, neutral flow problems of ring compression, and the problems of complex geometric change in closed-die forging.

In this report, Section II discusses the minimum, or stationary value, principle and the methods of imbedding the incompressibility constraints for rigid-plastic materials. The boundary conditions along the die-workpiece interface and the methods of rigid-body treatment are also discussed. Section III describes the finite-element method and Newton-Raphson's iterative technique used in obtaining the minimum, or stationary value, solutions. Section IV investigates the deformation mechanics of the multipass steady-state extrusion and drawing processes, emphasizing the influence of the previous deformation history on the current metal flow.

In implementing the finite-element method for the analysis of metalworking problems, particular attention must be paid to boundary conditions. In upsetting, a part of an initially free surface comes into contact with the die during deformation. A similar situation occurs in sheet-metal forming. There is also a class of problems, such as ring compression and rolling. A unique feature of these kinds of problems is that there exists a point (or a region) along the die-workpiece interface where the velocity of the deforming material relative to the die velocity becomes zero (the problems of neutral flow point or region). The frictional stress usually changes its direction at the neutral flow point, but the lcoation of this point is not known a priori. In Section V, a variational formulation is developed for the case where the frictional stress is dependent on the relative velocity at the die-workpiece interface. This modified formulation is then used to analyze the ring compression problems.

The closed-die forging process is an extremely difficult problem because of the complex die geometries, the large rigid portions, and the rapid changes in velocity field during deformations. In Section VI, the rigid-plastic finite-element method is applied, with further modifications, to analyze these extremely complex problems.

Section II

PROBLEM FORMULATION

1. MINIMUM PRINCIPLE

The Cartesian coordinate is used to derive the minimum principle. Generalization of this formulation to other coordinate systems can be made without difficulty. A body of volume, V, is considered with the traction, $\underset{\sim}{F}$, prescribed on a part of the surface, S_F, and the velocity, $\underset{\sim}{V}$, prescribed on the remainder of the surface, S_U. The body is composed of a rigid-plastic material which obeys the von Mises yield criterion and its associated flow rule. Body forces are assumed to be absent. The actual stress (σ_{ij}) and velocity field ($\underset{\sim}{v}$) satisfy the following relations:

(a) Equilibrium conditions:

$$\sigma_{ij,j} = 0; \tag{1}$$

(b) Compatibility conditions:

$$\dot{\varepsilon}_{ij} = \frac{1}{2}(v_{i,j} + v_{j,i}) \tag{2}$$

and

$$\dot{\varepsilon}_v = v_{i,i} = 0;$$

(c) Stress-strain rate relationship:

$$\sigma'_{ij} = \frac{2}{3}\frac{\bar{\sigma}}{\dot{\bar{\varepsilon}}}\dot{\varepsilon}_{ij}; \tag{3}$$

where σ'_{ij} are the deviatoric stresses, $\bar{\sigma}$ and $\dot{\bar{\varepsilon}}$ are the effective stress and the effective strain rates, respectively, and are defined by $\bar{\sigma} = \sqrt{\frac{3}{2}\sigma'_{ij}\sigma'_{ij}}$ and $\dot{\bar{\varepsilon}} = \sqrt{\frac{2}{3}\dot{\varepsilon}_{ij}\dot{\varepsilon}_{ij}}$.

(d) Boundary conditions:

$\sigma_{ij}n_i = F_j$ on S_F

$v_i = V_i$ on S_U

where $\underset{\sim}{n}$ is the unit outward normal to the corresponding surface.

Let $\underset{\sim}{v}^*$ be any admissible velocity field satisfying the volumetric constraint $\dot{\varepsilon}^*_v = 0$ and the prescribed velocity boundary conditions. Multiplication of the left-hand side of Eq. (1) by v^*_i and integration of this quantity over the whole volume gives the following virtual work principle:

$$\int_V \sigma_{ij}\dot{\varepsilon}^*_{ij}\, dV = \int_{S_F} F_i v^*_i\, dS + \int_{S_U} (\sigma_{ij}n_j)V_i\, dS, \tag{4}$$

where $\dot{\varepsilon}^*_{ij}$ are the strain rate components compatible with the admissible velocity field $\underset{\sim}{v}^*$. Note that in deriving Eq. (4) the divergence theorem is used.

The convexity and normality conditions of the yield surface provide the following inequality,

$$(\sigma^*_{ij} - \sigma_{ij})\dot{\varepsilon}^*_{ij} \geq 0, \tag{5}$$

where σ^*_{ij} are the stress components derived from the admissible velocity field $\underset{\sim}{v}^*$ through the stress-strain rate relationship (3), satisfying the yield criterion.

Because the volumetric constraint $\dot{\varepsilon}_v^* = 0$ is imposed on the admissible velocity field, the tensor product of the stress and strain rate is therefore equivalent to the product of effective stress and effective strain rate and is expressed by

$$\sigma_{ij}^* \dot{\varepsilon}_{ij}^* = \bar{\sigma}\dot{\bar{\varepsilon}}^* . \tag{6}$$

Substitution of Eqs. (6) and (5) into Eq. (4) gives the following inequality:

$$\int_V \bar{\sigma}\, \dot{\bar{\varepsilon}}^*\, dV - \int_{S_F} \underset{\sim}{F} \cdot \underset{\sim}{v}^*\, dS \geq \int_{S_U} (\sigma_{ij} n_j) V_i\, dS, \tag{7}$$

where the equality holds only if $\sigma_{ij}^* = \sigma_{ij}$, i.e., when the stress components correspond to the actual solutions. The functional ϕ defined by

$$\phi = \int_V \bar{\sigma}\, \dot{\bar{\varepsilon}}^*\, dV - \int_{S_F} \underset{\sim}{F} \cdot \underset{\sim}{v}^*\, dS \tag{8}$$

is therefore used for the finite-element formulation, which states that, among all admissible velocity fields $\underset{\sim}{v}^*$, the actual solution gives the minimum value of this functional ϕ.

This minimum principle is also found in the books by Hill [5] and Washizu [28] and has been used extensively in the analysis of metal-forming processes [17], [29]. As pointed out by Washizu [28] and Kobayashi, Lee, and Oh [30], the solution $\dot{\varepsilon}_{ij}^*$ obtained from the minimization of the functional (8) differs from the actual strain rate $\dot{\varepsilon}_{ij}$ by a scalar factor c (i.e., $\dot{\varepsilon}_{ij}^* = c\dot{\varepsilon}_{ij}$), if surface tractions are prescribed over the entire surface; and the solution σ_{ij}^* differs from the actual stress σ_{ij} by a uniform hydrostatic stress $\bar{p}$ (i.e., $\sigma_{ij}^* = \sigma_{ij} + \bar{p}\delta_{ij}$), if velocities are prescribed over the entire surface, or if a combination of tangential traction and normal velocity is prescribed over that surface.

Although the formulation above is still an upper-bound approach, the method used in obtaining the solution is quite different. The finite-element techniques used in the present analysis gives much more attractive results than those of classical upper-bound solutions. In the classical upper-bound predictions, an admissible velocity field is provided first. This admissible field must be mathematically expressible in order to have a mathematical closed-form solution. Although the provided velocity field may be verified experimentally, a reasonable mathematical representation of this velocity field is usually very difficult to obtain. In addition, the classical upper-bound solution lacks the ability in efficiently dealing with work-hardening materials; it also lacks the abilities in revealing the detailed deformation mechanics, such as the local stress and strain, and the die pressure distribution. These severe restrictions limit the value in the actual application of the classical upper-bound method. On the contrary, the present analysis makes use of the finite-element techniques to solve the functional (8) above; the volumetric constraint is removed by introducing the Lagrange multiplier or penalty function formulations (see Section II.4). Certain type of velocity distributions inside an element, in terms of surrounding nodal velocities, is presumed; but the nodal velocities themselves are obtained from the computational results directly. Work-hardening material behavior and frictional force between the die-workpiece interface can also be treated efficiently. Besides, this method also provices the details necessary for the proper design and control of the metal-working process.

2. RIGID-BODY TREATMENT

The minimum principle described in the previous section applies only if the entire body is deforming plastically and no rigid zone or unloading exists during the deformation process. In practical problems, however, situations do arise where the rigid zone, as well as rigid unloading, are involved. These rigid portions are characterized by the extremely small value of effective strain rate in comparison to that in the deforming body. If these portions are included within the control volume, V, the value of the first derivatives of the functional (8) cannot be uniquely determined because of the undefined value of the effective stress (Eq. (3)) when the effective strain rate approaches zero. Due to these undetermined derivatives, solutions are impossible to obtain, except for the case where the rigid portions are eliminated from the actual calculation. However, the rigid elimination technique is virtually inapplicable in most of the problems because of the difficulties in determining the rigid-plastic boundaries.

In an effort to eliminate the problem of the undetermined functional derivatives, the following method makes use of a limited value $\dot{\bar{\varepsilon}}_0$ (say, $\dot{\bar{\varepsilon}}_0 = 10^{-3}$) in Eq. (3) for all elements lying inside the rigid portions. Elements with the value of effective strain rate, $\dot{\bar{\varepsilon}}$, less than the assigned value, $\dot{\bar{\varepsilon}}_0$, are called near-rigid elements. These elements are not eliminated from the control volume during actual computations. The limited value, $\dot{\bar{\varepsilon}}_0$, assumed in the stress-strain relationship for these elements, is to ensure a unique value of the deviatoric stress. This presumptive stress-strain rate relationship is equivalent to the assumption of a Newtonian fluid-like material behavior for those elements lying inside the near-rigid portions and is expressed by

$$\sigma'_{ij} = \frac{2}{3}\frac{\bar{\sigma}}{\dot{\bar{\varepsilon}}_0}\dot{\varepsilon}_{ij} \qquad (\text{for } \dot{\bar{\varepsilon}} \le \dot{\bar{\varepsilon}}_0) , \tag{9}$$

where the slope, $\frac{2}{3}\frac{\bar{\sigma}}{\dot{\bar{\varepsilon}}_0}$, is a constant for each incremental step during deformations, with its magnitude depending on the magnitude of $\bar{\sigma}$, which varies from one step to another.

To derive a minimum principle suitable for these near-rigid elements at each incremental step, the inequality (10), instead of (5), is used, and is given by

$$\sigma^*_{ij}\dot{\varepsilon}^*_{ij} - 2\sigma_{ij}\dot{\varepsilon}^*_{ij} \ge -\sigma_{ij}\dot{\varepsilon}_{ij} \qquad (\text{for } \dot{\bar{\varepsilon}} \le \dot{\bar{\varepsilon}}_0) . \tag{10}$$

Substitution of Eqs. (10) and (4) into Eq. (6) gives the following energy relation, which is slightly different from the expression (7) and is expressed by

$$\int_V \frac{1}{2}\bar{\sigma}^*\dot{\bar{\varepsilon}}^*\, dV - \int_{S_F} F_i v^*_i\, dS \ge -\frac{1}{2}\int_V \sigma_{ij}\dot{\varepsilon}_{ij}\, dV + \int_{S_U} (\sigma_{ij}n_j)V_i\, dS . \tag{11}$$

Hence, with this modified stress-strain rate relationship, the functional to be minimized for the whole control volume, V, becomes

$$\phi = \begin{cases} \int_V \bar{\sigma}^*\dot{\bar{\varepsilon}}^*\, dV - \int_{S_F} \underset{\sim}{F}\cdot\underset{\sim}{v}^*\, dS \quad (\text{for } \dot{\bar{\varepsilon}} > \dot{\bar{\varepsilon}}_0) & (12a) \\ \int_V \frac{1}{2}\bar{\sigma}^*\dot{\bar{\varepsilon}}^*\, dV - \int_{S_F} \underset{\sim}{F}\cdot\underset{\sim}{v}^*\, dS \quad (\text{for } \dot{\bar{\varepsilon}} \le \dot{\bar{\varepsilon}}_0) & (12b) \end{cases}$$

The factor $\frac{1}{2}$ appears in the expression of the distortional energy (12b) for those near-rigid elements; this is due to the linear dependence of σ'_{ij} and $\dot{\varepsilon}_{ij}$. However, this factor disappears in the expression of its first derivatives with respect to $\underset{\sim}{v}^*$, and the second derivatives are only constants depending on $\bar{\sigma}$ and $\dot{\varepsilon}_0$.

This modified functional (12) was used in the present study. In problems such as extrusion and drawing, the near-rigid portion does not present much difficulty in obtaining the convergent solutions, since the boundary conditions are mainly velocities prescribed. For the forging problems, however, a large portion of force-free boundary is prescribed. This force-prescribed boundary, together with the large rigid portions, results in bad converging characteristics. The present method resolves this difficulty by means of a suitable selection of the $\dot{\varepsilon}_0$ value (say, $\dot{\varepsilon}_0 = 10^{-4}$ in extrusion and 10^{-3} in forging) and results in reliable solutions with fast convergence.

3. BOUNDARY CONDITIONS ALONG THE TOOL-WORKPIECE INTERFACE

In general, neither velocity nor force (including magnitude and direction) is prescribed along the tool-workpiece interface. This is because the direction of the frictional stress is opposite to the direction of the relative velocity between the workpiece and the die, and this relative velocity is not known a priori. However, situations exist, e.g., in extrusion and drawing, in which the direction of metal flow is well understood. This gives, in turn, the direction of the frictional stress. This class of problems can be solved if the magnitude of the frictional stress is given according to the well-known Columbus Law, expressed by

$$f = \mu p, \tag{12}$$

or the friction law of constant factor m, expressed by

$$f = mk, \qquad (k = \frac{\bar{\sigma}}{\sqrt{3}}), \tag{13}$$

where p is the die pressure and k is the shear yield stress. The tool-workpiece interface is treated as a force-prescribed boundary and the formulations in the sections above are readily applicable. For metal-forming problems, the friction law of Eq. (13) has been used extensively; examples are found in [29], [39], and [47].

For problems such as ring compression and rolling, the unknown direction of the relative velocity between the die-workpiece interface makes it extremely difficult to handle the boundary condition. A unique feature of this type of problem is that there exists a point (or a region) along the die-workpiece interface where the velocity of the deforming material relative to the die becomes zero (a neutral flow problem), and the location of this point (or region) depends on the magnitude of the frictional stress itself. To deal with these problems, a new variational formulation has been developed and successfully applied to the case of ring compression. The details of these new derivations will be discussed in Section V.

4. IMBEDDING OF THE INCOMPRESSIBILITY CONSTRAINT

The incompressibility condition, $\dot{\varepsilon}_v^* = 0$, imposed on the velocity fields can be removed by introducing either the Lagrange multiplier [17], [30], or a penalty function [31] into the functional ϕ (Eq. (8)). Note that the minimum principle becomes a stationary value problem if the Lagrange multiplier method is used. In order to avoid the confusion of the notations, the variable $\underset{\sim}{u}$ is assigned to represent any set of the arbitrary velocity fields which satisfies the velocity boundary conditions but not necessarily the incompressibility constraint. With this velocity field, the modified functionals are then stated as

$$\phi_1 = \int_V \bar{\sigma}\dot{\bar{\varepsilon}}\, dV + \int_V \lambda\dot{\varepsilon}_v\, dV - \int_{S_F} \underset{\sim}{F}\cdot\underset{\sim}{u}\, dS \tag{14}$$

for the Lagrange multiplier method, where λ is the Lagrange multiplier, and

$$\phi_2 = \int_V \bar{\sigma}\dot{\bar{\varepsilon}}\, dV + \int_V \frac{\zeta}{2}\dot{\varepsilon}_v^2\, dV - \int_{S_F} \underset{\sim}{F}\cdot\underset{\sim}{u}\, dS \tag{15}$$

for the penalty function constraint, where ζ is a large positive constant (say, $\zeta = 10^6$). The stress and strain rate components (σ_{ij} and $\dot{\varepsilon}_{ij}$) are derived from the velocity field $\underset{\sim}{u}$.

Physical interpretations of the individual terms of the equations above can be made in terms of distortion, dilatation, and input energy, respectively. It can also be shown [30] that when the velocity u corresponds to the actual one, the value of the Lagrange multiplier is equivalent to the value of mean stress and is expressed by

$$\lambda = \sigma_m = \frac{1}{3}\sigma_{ii} \, . \tag{16}$$

Comparing the variations of the functionals ϕ_1 and ϕ_2, the penalty function approach can also provide the mean stress, if the velocity $\underset{\sim}{u}$ obtained from the minimum value of ϕ_2 is identical to that obtained from the stationary value of ϕ_1, and this mean stress is given by

$$\zeta\dot{\varepsilon}_v = \lambda = \sigma_m \, . \tag{17}$$

Both approaches have advantages and disadvantages, as follows: (i) For the Lagrange method, the additional unknown λ is introduced and, if a large number of elements is used in the finite-element discretization, this additional unknown will result in a large bandwidth for the stiffness matrix and also requires considerable amounts of computing time to solve the equation; (ii) For the penalty approach, although the additional unknown is avoided in the problem formulation, the system of equations may become ill-conditioned when a bad initial guess is provided, giving a very large value of $\zeta\dot{\varepsilon}_v$. It is suggested, therefore, to use the upper-bound velocity distribution as an initial guess, if available.

For a four-nodal quadrilateral element which is used in the finite-element discretization, it is shown (see Section III.5) that the volumetric strain rate $\dot{\varepsilon}_v$ is linearly distributed inside that element. It can be shown further, for the case of plane stress or plane strain, that the incompressibility constraint, $\int_V \dot{\varepsilon}_v \, dV = 0$, can always be achieved if the volumetric strain rate is varying linearly from positive to negative with a zero value at the center of the element, without any restriction on its slope. The penalty function constraint, $\int_V \dot{\varepsilon}_v^2 \, dV$, on the other hand, requires the value of $\dot{\varepsilon}_v$ to be zero at every internal point of the element because of the square quantity, $\dot{\varepsilon}_v^2$, of the integrand. Consequently, due to this over-constraint requirement, an incorrect solution may result, if the penalty function (15) is applied without suitable modifications. The well-known "reduced integration" has been proved to be successful in dealing with the penalty term for the cases of plane stress and plane strain and for three-dimensional problems [9]. This reduced integration releases the over-constraint conditions by the method of reducing the integration points in numerical evaluation of the integral, $\int_V \dot{\varepsilon}_v^2 \, dV$. For example, the 2×2 numerical integration is reduced to one-point numerical integration for the cases of two-dimensional plane problems; the only condition required to satisfy the volumetric constraint is the requirement of the zero $\dot{\varepsilon}_v$ at the integration point (i.e., the centroid of the element), but not necessary at other points (see Section III.5). It can also be shown that the reduced one-point integration, evaluated at the centroid of the element, gives the exact evaluation of the integral, $\int_V \dot{\varepsilon}_v \, dV$ for cases of plane stress and plane strain, but not for axisymmetric cases. Nevertheless, the over-constraint conditions in axisymmetric problems can also be removed by the method of reduced integration, although the exact evaluation of the integral, $\int_V \dot{\varepsilon}_v \, dV$ is not attainable from this reduced integration.

A slight modification of the penalty term can also provide the desired solutions without employing the reduced integration. This modified penalty form is stated as

$$\phi_3 = \int_V \bar{\sigma}\dot{\bar{\varepsilon}} \, dV + \frac{\zeta}{2V} \left[\int_V \dot{\varepsilon}_v \, dV\right]^2 - \int_{S_F} \underset{\sim}{F} \cdot \underset{\sim}{u} \, dS \tag{18}$$

and, when the admissible velocity field corresponds to the actual one, the mean stress is given by

$$\sigma_m = \lambda = \frac{\zeta}{V} \int_V \dot{\varepsilon}_v \, dV. \tag{19}$$

Note that, in Eq. (19), the mean stress is assumed to be uniform over each element as that assumed for the Lagrange multiplier approach. Comparison of Eqs. (19) and (17) gives the facts that the present modification is made by assuming the average volumetric strain rate

$$\dot{\varepsilon}_v^{ave} = \frac{1}{V} \int_V \dot{\varepsilon}_v \, dV \tag{20}$$

and by substitution of this average value into Eq. (15). The square outside the integral $\int_V \dot{\varepsilon}_v \, dV$ makes the formulation free from the possibilities of over-constraint and renders this formulation successful in application to any problem.

In the present investigations, the Lagrange multiplier method (14) is applied to the problems of ring compression; the modified penalty approach (18) is used in the analysis of multipass extrusion and drawing and forging problems. Further details in terms of finite-element discretization are given in Section III.

Section III

METHOD OF SOLUTION--THE FINITE-ELEMENT APPROACH

1. METHOD OF APPROACH

General theories of the finite-element method have been well described in many books (for example, Zienkiewicz [9], Strang and Fix [10], Bathe and Wilson [32]). These finite-element techniques were applied to the present minimum or stationary value problems for rigid-plastic work-hardening materials with the functionals as given in Section II. The method is briefly described as follows.

Let the functional $\phi(\underset{\sim}{w})$ represent a given volume integral with its value evaluated over the whole body, V. The body, V, is divided into M elements interconnected at N nodal points. The value of the functional, $\phi(\underset{\sim}{w})$, may be written as

$$\phi = \sum_{m=1}^{M} \bar{\phi}^{(m)}(\underset{\sim}{w}), \tag{21}$$

where $\bar{\phi}^{(m)}(\underset{\sim}{w})$ represents the same integral but evaluated at the m-th element. Inside this element the variables, $\underset{\sim}{w}$, are approximated by a linear combination of certain shape functions, $N_\alpha'^{(*)}$ such that

$$\underset{\sim}{w} \simeq \sum_{\alpha} N'_\alpha w'_\alpha, \tag{22}$$

where the unknown coefficients $\underset{\sim}{w}'_\alpha$ may be explained as the values of the variables $\underset{\sim}{w}$ at nodal point α, and are called nodal variables. (These

---

(*) Hereafter, the Greek indices ($\alpha,\beta,\ldots$,etc.) are reserved to denote the surrounding nodal points or their associated variables at the elemental level.

nodal unknowns may represent displacements, velocities, temperature, etc., depending on the type of the problem). Substitution of Eq. (22) into Eq. (21) gives the approximation of the functional ϕ by

$$\phi \simeq \sum_{m=1}^{M} \tilde{\phi}^{(m)}(\underset{\sim}{w}'_{\alpha}) , \qquad (23)$$

which depends on the nodal point variables $\underset{\sim}{w}'_{\alpha}$ only.

If $\bar{w}_i$ ($i = 1,\ldots,N \times p$; N = total nodals, p = number of unknowns to each nodal) denote the unknowns of the nodal variables ($\underset{\sim}{w}_{\alpha}$) in the global system after assembly, the functional ϕ in Eq. (23) can then be replaced by

$$\phi \simeq \phi(\bar{w}_i) \qquad (i = 1,\ldots,N \times p). \qquad (24)$$

Thus, the discretization procedures change the original stationary value problem of the functional ϕ, with respect to $\underset{\sim}{w}$ to the problem of the functional Φ with respect to nodal variables w_i.

To find the minimum or stationary value of the functional Φ of Eq. (24), the following system of equations must be solved:

$$\frac{\partial\Phi(\bar{w}_i)}{\partial\bar{w}_j} = 0 \qquad (j = 1,\ldots,N \times p). \qquad (25)$$

If this system of equations is linear, it is then possible to write Eq. (25) in terms of the following matrix representation:

$$[\bar{K}_{ij}]\{\bar{w}_j\} = \{\bar{f}_i\}, \qquad (26)$$

where $[\bar{K}_{ij}]$, known as the stiffness matrix, is independent of $\bar{w}_j$; and $\{\bar{f}_i\}$ is the nodal force vector. The matrix $[\bar{K}_{ij}]$ is usually a banded symmetric matrix in most solid mechanics problems. For these cases, only the upper half of the elements of matrix $[\tilde{K}_{ij}]$ are actually required during computation, due to the symmetric property; and these elements can be arranged and stored in a square array inside the computer, due to the banded property. The Gaussian elimination and backward substitution techniques are normally used in solving the equations above (26).

If the elements of the stiffness matrix $[\tilde{K}_{ij}]$ are functions of the nodal variable $\bar{w}_i$, the system (25) is then called nonlinear. All the functionals given in Section II belong to this type of problem. Normally, it requires more effort to solve the nonlinear problems than the linear ones. Most of the methods rely on the iterative techniques [33], [34]. although the convergence character, during iterations, depends very much on the functional behavior itself, the well-known Newton-Raphson iterative method has been extensively used due to its simplicity and the quadratic convergence character.

With the assumptions of the existence and continuity of the derivatives, the value of $\frac{\partial\Phi}{\partial\bar{w}_i}$ evaluated at an arbitrary point $\bar{w}_k(n)$ can be written as the following series representation by virtue of Taylor's expansion:

$$\left.\frac{\partial\Phi}{\partial\bar{w}_i}\right|_{\bar{w}_k(n)} = \left.\frac{\partial\Phi}{\partial\bar{w}_i}\right|_{\bar{w}_k(n-1)} + \left.\frac{\partial^2\Phi}{\partial\bar{w}_i\cdot\partial\bar{w}_j}\right|_{\bar{w}_k(n-1)} \Delta\bar{w}_{j(n)} + \cdots ; \qquad (27)$$

$$\Delta\bar{w}_j(n) = \bar{w}_j(n) - \bar{w}_j(n-1),$$

where $\bar{w}_j(n-1)$ denotes some other reference point. If $\Delta\bar{w}_j$ are small enough, $(\Delta\bar{w}_j)^2$ and all other higher-order terms can then be neglected; and if the value of the left-hand side of Eq. (27) is very near zero, the quantities can then be calculated from the following relation:

$$\left.\frac{\partial^2 \Phi}{\partial \bar{w}_i \, \partial \bar{w}_j}\right|_{\bar{w}_{k(n-1)}} \Delta \bar{w}_{j(n)} = -\left.\frac{\partial \Phi}{\partial \bar{w}_i}\right|_{\bar{w}_{k(n-1)}} . \tag{28}$$

Eq. (28) is used for the Newton-Raphson iterative technique, in which $\bar{w}_{k(n-1)}$ represent the input values obtained from the previous solution, and $\Delta\bar{w}_j(n)$ represent the correction values obtained from the present iteration. In order to avoid the possible divergent solutions, a deceleration coefficient η is usually assigned such that

$$\bar{w}_{k(n)} = \bar{w}_{k(n-1)} + \eta \Delta \bar{w}_{k(n)} . \tag{29}$$

The value of η is normally restricted to $0 < \eta \leq 1$; it may be selected as large as possible if the functional is well behaved. Thus, once an initial guess $\bar{w}_{k(0)}$ is provided, the iterative relations of Eqs. (28) and (29) are then used to obtain an improved solution; this procedure is performed repeatedly until the desired accuracy is achieved. Note that some restrictions for the tangent matrix, $[\frac{\partial^2 \Phi}{\partial \bar{w}_i \partial \bar{w}_j}]$, are required in order to assure the existence and uniqueness of the solution. Further discussions on this aspect can be found in some references (e.g., [35]).

2. CONVERGENCE REQUIREMENT

In order to ensure the convergence of the obtained solutions during iterative processes, the solution must be checked at every iteration to satisfy certain requirements according to a convergence criterion. Since the new solution is controlled by the size of the deceleration coefficient η (Eq. (29)), the provided criterion should also be capable of determining an optimal value of the deceleration coefficient in order to have fast convergence and, hence, reduce the computing time. Unfortunately, no such criterion is available at the present time, although efforts have been made to establish one in the past years. Instead, the following convergence criteria are often used in measuring the convergence of solutions.

In the previous studies [17]-[21], [29], the convergence of the solution has been measured by the quantity $\|\Delta\underset{\sim}{\bar{w}}\|/\|\underset{\sim}{\bar{w}}\|$, where the Euclidean vector norm is defined by

$$\|\underset{\sim}{\bar{w}}\| = \sqrt{\sum_{i=1}^{N\times p} \bar{w}_i^2} \; , \tag{30}$$

where N = total number of nodal points and p = number of unknowns to each node. The deceleration coefficient is assigned to be a constant and the convergence criterion requires that the error norm at the n-th iteration $(\|\Delta\underset{\sim}{\bar{w}}_{(n)}\|/\|\underset{\sim}{\bar{w}}_{(n-1)}\|)$ be less than that at the previous iteration. This convergence criterion, with a suitable selection of the deceleration coefficient, has worked out well for the solutions in previous studies. However, it was found that a divergent solution may be indicated according to this criterion for a function which is not well behaved, although the solution is converging in its true sense. In this case, the criterion resulted in the use of unnecessarily small values of the deceleration coefficient and thus increased computing time.

Instead of the measurement defined by (30), the quantity g defined by

$$g = \sqrt{\sum_{i=1}^{N\times p} \left(\frac{\partial\Phi}{\partial\bar{w}_i}\right)^2} \tag{31}$$

can also be utilized to indicate the convergence by requiring the value of g evaluated at the present solution (Eq. (29)) be less than that of the previous one. The convergence of the obtained solutions is then measured by either of these two criteria (Eqs. (30) and (31)). It was found that a combination of these two criteria does provide an adequate indication of convergence, and the value of deceleration coefficient can also be selected efficiently, according to the previous information of the functional behavior and the convergence requirement at the current iteration.

For the case where the initial guess is far from the actual one, the convergence requirement by $\|\Delta \underset{\sim}{\bar{w}}\| / \|\underset{\sim}{\bar{w}}\|$ is very helpful in preventing the possible diverging solutions. However, once the obtained iterative solution is very close to the actual one (say, $g \leq 0.5$), the measurement by Eq. (31) and its convergence requirement can provide very useful information in selecting an efficient value of the deceleration coefficient, and, therefore, provide fast convergence. Note that situations may still happen in which the new solution obtained does not satisfy any of the criteria above, especially when a very bad initial guess is provided. This difficulty can be resolved by either changing the initial guess or by using other iterative techniques (for example, the steepest descent method [36], damped Newton-Raphson method [33], or the conjugate gradient method [37], [38]). Nevertheless, it was found that, in many cases, the bad convergence characteristics are often due to the improper formulation itself rather than the choice of the iterative technique. This improper formulation includes, for example, the undefined value of the frictional stress (Eq. (13)) for the neutral region along the die-workpiece interface for the ring compression case, and the undefined value of the deviatoric stresses in Eq. (3) with near-zero effective strain rate when the control volume contains rigid portions. The necessary modifications for the neutral region problem will be discussed later in Section V. The method of rigid treatment has been proposed in Section II.2. Both new formulations were employed in the present investigations and the convergent solutions were therefore obtained without difficulty.

3. DISCRETIZATION FORMULATIONS FOR AXISYMMETRIC AND PLANE-STRAIN CASES

In the present investigations, the nonlinear stationary value of the functional ϕ_1 (Eq. (14)) for the Lagrange multiplier and the minimization of the functional ϕ_2 (Eq. (15)); or ϕ_3, (Eq. (18)) for the penalty constraint were solved by the finite-element method and the iterative technique, as described in the two sections above. The procedures start with the approximation of the functionals above by Eq. (33). Let $\pi_1^{(m)}$, $\pi_2^{(m)}$, $\pi_3^{(m)}$, $\pi_F^{(m)}$ be the integrals defined by (32), which correspond to distortional energy, dilatational energy of the Lagrange form, the penalty form, and input energy, respectively. All these integrals are evaluated at typical element m. These integrals are expressed by

$$\begin{aligned}
\pi_1^{(m)} &= \int_{V^{(m)}} \bar{\sigma}\dot{\bar{\varepsilon}}\, dV, \\
\pi_2^{(m)} &= \int_{V^{(m)}} \lambda\dot{\varepsilon}_v\, dV = \lambda^{(m)}\pi_v^{(m)}; \quad \pi_v^{(m)} = \int_{V^{(m)}} \dot{\varepsilon}_v\, dV, \\
\pi_3^{(m)} &= \int_{V^{(m)}} \frac{\zeta}{2}\dot{\varepsilon}_v^2\, dV, \\
\pi_F^{(m)} &= \int_{S^{(m)}} \underset{\sim}{F}\cdot\underset{\sim}{u}\, dS.
\end{aligned} \tag{32}$$

where $V^{(m)}$ denotes the volume of the m-th element and $S^{(m)}$ denotes the corresponding surface where the surface traction is prescribed. Note that the mean stress λ in Eq. (32) is assumed to be uniform ($\lambda = \lambda^{(m)}$) over the entire element. The functionals ϕ_1, ϕ_2, and ϕ_3 are then approximated by

$$\phi_1 \simeq \sum_{m=1}^{M} [\pi_1^{(m)} + \lambda^{(m)}\pi_V^{(m)} - \pi_F^{(m)}], \quad \text{(Lagrange multiplier method)}$$

$$\phi_2 \simeq \sum_{M=1} [\pi_1^{(m)} + \pi_3^{(m)} - \pi_F^{(m)}], \quad \text{(Penalty constraint)} \qquad (33)$$

$$\phi_3 \simeq \sum_{m=1}^{M} [\pi_1^{(m)} + \frac{\zeta}{2V^{(m)}} (\pi_V^{(m)})^2 - \pi_F^{(m)}], \quad \text{(Modified penalty constraint)}$$

where M is the total number of elements.

For the functional ϕ_1 the independent variables are the nodal point velocities u_α (see Eq. (41)) and the element mean stress $\lambda^{(m)}$; the system of equations to be solved at the n-th iteration for the Newton-Raphson iterative method is then given by

$$\left[\begin{array}{c|c} \sum\limits_{m=1}^{M} \{\frac{\partial^2}{\partial u_\alpha \partial u_\beta}[\pi_1^{(m)} - \pi_F^{(m)}]\} & \sum\limits_{m=1}^{M} \{\frac{\partial}{\partial u_\alpha} \pi_V^{(m)}\} \\ \hline \sum\limits_{m=1}^{M} \{\frac{\partial}{\partial u_\beta} \pi_V^{(m)}\} & 0 \end{array}\right]_{(n-1)} \left\{\begin{array}{c} \Delta u_\beta \\ \hline \lambda^{(m)} \end{array}\right\}_{(n)} \qquad (34)$$

$$= \left\{\begin{array}{c} -\sum\limits_{m=1}^{M} \{\frac{\partial}{\partial u_\alpha}[\pi_1^{(m)} - \pi_F^{(m)}]\} \\ \hline -\sum\limits_{m=1}^{M} \pi_V^{(m)} \end{array}\right\}_{(n-1)}$$

In Eq. (34) the tangent matrix is banded and symmetric; the components of this matrix, as well as the left-hand side vector of Eq. (34), involve only the nodal point velocities. Hence, only the initial guess of the velocity field $u_{\alpha(0)}$ is required to start the first iteration; the value of the Lagrange multiplier (i.e., mean stress) can be obtained from the results of iterations.

For the penalty constraint of the functional ϕ_2, because the unknowns are nodal point velocities only, the system of equations to be solved for the n-th iteration is

$$\sum_{m=1}^{M} \left\{\frac{\partial^2}{\partial u_\alpha \partial u_\beta}\left(\pi_1^{(m)} + \pi_3^{(m)} - \pi_4^{(m)}\right)\right\}_{(n-1)} \cdot \Delta u_{\beta(n)} = -\sum_{m=1}^{M} \left\{\frac{\partial}{\partial u_\alpha}\left(\pi_1^{(m)} + \pi_3^{(m)} - \pi_4^{(m)}\right)\right\}. \tag{35}$$

The expression for the functional ϕ_3 is similar to Eq. (34), and is therefore omitted. Note that the summations ($\sum_{m=1}^{M}$) in Eqs. (34) and (35) denote the proper assembling procedure by adding together all components corresponding to the same unknown.

The following discretization formulations are made at the elemental level for axisymmetric cases, in which a four-nodal quadrilateral element is considered. The necessary modifications of these formulas for plane-strain cases will be discussed later. The actual coordinate system (r, z) for a typical element is transformed into a natural coordinate system (s, t), as shown in Fig. 1. This natural coordinate system is defined in a way such that s and t vary from -1 to 1 within each element. An arbitrary point (r, z) inside the element can therefore be expressed in terms of the natural coordinate (s, t) as follows:

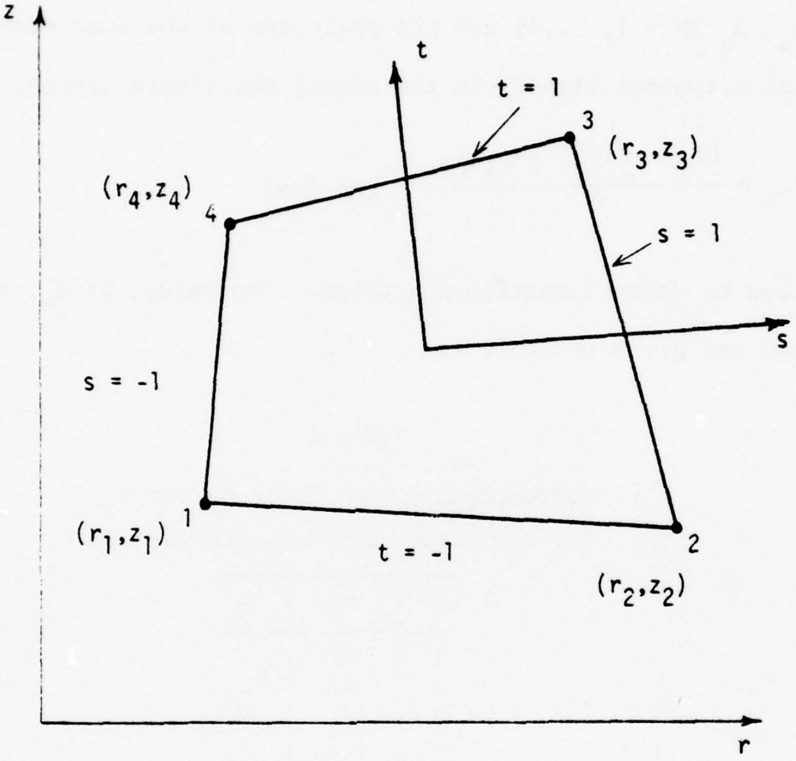

Fig. 1 Quadrilateral element and natural coordinate system.

$$r(s,t) = \sum_{\alpha=1}^{4} q_\alpha r_\alpha \; ; \tag{36}$$

$$z(s,t) = \sum_{\alpha=1}^{4} q_\alpha z_\alpha \; , \tag{37}$$

where r_α, z_α ($\alpha = 1,\ldots,4$) are the positions of the four surrounding nodal points of a typical element in the actual coordinate system; and

$$q_\alpha = \frac{(1 + s_\alpha s)(1 + t_\alpha t)}{4} \qquad \text{(no sum)} \tag{38}$$

are called the transformation functions. The values of s_α, t_α are tabulated and given in Table 1.

Table 1

Corresponding values of s_α and t_α for the coordinate transformattion

α	s_α	t_α
1	-1	-1
2	+1	-1
3	+1	+1
4	-1	+1

With the assumption of bilinear distributed velocity fields, the radial and axial velocity components u_r, u_z at any arbitrary point inside the element can then be determined in terms of the surrounding nodal velocities. This is expressed by $\underset{\sim}{u} = \sum_{\alpha=1}^{4} N'_\alpha \underset{\sim}{u}'_\alpha$ (Eq. (22)), or, with suitable arrangement of the representation, expressed by

$$u_i = \sum_{\alpha=1}^{8} N_{i\alpha} u_\alpha \qquad (i = 1,2), \tag{39}$$

where the vector $\{u_i\}$ and $\{u_\alpha\}$ are defined by, respectively,

$$\{u_i\}^T = \{u_r, u_z\}, \tag{40}$$

and

$$\{u_\alpha\}^T = \{u_{r_1}, u_{z_1}, u_{r_2}, u_{z_2}, u_{r_3}, u_{z_3}, u_{r_4}, u_{z_4}\}; \tag{41}$$

and the shape function $[N_{i\alpha}]$ is defined by

$$[N_{i\alpha}] = \begin{bmatrix} q_1, & 0, & q_2, & 0, & q_3, & 0, & q_4, & 0 \\ 0, & q_1, & 0, & q_2, & 0, & q_3, & 0, & q_4 \end{bmatrix}. \tag{42}$$

The Greek index α denotes the appropriate surrounding nodal point variables at the elemental level, as mentioned before.

The stress and strain components in Eqs. (3) and (8) can be represented by the proper vector forms, such that

$$\dot{\bar{\varepsilon}} = \sqrt{\frac{2}{3}\dot{\underset{\sim}{\varepsilon}}\cdot\dot{\underset{\sim}{\varepsilon}}}\ , \tag{43}$$

and

$$\bar{\sigma} = \sqrt{\frac{3}{2}\underset{\sim}{\sigma}'\cdot\underset{\sim}{\sigma}'}\ , \tag{44}$$

where the corresponding values of the vector representations are given by

$$\dot{\varepsilon}_i = A_{ij}u_j\ , \tag{45}$$

and

$$\dot{\sigma}'_i = \frac{3}{2}\,\frac{\bar{\sigma}}{\dot{\bar{\varepsilon}}}\,\dot{\varepsilon}_i\ , \tag{46}$$

where $[A_{ij}]$ is the appropriate matrix representation of the differential operator acting on the velocity component $\{u_j\}$. For axisymmetric cases,

$\{u_j\}^T = \{u_r, r_z\}$, the components of $\{\dot{\varepsilon}_i\}$, $\{\sigma_i'\}$, and $[A_{ij}]$ are defined by

$$\{\dot{\varepsilon}_i\}^T = \{\dot{\varepsilon}_r, \dot{\varepsilon}_z, \dot{\varepsilon}_\theta, \sqrt{2}\dot{\varepsilon}_{rz}\}, \tag{47}$$

$$\{\sigma_i'\}^T = \{\sigma_r', \sigma_z', \sigma_\theta', \sqrt{2}\sigma_{rz}\}, \tag{48}$$

and

$$[A_{ij}] = \begin{bmatrix} \frac{\partial}{\partial r} & 0 \\ 0 & \frac{\partial}{\partial z} \\ \frac{1}{r} & 0 \\ \frac{1}{\sqrt{2}}\frac{\partial}{\partial z} & \frac{1}{\sqrt{2}}\frac{\partial}{\partial r} \end{bmatrix} . \tag{49}$$

For convenience, the appropriate vector representation of the Kronecker delta is used for the volumetric strain rate, such that

$$\dot{\varepsilon}_v = \underset{\sim}{C} \cdot \underset{\sim}{\varepsilon}, \tag{50}$$

where the Kronecker delta C is defined by

$$\{\underset{\sim}{C}\}^T = \{1,1,1,0\}. \tag{51}$$

By substituting the expression (40) for u_r and u_z into Eq. (45), the strain-rate vector is then expressible in terms of the surrounding nodal point velocities and is given by

$$\dot{\varepsilon}_i = B_{i\alpha} u_\alpha \text{ ,} \tag{52}$$

and

$$B_{i\alpha} = A_{ij} N_{j\alpha} \tag{53}$$

is the corresponding matrix representation of the differential operator $\underline{A}$ acting on the shape function $\underline{N}$. Results of these differentiations are obtained, with the help of the chain rule, by converting the differentiations from the (r, z) coordinate to the (s, t) coordinate according to the following relationship:

$$\begin{Bmatrix} \frac{\partial}{\partial r} \\ \frac{\partial}{\partial z} \end{Bmatrix} = \frac{1}{|J|} \begin{bmatrix} \frac{\partial z}{\partial t} & -\frac{\partial z}{\partial s} \\ -\frac{\partial r}{\partial t} & \frac{\partial r}{\partial s} \end{bmatrix} \begin{Bmatrix} \frac{\partial}{\partial s} \\ \frac{\partial}{\partial t} \end{Bmatrix} , \tag{54}$$

where J is the determinant of the Jacobian of the coordinate transformation and is expressed by

$$|J| = \frac{\partial r}{\partial s} \cdot \frac{\partial z}{\partial t} - \frac{\partial r}{\partial t} \cdot \frac{\partial z}{\partial s} . \tag{55}$$

After carrying out the detailed calculation, the values of the matrix $\underline{B}$ are obtained as follows:

$$[B_{i\alpha}] = \begin{bmatrix} Y_1 & 0 & Y_2 & 0 & Y_3 & 0 & Y_4 & 0 \\ 0 & X_1 & 0 & X_2 & 0 & X_3 & 0 & X_4 \\ G_1 & 0 & G_2 & 0 & G_3 & 0 & G_4 & 0 \\ \frac{1}{\sqrt{2}} X_1 & \frac{1}{\sqrt{2}} Y_1 & \frac{1}{\sqrt{2}} X_2 & \frac{1}{\sqrt{2}} Y_2 & \frac{1}{\sqrt{2}} X_3 & \frac{1}{\sqrt{2}} Y_3 & \frac{1}{\sqrt{2}} X_4 & \frac{1}{\sqrt{2}} Y_4 \end{bmatrix} \tag{56}$$

with

$$\begin{Bmatrix} X_1 \\ X_2 \\ X_3 \\ X_4 \end{Bmatrix} = \frac{1}{8|J|} \begin{Bmatrix} -r_{24} + r_{34}s + r_{23}t \\ r_{13} - r_{34}s - r_{14}t \\ r_{24} - r_{12}s + r_{14}t \\ -r_{13} + r_{12}s - r_{23}t \end{Bmatrix} , \tag{57}$$

$$\begin{Bmatrix} Y_1 \\ Y_2 \\ Y_3 \\ Y_4 \end{Bmatrix} = \frac{1}{8|J|} \begin{Bmatrix} z_{24} - z_{34}s - z_{23}t \\ -z_{13} + z_{34}s + z_{14}t \\ -z_{24} + z_{12}s - z_{14}t \\ z_{13} - z_{12}s + z_{23}t \end{Bmatrix} , \tag{58}$$

$$\begin{Bmatrix} G_1 \\ G_2 \\ G_3 \\ G_4 \end{Bmatrix} = \frac{1}{r} \begin{Bmatrix} q_1 \\ q_2 \\ q_3 \\ q_4 \end{Bmatrix} , \tag{59}$$

and

$$|J| = \frac{1}{8}[(r_{13} \cdot z_{24} - r_{24} \cdot z_{13}) + (r_{34} \cdot z_{12} - r_{12} \cdot z_{34})s + (r_{23} \cdot z_{14} - r_{14} \cdot z_{23})t]. \tag{60}$$

In the expressions above, q_α and r are defined by Eqs. (36) and (38); $r_{\alpha\beta}$ and $z_{\alpha\beta}$ are defined by

$$r_{\alpha\beta} = r_\alpha - r_\beta ,$$

and

$$z_{\alpha\beta} = z_\alpha - z_\beta ,$$

where (r_α, z_α) is the position of the nodal point in the (r, z) coordinate system.

According to Eqs. (52), (53), and (60), the effective strain rate and volumetric strain rate can be expressed in terms of the surrounding nodal velocities as follows:

$$\dot{\varepsilon} = \sqrt{\frac{2}{3} K_{\alpha\beta} u_\alpha u_\beta} , \tag{61}$$

$$\dot{\varepsilon}_v = Q_\alpha u_\alpha , \tag{62}$$

where Q_α and $K_{\alpha\beta}$ are defined by

$$K_{\alpha\beta} = B_{i\alpha} B_{i\beta} \ , \tag{63}$$

and

$$Q_\alpha = C_i B_{i\alpha} \ . \tag{64}$$

Inserting all the corresponding values in Eq. (32) and performing the necessary differentiations, the first and second derivatives of $\pi_1^{(m)}$, $\pi_2^{(m)}$, and $\pi_3^{(m)}$ are obtained. These are given by

$$\frac{\partial \pi_1^{(m)}}{\partial u_\alpha} = \int_{V^{(m)}} \left(\frac{2}{3}\right) \frac{\bar{\sigma}}{\dot{\bar{\varepsilon}}} K_{\alpha\gamma} u_\gamma \, dV \ ,$$

$$\frac{\partial^2 \pi_1^{(m)}}{\partial u_\alpha \partial u_\beta} = \int_{V^{(m)}} \left(\frac{2}{3}\right) \frac{\bar{\sigma}}{\dot{\bar{\varepsilon}}} \left[K_{\alpha\beta} - \frac{2/3}{\dot{\bar{\varepsilon}}^2} (K_{\alpha\gamma} K_{\beta\delta} u_\gamma u_\delta)\right] dV \ ,$$

$$\frac{\partial \pi_2^{(m)}}{\partial \lambda^{(m)}} = \pi_v^{(m)} = \int_{V^{(m)}} Q_\alpha u_\alpha \, dV \ ,$$

$$\frac{\partial^2 \pi_2^{(m)}}{\partial \lambda^{(m)} \partial u_\alpha} = \frac{\partial \pi_v^{(m)}}{\partial u_\alpha} = \int_{V^{(m)}} Q_\alpha \, dV \ , \tag{65}$$

$$\frac{\partial^2 \pi_v^{(m)}}{\partial u_\alpha \partial u_\beta} = 0 \ ,$$

$$\frac{\partial \pi_3^{(m)}}{\partial u_\alpha} = \int_{V^{(m)}} \zeta Q_\alpha Q_\gamma u_\gamma \, dV \ ,$$

$$\frac{\partial^2 \pi_3^{(m)}}{\partial u_\alpha \partial u_\beta} = \int_{V^{(m)}} \zeta Q_\alpha Q_\beta \, dV \ .$$

Note that if a near-rigid element is found during iterations, the proposed rigid treatment (Section II.2) is used. In this case, the first and second derivatives of the distortional energy, $\pi_1^{(m)}$, become

$$\left.\begin{aligned} \frac{\partial \pi_1^{(m)}}{\partial u_\alpha} &= \int_{V^{(m)}} \left(\frac{2}{3}\right) \frac{\bar{\sigma}}{\dot{\bar{\varepsilon}}} K_{\alpha\gamma} u_\gamma \, dV \\ \frac{\partial^2 \pi_1^{(m)}}{\partial u_\alpha \partial u_\beta} &= \int_{V^{(m)}} \left(\frac{2}{3}\right) \frac{\bar{\sigma}}{\dot{\bar{\varepsilon}}_0} K_{\alpha\beta} \, dV \end{aligned}\right\} \quad (\text{for } \dot{\bar{\varepsilon}} \leq \dot{\bar{\varepsilon}}_0) \; . \tag{66}$$

The results (65) and (66), together with the discretization of $\pi_F^{(m)}$ from the next section, are substituted into Eqs. (34) and (35). With the proper assembling procedures, the system of equations necessary for the Newton-Raphson iterative technique is then obtained. This system of equation is used to obtain a new solution, and the solution procedures are repeated until the desired accuracy is achieved.

Note that all the formulations given above are still valid for plane-strain cases, if the following changes are made: (i) the (r, z) coordinate is replaced by (x, y) coordinates; (ii) the value G_i $(i = 1,\ldots,4)$ in Eq. (59) is set to be zero. It is also worth noting that the corresponding changes in the numerical evaluation of the volume integral (Eq. (65)) must be made for plane-strain cases. Further discussion on numerical integrations can be found in Section III.5.

4. DISCRETIZATION FOR TRACTION PRESCRIBED BOUNDARIES AND CALCULATION OF RESULTANT NODAL FORCES

In general, the discretization formulations for traction prescribed boundaries are very difficult to make if the surface traction is not linearly (or uniformly) distributed over the surface connecting two consecutive nodal points. For this reason, the following discretization formulations are made, under the assumption of linearly distributed surface traction between two consecutive nodal points, for an inclined boundary. These formulations were used for the cases of extrusion and drawing, in which the interfacial frictional stress is assumed as a constant ($f = m \frac{Y_0}{\sqrt{3}}$) and its direction is known.

The inclined boundary is shown in Fig. 2, in which the surface makes an angle α with the horizontal axis. The positions (r_1, z_1) and (r_2, z_2) are assigned to nodals 1 and 2, respectively, for a typical element along this boundary. Normal and shear stresses, (p_1, τ_1) and (p_2, τ_2) are given at these points. With the assumption of linearly distributed traction, the prescribed stresses in the r and z directions, at an arbitrary point (r, z) along this surface, are given by

$$\begin{aligned} F_r &= \left[\frac{\tau_1(r_2 - r)}{r_2 - r_1} - \frac{\tau_2(r_1 - r)}{r_2 - r_1}\right] \sin\alpha + \left[\frac{p_1(r_2 - r)}{r_2 - r_1} - \frac{p_2(r_1 - r)}{r_2 - r_1}\right] \cos\alpha; \\ F_z &= \left[\frac{\tau_1(r_2 - r)}{r_2 - r_1} - \frac{\tau_2(r_1 - r)}{r_2 - r_1}\right] \cos\alpha - \left[\frac{p_1(r_2 - r)}{r_2 - r_1} - \frac{p_2(r_1 - r)}{r_2 - r_1}\right] \sin\alpha. \end{aligned} \tag{67a}$$

For the quadrilateral element used in the present investigations, the velocities have bilinear distributions inside the element and are linear along the boundaries. For any arbitrary point along the surface, the velocities (u_r, u_z) are expressible in terms of the nodal velocities (u_{r_1}, u_{z_1}) and (u_{r_2}, u_{z_2}),

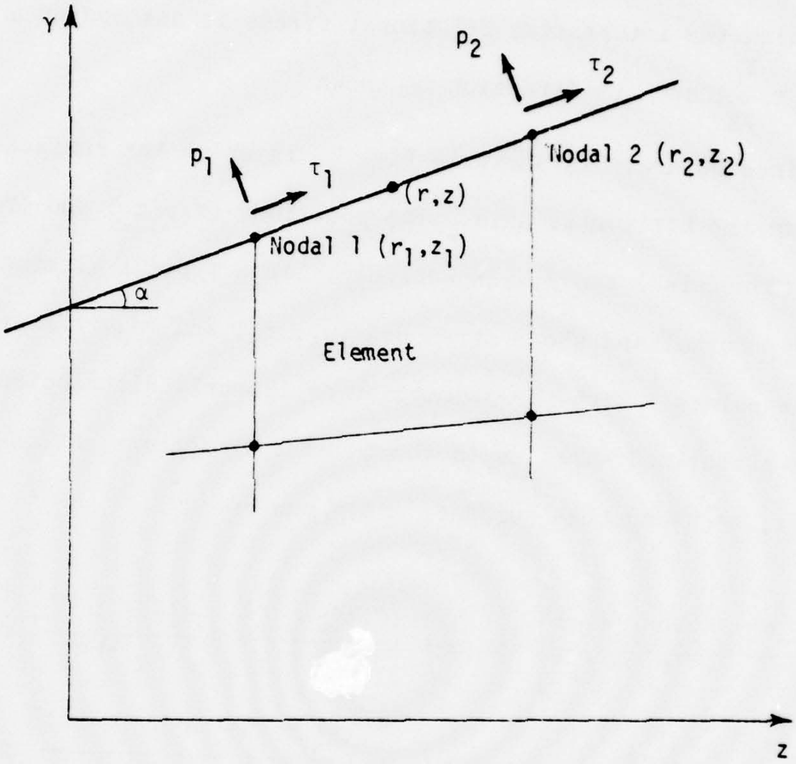

Fig. 2 Traction prescribed inclined boundary.

$$u_r = \frac{u_{r_1}(r_2 - r)}{r_2 - r_1} - \frac{u_{r_2}(r_1 - r)}{r_2 - r_1} ;$$

$$u_z = \frac{u_{z_1}(r_2 - r)}{r_2 - r_1} - \frac{u_{z_2}(r_1 - r)}{r_2 - r_1} . \tag{67b}$$

Inserting Eqs. (67a) and (67b) into Eq. (32d) and performing the necessary integration, the following results are then obtained for the integral $\pi_F^{(m)}$, for plane cases and axisymmetric cases, respectively:

$$\pi_F^{(m)} = \frac{W}{6} \left\{ \begin{aligned} &[(2p_1 + p_2)\Delta z + (2\tau_1 + \tau_2)\Delta r]u_{r_1} \\ &+ [-(2p_1 + p_2)\Delta r + (2\tau_1 + \tau_2)]u_{z_1} \\ &+ [(p_1 + 2p_2)\Delta z + (\tau_1 + 2\tau_2)\Delta r]u_{r_2} \\ &+ [-(p_1 + 2p_2)\Delta r + (\tau_1 + 2\tau_2)\Delta z]u_{z_2} \end{aligned} \right\} ; \quad \text{(plane cases)} \tag{68}$$

$$\pi_F^{(m)} = \frac{\pi}{6} \begin{bmatrix} \{[p_1(3r_1+r_2) + p_2(r_1+r_2)]\Delta z + [\tau_1(3r_1+r_2) + \tau_2(r_1+r_2)]\Delta r\}u_{r_1} \\ + \{-[p_1(3r_1+r_2) + p_2(r_1+r_2)]\Delta r + [\tau_1(3r_1+r_2) + \tau_2(r_1+r_2)]\Delta z\}u_{z_1} \\ + \{[p_1(r_1+r_2) + p_2(r_1+3r_2)]\Delta z + [\tau_1(r_1+r_2) + \tau_2(r_1+3r_2)]\Delta r\}u_{r_2} \\ + \{-[p_1(r_1+r_2) + p_2(r_1+3r_2)]\Delta r + [\tau_1(r_1+r_2) + \tau_2(r_1+3r_2)]\Delta z\}u_{z_2} \end{bmatrix} ,$$

$$\text{(axisymmetric cases)} \tag{69}$$

where W is the width of the workpiece in plane cases, and Δr, Δz are defined by $\Delta r = r_2 - r_1$ and $\Delta z = z_2 - z_1$, respectively.

In view of Eqs. (68) and (69), the first derivatives of $\pi_F^{(m)}$, which are equivalent to the corresponding nodal forces, are all constants; and the second derivatives are all zeros. These results are substituted into Eqs. (34) and (35) for the formulation of Newton-Raphson iterations.

There is another type of boundary condition in which the frictional stress depends not only on the direction, but also on the magnitude of the velocity of the deforming body relative to the die, such as the neutral flow problems described in Section V. The discretization procedures are very complicated and the formulations require very tedious manipulations. Detailed discretization formulations for this kind of boundary conditions are given in Section V.

For nodal points along the velocity prescribed boundary, the nodal velocity u_α is equal to the prescribed value and the obtained value of Δu_α must always be equal to zero. This can be accomplished by modifying the equation corresponding to Δu_α in Eq. (34) or (35), such that this equation becomes $\Delta u_\alpha = 0$ during every iteration. The obtained velocity field and the value of the Lagrange multiplier are then used to calculate the resultant nodal force corresponding to this velocity prescribed nodal point, according to $f_\alpha = \sum_{m=1}^{M} \frac{\partial}{\partial u_\alpha} [\pi_1^{(m)} + \lambda^{(m)}\pi_v^{(m)}]$ for the Lagrange multiplier constraint, and $f_\alpha = \sum_{m=1}^{M} \frac{\partial}{\partial u_\alpha} [\pi_1^{(m)} + \pi_3^{(m)}]$ or $\sum_{m=1}^{M} \frac{\partial}{\partial u_\alpha} [\pi_1^{(m)} + \frac{\zeta}{2v^{(m)}} (\pi_v^{(m)})^2])$ for the penalty function constraint.

5. DISCUSSION OF THE NUMERICAL INTEGRATION

Throughout the present investigation, the Gaussian quadrature formulas are used for volume integration. For a given function, H(r, z) (or H(x, y) in plane cases) the integration is given by

$$\int_V H\,dV = \begin{cases} 2\pi \int_r \int_z rH(r,z)\,dr\,dz & \text{(axisymmetric)} \\ W \int_x \int_y H(x,y)\,dx\,dy & \text{(plane cases)} \end{cases}$$

$$= \begin{cases} 2\pi \int_{-1}^{1} \int_{-1}^{1} H(s,t)r(s,t)|J(s,t)|\,ds\,dt \\ W \int_{-1}^{1} \int_{-1}^{1} H(s,t)|J(s,t)|\,ds\,dt \end{cases} , \tag{70}$$

where W is the width of the workpiece in plane cases and $|J|$ is the determinant of the Jacobian of the coordinate transformation.

The 2×2 Gaussian quadrature gives the following evaluation of these volume integrations:

$$\int_V H\,dV = \begin{cases} 2\pi \sum_{i=1}^{4} \rho_i [H\cdot r\cdot J]\Big|_{s=s_i;\ t=t_i} \\ W \sum_{i=1}^{4} \rho_i [H\cdot J]\Big|_{s=s_i;\ t=t_i} \end{cases} , \tag{71}$$

where ρ_i is the weighting factor, which is equal to 1 for all four integration points. The locations of these integration points are tabulated and given in Table 2.

For an integral with its integrand expressible by a polynomial of s and t, the exact evaluation of this integral can be made by the 2×2 Gaussian quadrature for orders up to s^3 and t^3. In the present studies, this 2×2 numerical integration is applied to all volume integrals except $\pi_3^{(m)}$ $(\pi_3^{(m)} = \int_{V^{(m)}} \frac{\zeta}{2} \dot{\varepsilon}_v^2\,dV)$. Note that a reduced 1×1 integration must be used for $\pi_3^{(m)}$ in order to avoid the possibility of over-constraint due to the 2×2 numerical integrations. The reasons are clearly shown below.

Table 2

Locations of integration points for 2×2 Gaussian quadrature formulas

i	s_i	t_i
1	$\frac{1}{\sqrt{3}}$	$\frac{1}{\sqrt{3}}$
2	$-\frac{1}{\sqrt{3}}$	$\frac{1}{\sqrt{3}}$
3	$\frac{1}{\sqrt{3}}$	$-\frac{1}{\sqrt{3}}$
4	$-\frac{1}{\sqrt{3}}$	$-\frac{1}{\sqrt{3}}$

Consider a typical element $V^{(m)}$; the volumetric strain rate $\dot{\varepsilon}_v$ inside this element is given by

$$\dot{\varepsilon}_v = \frac{1}{|J|} \sum_{\alpha=1}^{8} (a_\alpha + b_\alpha s + c_\alpha t) u_\alpha . \tag{72}$$

where a_α, b_α, c_α are all independent of (s, t); and the detailed expressions of these constants can be found from Eqs. (62) and (56), which are omitted here. For the cases of plane-strain and plane-stress, the exact evaluation of the integral corresponding to dilatation energy in the Lagrange multiplier formulation is given by

$$\pi_2^{(m)} = \lambda^{(m)} \int_V \dot{\varepsilon}_v \, dV = 4\lambda^{(m)} \left(\sum_{\alpha=1}^{8} a_\alpha u_\alpha \right), \tag{73}$$

which can also be obtained from either a 2×2 numerical integration or a reduced 1×1 integration. Note that in the 1×1 integration, the integration point is located at the centroid of the element (i.e., s = 0, t = 0) and the weighting factor is 4. Now consider the penalty function constraint $\pi_3^{(m)}$; the integral can be written in terms of the local coordinates s and t:

$$\pi_3^{(m)} = \int_{-1}^{1}\int_{-1}^{1} \frac{\zeta}{2}\,\frac{1}{|J|}\Big[\sum_{\alpha=1}^{8} (a_\alpha + b_\alpha s + c_\alpha t)u_\alpha\Big]\Big[\sum_{\beta=1}^{8} (a_\beta + b_\beta s + c_\beta t)u_\beta\Big]\, ds\, dt. \tag{74}$$

With reduced 1×1 numerical integration, the result of the integral above is given by

$$\pi_3^{(m)} = 4\cdot\left(\frac{\zeta}{2}\right)\cdot\left(\frac{4}{A}\right)\cdot\sum_{\alpha=1}^{8} a_\alpha u_\alpha \sum_{\beta=1}^{8} a_\beta u_\beta\ , \tag{75}$$

where A is the area of the element. Clearly, the derivatives of the equation above (75) is equivalent to those derivatives of Eq. (73) if the mean stress $\lambda^{(m)}$ is made according to (17) (i.e., $\lambda^{(m)} = \zeta\dot{\varepsilon}_v$) with the value of $\dot{\varepsilon}_v$ evaluated at the centroid of the element.

Hence, when the minimum solution is made, the 1×1 integration of the penalty constraint $\pi_3^{(m)}$ gives the desired incompressibility condition, which is equivalent to that of the Lagrange multiplier constraint. This is, however, no longer true if the 2×2 numerical integration is used in the evaluation of the integral $\int_V \frac{\zeta}{2}\dot{\varepsilon}_v^2\, dV$, because the constants b_α and c_α in Eq. (73) and the reduced one-point integration of (74) require the zero volumetric strain rate $\dot{\varepsilon}_v$ be satisfied only at the centroid of the element; but the 2×2 integration requires the zero values of $\dot{\varepsilon}_v$ be satisfied at all four integration points. This over-constraint requirement induced by the 2×2 integration will give an incorrect solution; the 1×1 reduced integration is, therefore, highly recommended for the evaluation of the penalty term, $\pi_3^{(m)}$.

It is to be noted that if the modified penalty function $\frac{\zeta}{2v^{(m)}}(\pi_v^{(m)})^2$ (Eq. (33c) is used, the reduced integration is no longer necessary because the quantity $\dot{\varepsilon}_v^2$ is not presented in the formulation. Thus, the modified penalty function can be applied, without any restriction, to any problems, including axisymmetric and three-dimensional cases.

Section IV

MULTIPASS EXTRUSION AND DRAWING

1. INTRODUCTION

Many bar drawing and extrusion processes in practice are multipass operations. Internal fracturing (center bursting) in these processes usually occurs after some area reduction through several passes. In order to predict and prevent the occurrence of such defects, it is necessary to determine the deformation characteristics involved in multipass operations. The influence of the deformation history on the current flow pattern, among others, is a unique feature of the problem.

Since the detailed mechanics, particularly the stress and strain paths at a critical site of a deforming material, are the required information, the method of analysis should be capable of accurately determining not only overall quantities involved in metalworking processes, such as forming loads, but also stress and strain distributions during deformation. Furthermore, work-hardening and distributed flow stress due to previous passes must be taken into consideration in the analysis. The finite-element approach comes close to fulfilling these requirements.

In the present investigation the rigid-plastic finite-element method was used as an analysis technique. The effect of work-hardening was examined in single-pass operations and the effect of distributed flow stress on the flow pattern was revealed by analyzing two-pass drawing and extrusion.

2. METHOD OF ANALYSIS

The steady-state, multipass, axisymmetric extrusion, and drawing processes were analyzed by the rigid-plastic finite-element method with the modified penalty function constraint, Eq. (18). Numerical integrations of the modified penalty term, $\frac{\beta}{2V^{(m)}} [\int_{V^{(m)}} \dot{\varepsilon}_V \, dV]^2$, were made by one-point integration evaluated at the element center. Fig. 5 compares the results of 2×2 integration and 1×1 integration for the penalty term for the case of extrusion without friction. As Fig. 5 shows, the reduced one-point integration resulted in a smoother distribution of the stress along the axis of symmetry, with its magnitude approximately equivalent to the mean value of the stress obtained by 2×2 integration.

Integration of strain rates were made according to the scheme discussed in the previous AFML report [40]. For work-hardening materials at the first pass, the effective strain was assumed zero at the starting point of the flow line. For the second pass (or any pass other than the first pass), the resulting effective strain of the previous pass was used as the initial value of the effective strain at the starting point of the flow line. Effective strains were calculated at every iteration, and the iteration was performed repeatedly until the desired accuracy was achieved. Note that the stress distributions obtained from computations differ from the actual distribution by a uniform hydrostatic component. Accordingly, the necessary corrections were made, using the technique described in [40].

3. COMPUTATIONAL CONDITIONS

Figure 3 shows the mesh systems and the boundary conditions used for the analysis. Both systems consist of 135 elements interconnected at 160 nodals. The process conditions for extrusion and drawing under which the computation was carried out are summarized in Tables 3 and 4, respectively.

Table 3

Extrusion process conditions for computation

Die semi-cone angle: $\alpha = 45°$

Reduction ratio: $R_i/R_0 = 1.6$

	Die workpiece interface frictional stress f	
Material	1st pass	2nd pass
Non-work-hardening	0	-
$\bar{\sigma} = Y_0$	$0.4Y_0$	
Pure aluminum		
$\bar{\sigma} = Y_0(1 + \frac{\bar{\varepsilon}}{0.319})^{0.34}$	0	0
$Y_0 = 106.86 MN/m^2$	$0.4Y_0$	$0.4Y_0$

Table 4

Drawing process conditions for computation

Die semi-cone angle: $\alpha = 6°$

Reduction ratio: $R_i/R_0 = 1.1$

	Die workpiece interface frictional stress f	
Material	1st pass	2nd pass
Non-work-hardening		
$\bar{\sigma} = Y_0$	$0.4Y_0$	-
Aluminum alloy 2024-T351		
$\bar{\sigma} = Y_0(1 + \frac{\bar{\varepsilon}}{0.0102})^{0.171}$		
$Y_0 = 309.4 MN/m^2$	$0.4Y_0$	$0.4Y_0$

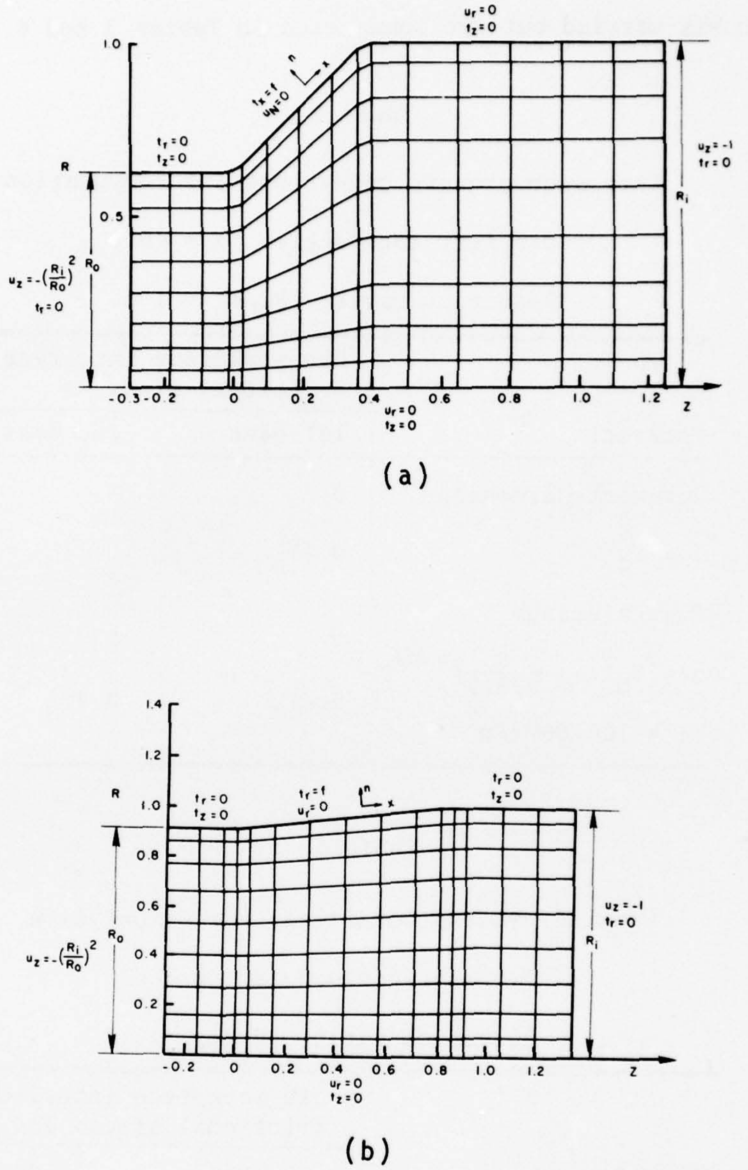

Fig. 3 Mesh system and the boundary conditions used in computation for (a) extrusion and (b) drawing.

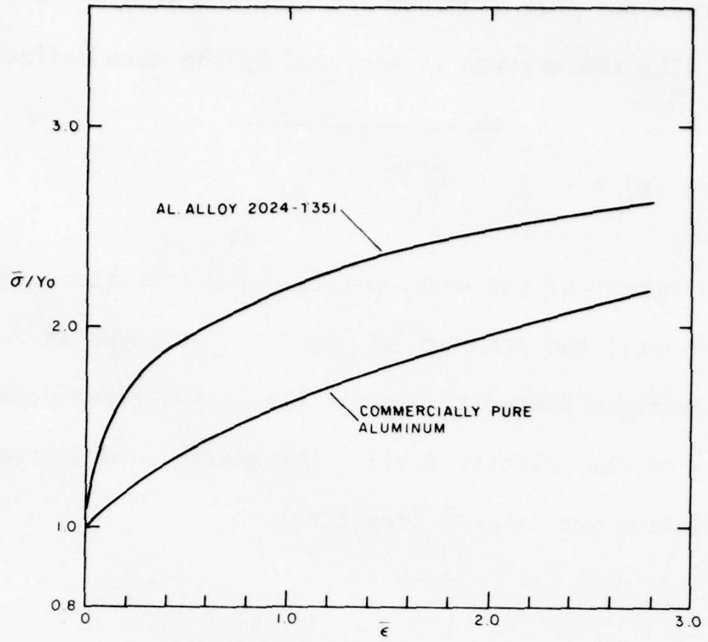

Fig. 4 Stress-strain curves of the two materials used in computation.

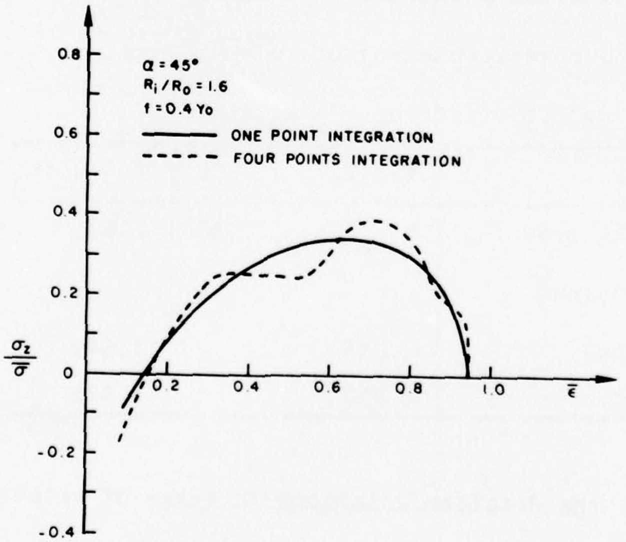

Fig. 5 Comparison of one-point and 2×2 Gaussian integration of the penalty term (axial stress vs. total strain along the axis of extrusion; material: non-work-hardening).

Stress-strain curves for pure aluminum and aluminum alloy 2024-T351 are shown in Fig. 4. The convergence is measured by the norm defined by

$$\frac{\|\Delta \underset{\sim}{u}\|}{\|\underset{\sim}{u}\|}, \quad \text{where } \|\underset{\sim}{u}\| = \sqrt{\sum_{i=1}^{N} \{(u_{r_i})^2 + (u_{z_i})^2\}}$$

N being the total number of the nodal points. The iteration continues for each solution until the accuracy of $\Delta \underset{\sim}{u} / \underset{\sim}{u} \leq 0.00005$ is reached. The number of iterations needed to achieve this convergence depends on the initial guess of the velocity field. The average number required for the final solution was 20 ∿ 30 iterations.

4. EXTRUSION

The average extrusion pressures computed for all of the cases given in Table 3 are summarized in Table 5.

Table 5

Average extrusion pressures

Die semi-cone angle: $\alpha = 45°$

Reduction ratio: $R_i/R_0 = 1.6$

Material	f = 0	$f = 0.4Y_0$
Non-work-hardening	$p_{ave}/Y_0 = 1.451$	1.823
Pure aluminum		
1st pass	2.218	2.642
2nd pass	2.982	3.425

We shall now discuss the detailed solutions in terms of velocity distributions, grid distortions, and stress and strain distributions.

The general trend of the velocity distributions is the same in all cases and is in agreement with the measurements in the visioplasticity study of axisymmetric extrusion of lead [41]. In Fig. 6 the effects of work-hardening are shown by comparing the velocity distributions for a non-work-hardening material and for commercially pure aluminum under the interface friction of $f = 0.4Y_0$. The two velocity components are plotted as functions of the radial coordinate at various locations in the axial direction. The distribution patterns are the same for both cases but the magnitudes differ. The velocity distributions during the first pass and the second pass in frictionless extrusion are compared in Fig. 7. A close examination of Figs. 6 and 7 shows that the distributions during the second pass are closer to those for a non-work-hardening material.

Detailed differences of deformation characteristics, due to material properties and multipass operations, are more clearly revealed, for example, in grid distortions. The steady-state grid distortion patterns are compared for non-work-hardening and work-hardening cases in Fig. 8 and for the two passes in Fig. 9. It is seen in Fig. 10 that distortion of grid lines that are originally perpendicular to the axis of the workpiece is less for non-work-hardening materials than that for work-hardening materials. A comparison of grid distortions for two passes, given in Fig. 9, shows that distortion of grid lines for the second pass is less than for the first pass, confirming the observation in velocity distributions that the deformation pattern during the second pass is closer to that for non-work-hardening materials. An important feature of grid distortions can be seen from the vertical grid distortion at the exit, as plotted in Fig. 10. For friction extrusion, grid distortion is greatest for the first pass of work-hardening

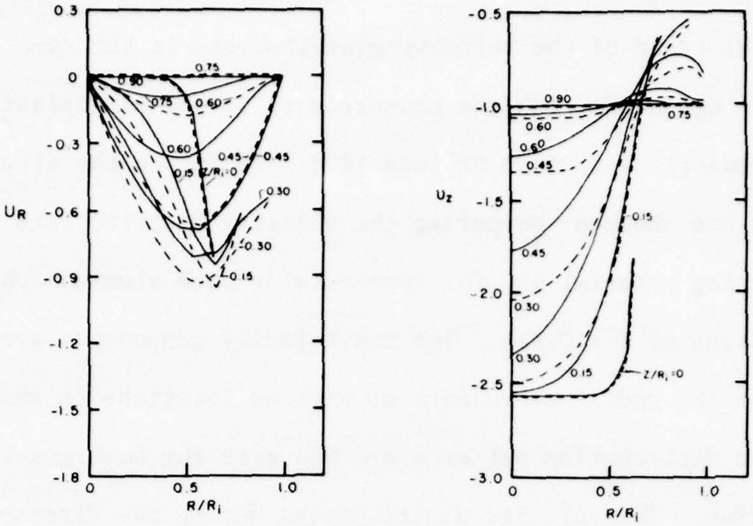

Fig. 6 Distributions of velocity components.
α = 45°, R_i/R_0 = 1.6, f = 0.4Y_0;
materials: non-work-hardening (– – –)
and pure aluminum, 1st pass (——).

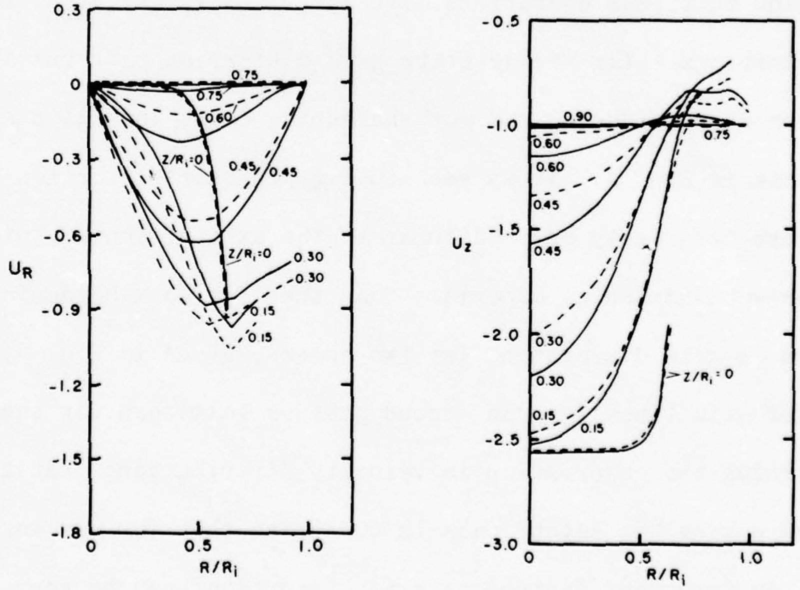

Fig. 7 Distribution of velocity components.
α = 45°, R_i/R_0 = 1.6, f = 0;
material: pure aluminum, 1st pass (——),
2nd pass (– – –).

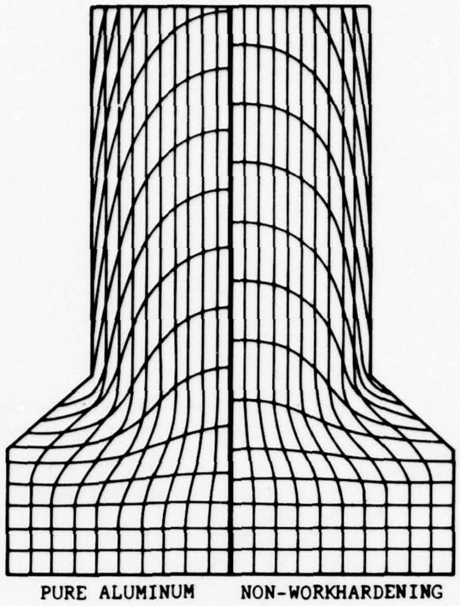

Fig. 8 Grid distortion for non-work-hardening materials and pure aluminum ($f = 0.4Y_0$).

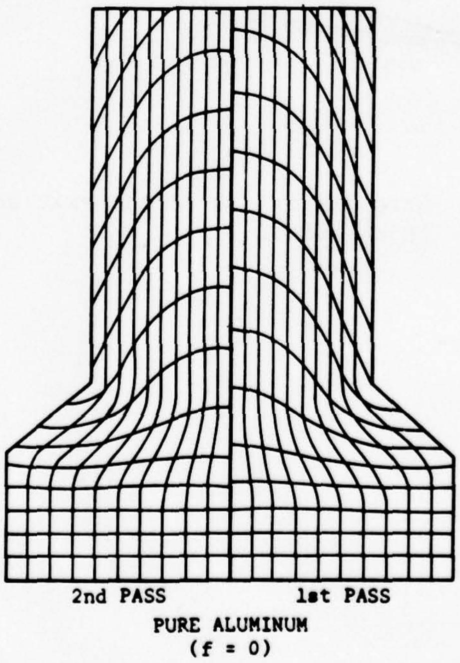

Fig. 9 Comparison of grid distortion in pure aluminum for 1st and 2nd passes ($f = 0$).

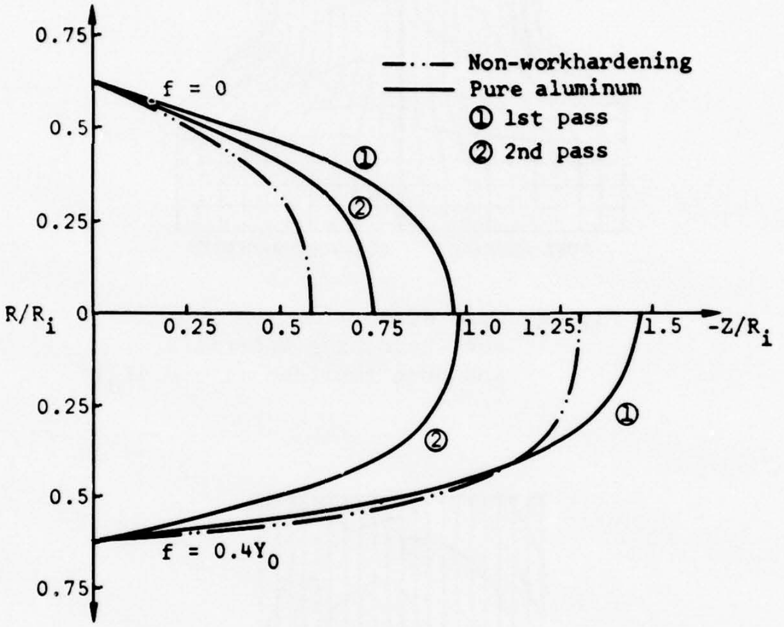

Fig. 10 Grid distortion at the exit section in extrusion.

materials, less for the second pass of work-hardening materials, and least for non-work-hardening materials. This order is different, however, when interface friction is present, because the magnitude of the frictional stress relative to the flow stress of incoming material is less for the second pass of work-hardening materials, in comparison to other cases. This is, in effect, a reduction of friction, thereby reducing the total grid distortion.

The effective strain rates were integrated along the flow lines to yield the effective strain distributions and are shown in Fig. 11. The figure also shows the boundaries between the rigid and plastically deforming regions by a near-zero strain-rate contour. The rigid-plastic boundaries at the exit are almost identical in shape and location for all cases. However, the size of the deformation zone is larger for work-hardening materials at the first pass but reduces at the second pass and becomes almost the same as that for non-work-hardening materials. It is of interest to note that the distribution of additional strains during the second pass is very close to that for non-work-hardening materials. So far, all indications with regard to the effect of distributed flow stress on the incoming material are that the deformation characteristics during the second pass are different from those during the first pass due to the non-uniform flow stress distributions in the incoming material and are closer to those for non-work-hardening materials. The reason for this is not obvious. Examining the strain distributions and corresponding flow stress distributions at the exit section shown in Fig. 12, we can see that non-uniformity of flow stress distribution after the first pass is appreciable due to the effect of work-hardening, but that the increase in flow stress during

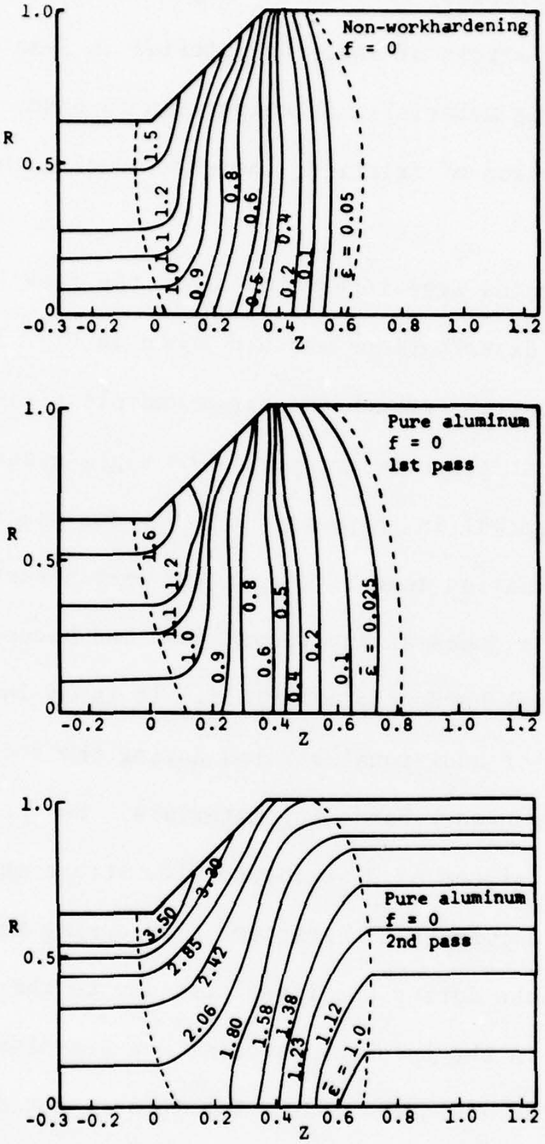

Fig. 11 The effective strain distributions in extrusion.

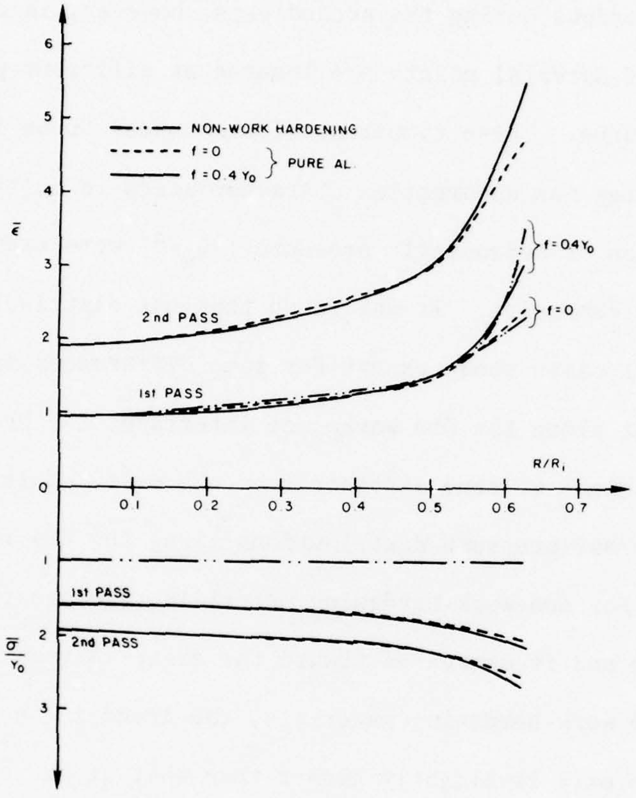

Fig. 12 The effective stress and the effective strain distributions across a section of an extruded bar.

the second pass is almost constant across the section. During the second pass, the two effects are combined. These are the effects of further work-hardening and the effect of initial nonuniform flow stress distributions. Due to work-hardening during the first pass, the manner in which the material work-hardens during the second pass, however, is different because the state-of-material points are located at different points on the stress-strain curve. These combined effects appear to be influential factors in determining the deformation characteristics in multipass extrusion.

The distribution of hydrostatic pressure $(-\sigma_m/\bar{\sigma})$ were examined in Fig. 13 for frictionless extrusion. It was found that the distribution patterns are the same for all cases shown except for some differences in magnitude. It was observed that along the die workpiece interface, the hydrostatic pressure shows a minimum at some distance from the exit. This feature is seen also in the normal pressure distributions along the die interface shown in Fig. 14. For non-work-hardening materials, the pressure is highest at the entrance and it decreases toward the exit, increasing again near the exit. For work-hardening materials, the trend is the same but the pressure at the exit is slightly higher than that at the entrance. For the second pass, the magnitude increases again with the pressure greatest at both the exit and the entrance.

The critical site for the occurrence of center bursting in extrusion is along the axis of extrusion. The stress and strain histories are important for applying a ductile fracture criterion. Fig. 15 shows these stress and strain histories along the axis of extrusion for the frictionless case. The axial stress becomes tensile over a certain range of deformation and a larger tension zone is obtained for non-work-hardening materials than that for work-hardening materials. The tensile stress

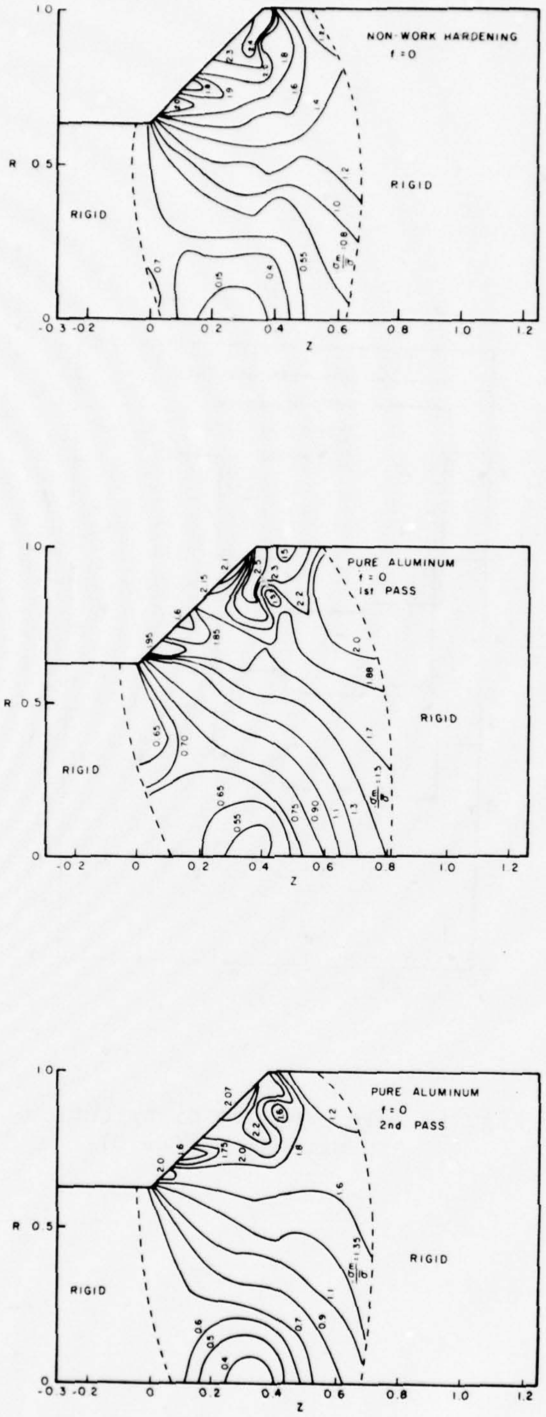

Fig. 13 Hydrostatic pressure distributions in extrusion.

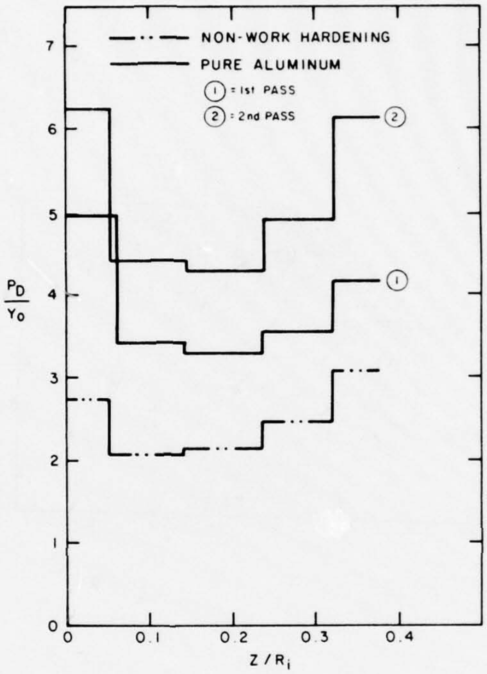

Fig. 14 Die pressure distribution in extrusion (f = 0).

increases during the second pass. It was found that the interface friction has the effect of decreasing the axial stress, thus suppressing the possibility of producing center burst. These results are qualitatively in agreement with experimental observations. Fig. 16 shows the variations of axial stress along the center axis for the case of constant interface friction with $f = 0.4Y_0$. As mentioned earlier, the magnitude of the frictional stress ($f = 0.4Y_0$) relative to the flow stress ($\bar{\sigma}$) is less for the second pass than that for the first pass. Therefore, due to the effects of this reducing frictional stress, the amount of tensile stress increased during the second pass is greater for the friction case (Fig. 16) than that for the frictionless case (Fig. 15).

5. DRAWING

The drawing process is characterized by smaller die angles and smaller area reduction, when compared with those for extrusion. The computed average drawing stresses are listed in Table 6.

Table 6

Average drawing stresses

Die semi-cone angle: $\alpha = 6°$

Reduction ratio: $R_i/R_0 = 1.1$

Material	$f = 0.4Y_0$
Non-work-hardening	$\sigma_{ave}/Y_0 = 0.906$
Aluminum alloy 2024-T351	
1st pass	1.042
2nd pass	1.118

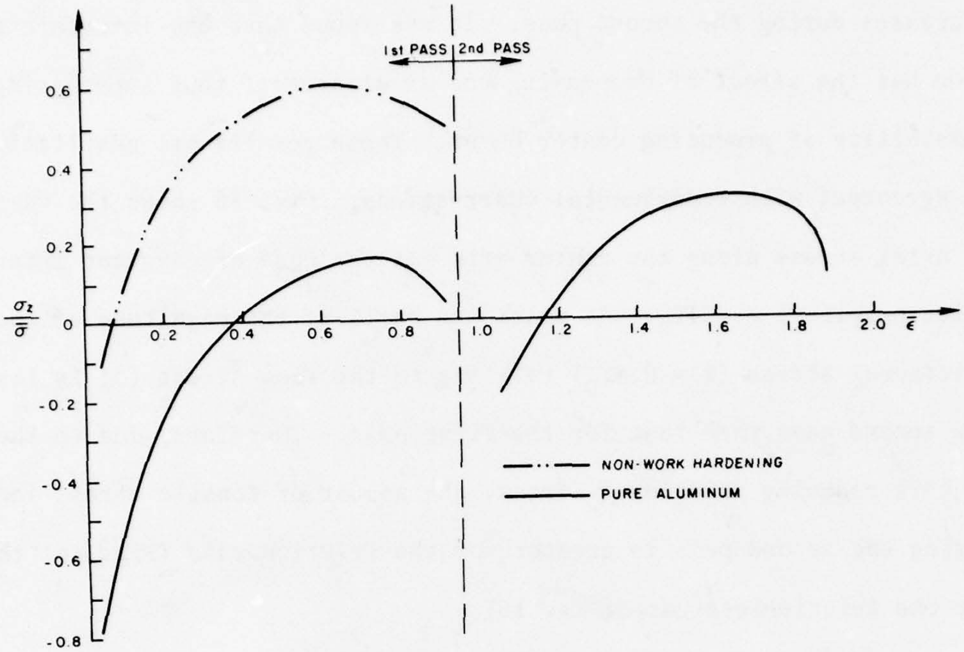

Fig. 15 Stress and strain history of a material point along the axis of extrusion (f = 0).

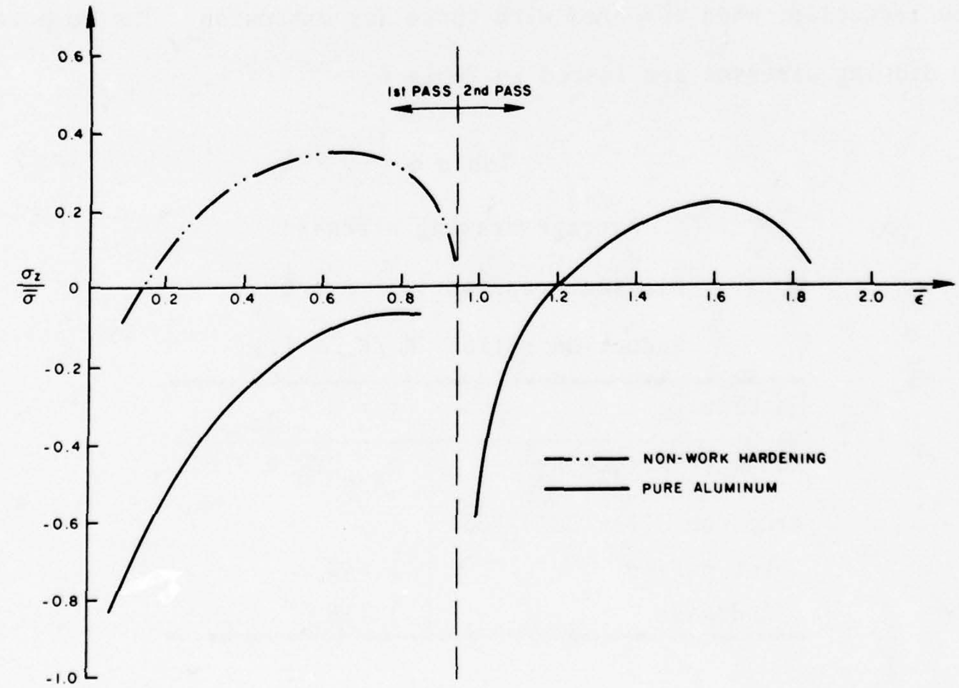

Fig. 16 Stress and strain history of a material point along the axis of extrusion (f = $0.4Y_0$).

Grid distortions at the exit are given in Fig. 17. In comparison with Fig. 10 for extrusion, Fig. 17 shows that the grid lines for drawing form the double-peak distortion in the drawn part for non-work-hardening materials. For work-hardening materials, this tendency lessens for the first pass, but increases again for the second pass, suggesting that the deformation characteristics during the second pass become similar to that of non-work-hardening materials.

The strain distributions (Fig. 18) for the three cases are similar to those for extrusion, as shown in Fig. 11. The variation of effective strain distributions in drawn bars (Fig. 19) is also similar to that in Fig. 12 for extrusion except that the variation is comparatively small due to a small die angle and small reductions. In drawing it is observed also that the increase in flow stress during the second pass is almost uniform across the bar section. The hydrostatic component distributions are given in Fig. 20. Also, the rigid-deforming boundaries are shown in the figure. The deformation zone size increases in the first pass of work-hardening materials, compared to that of non-work-hardening materials, but decreases in the second pass and becomes almost identical to that for non-work-hardening materials. It is also concluded that the strain distributions during the second pass are closer to those for a non-work-hardening material, although the difference between those for the first pass of work-hardening materials and of non-work-hardening materials are not too great. The hydrostatic component distributions revealed that the region under the die is in the compressive hydrostatic stress state, while the core and exit regions are in the tensile hydrostatic stress state. The stress distributions are similar with some differences in magnitude. The die pressure distributions are greatest at the entrance and minimum at the

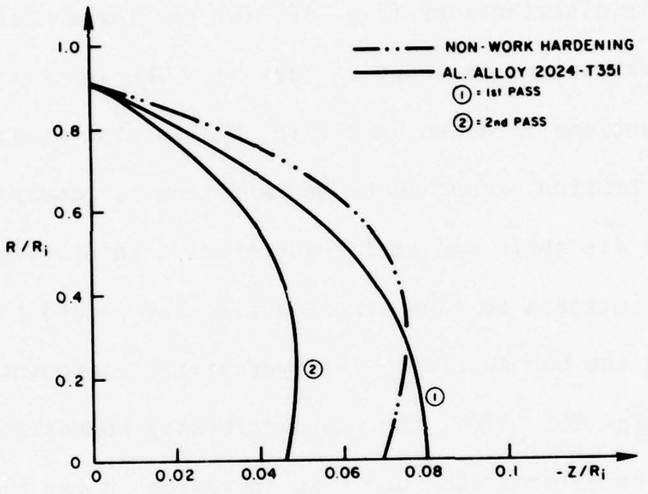

Fig. 17 Grid distortion at exit section in drawing ($f = 0.4Y_0$).

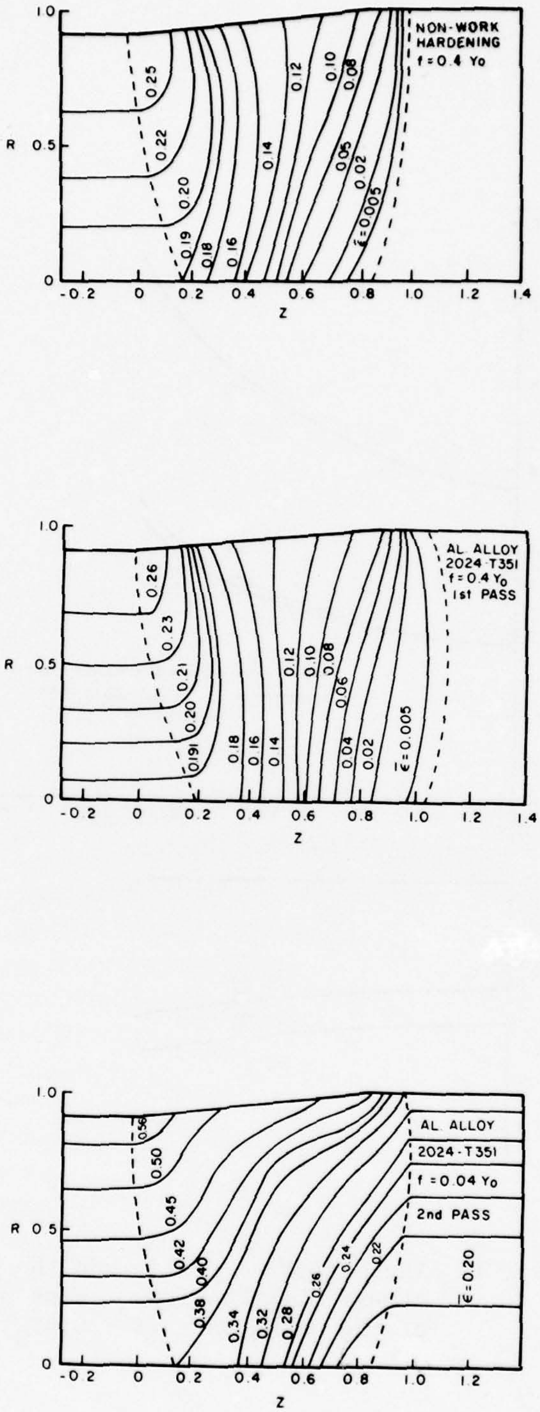

Fig. 18 The effective strain distributions in drawing.

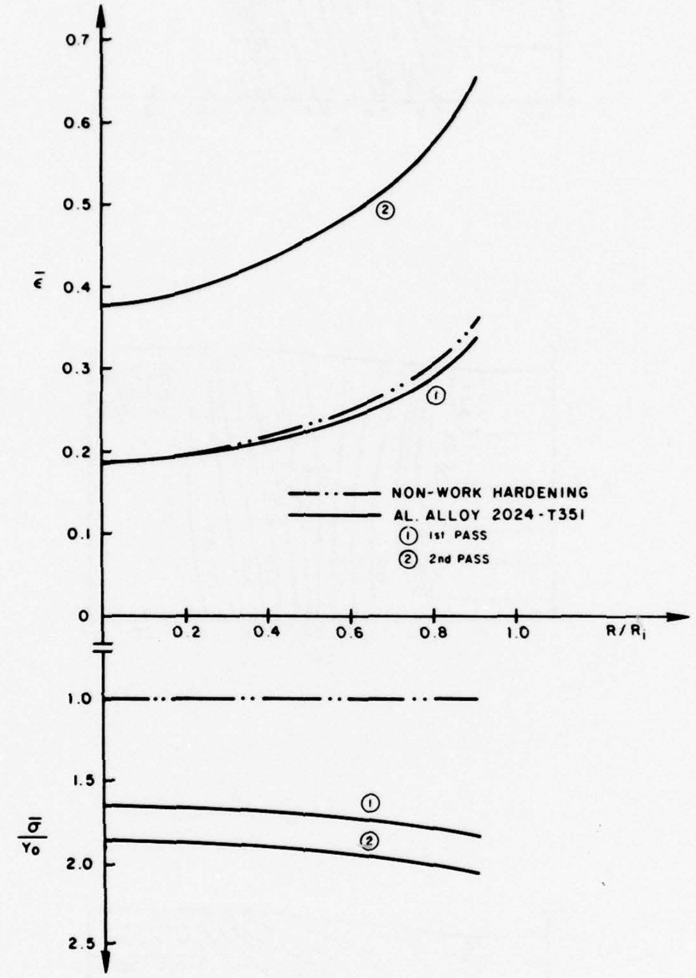

Fig. 19 The effective strain and the effective stress distributions across a section of the drawn bars (f = $0.4Y_0$).

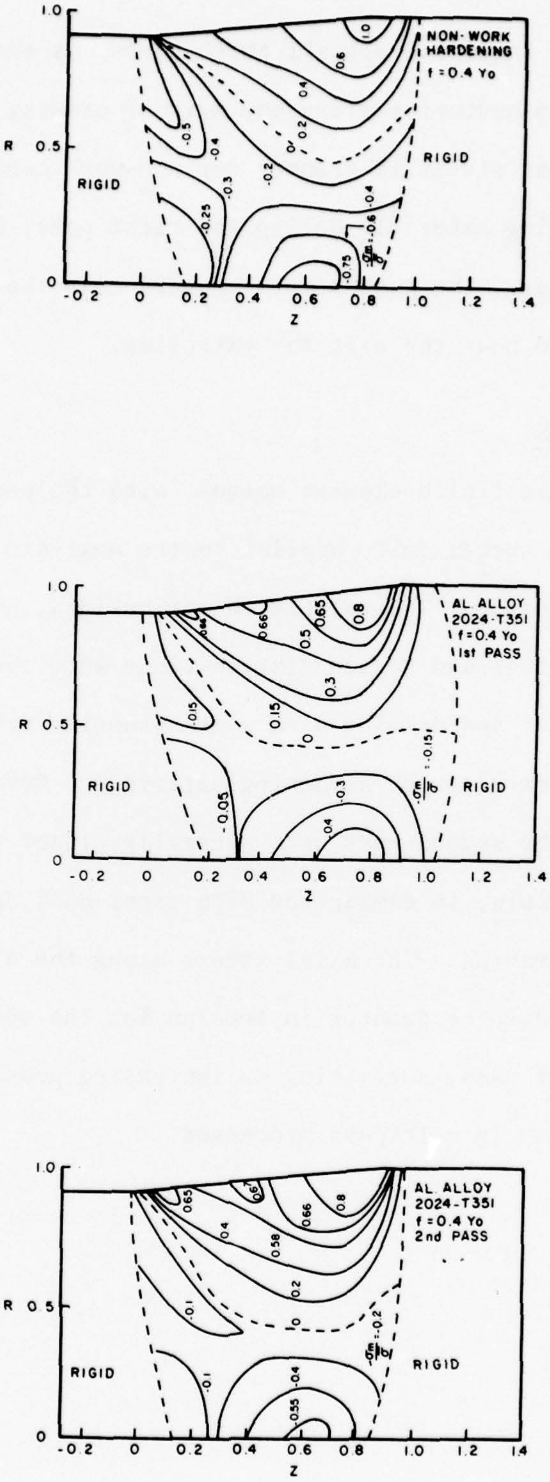

Fig. 20 Hydrostatic pressure distribution in drawing.

halfway point of the interface for all three cases, as shown in Fig. 21. The stress and strain histories along the axis of drawing are plotted in Fig. 22. The axial stress is greater for non-work-hardening materials than for work-hardening materials during the first pass, but increases during the second pass. The peak stress appears near the entrance, while this peak is observed near the exit for extrusion.

6. CONCLUDING REMARKS

The rigid-plastic finite-element method, with the penalty function constraint, has been successfully applied to the analysis of multipass bar drawing and extrusion. The velocity distributions, grid distortions, die pressure, and stress and strain distributions were obtained in detail for two-pass extrusion and drawing of a work-hardening material. Solutions were also obtained for non-work-hardening materials. Deformation characteristics during the second pass were generally closer to those of non-work-hardening materials, in comparison with first-pass deformation, for both extrusion and drawing. The axial stress along the axis of extrusion and drawing was found to be greater in tension for the second pass than that during the first pass, suggesting an increasing possibility of center burst formation in multipass processes.

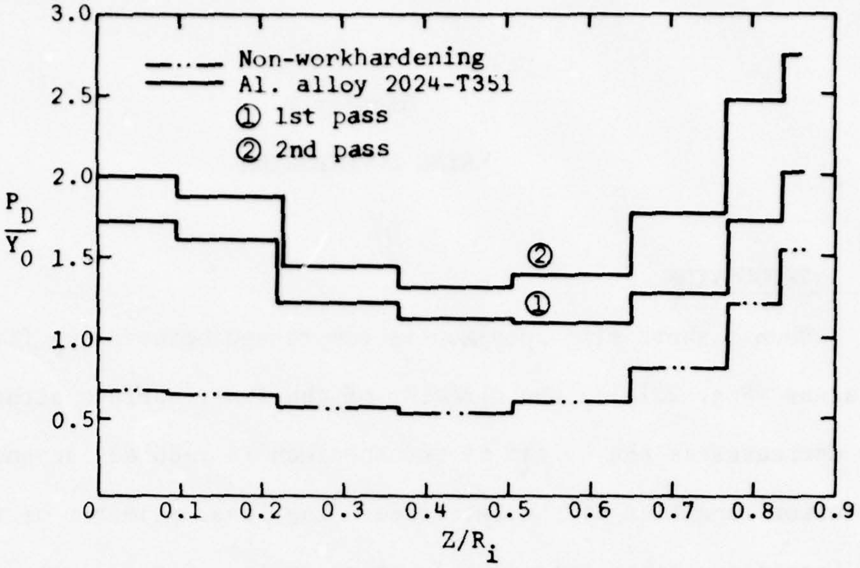

Fig. 21 Die pressure distribution in drawing ($f = 0.4Y_0$).

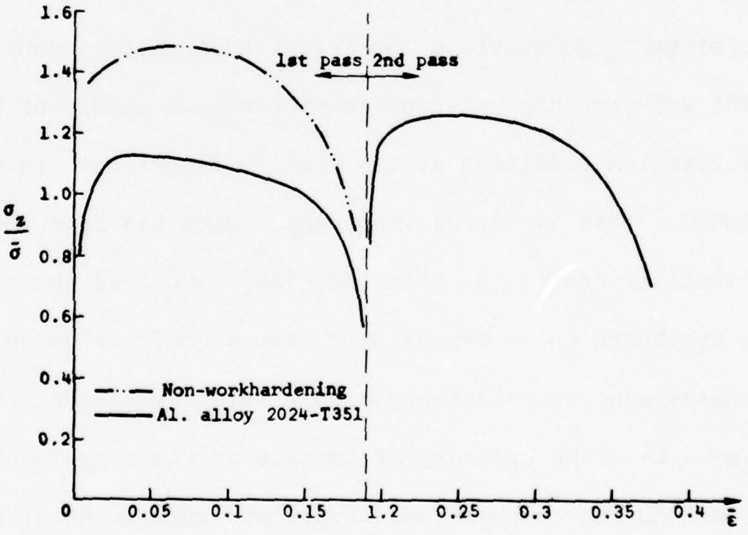

Fig. 22 Stress and strain history of a material point along the axis of drawing.

Section V

RING COMPRESSION

1. INTRODUCTION

When a short ring specimen is compressed between two flat, parallel platens (Fig. 23(a)), the diameter of the inner surface either increases or decreases as the height of the specimen is reduced, depending on the friction condition at the interface. The inner diameter of the ring is increased if the interface friction is low (Fig. 23(b)) and it is decreased if this friction is high (Fig. 23(c)). Because the change in internal diameter of the compressed ring is sensitive to friction at the die-workpiece interface, ring compression has been widely used as a test to evaluate the friction condition in metal-working processes.

In order to demonstrate the friction condition quantitatively, however, the relationship between the geometrical change of the workpiece and the friction condition at the work tool-workpiece interface must be established. This aspect of ring compression has been the subject of many investigations in the past [42]-[55]. Most of the mathematical methods are based on an approximate stress analysis or on the upper-bound analysis using relatively simple velocity fields. Earlier analysis assumed that the cylindrical surface of the ring specimen remains cylindrical during compression. Explicit expressions of neutral point radius and corresponding geometrical changes were obtained by the stress analysis for rigid-perfectly plastic materials with constant coefficient friction [42] or with constant interface frictional stress

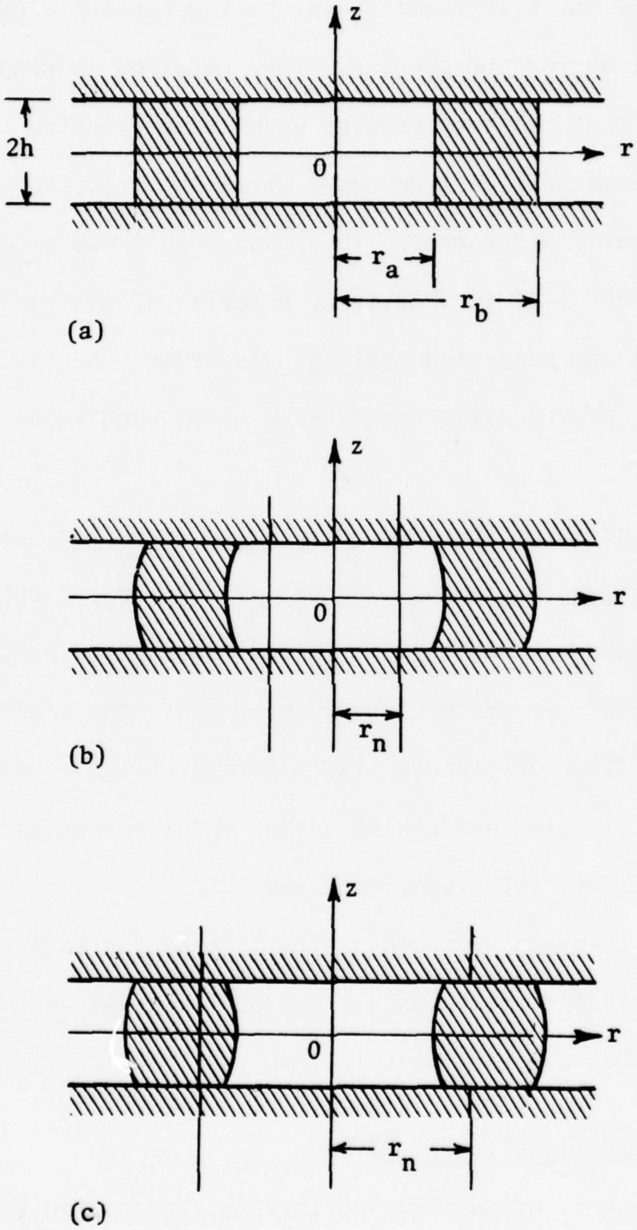

Fig. 23 Two deformation modes in ring compression.

[45]. Under the same assumptions, the upper-bound solutions were given for constant frictional stress [43], [44]. DePierre and Male [47] attempted to include the effect of work-hardening by assuming that the ratio of the frictional stress to the current flow stress remains constant during the process. They observed in comparing theory with experiment that the test results under high friction conditions exceeded the theoretical maximum curve where the frictional stress is equal to the shear yield stress. This discrepancy was also found in a subsequent report [48] in predicting material flow stress using ring compression. It was suggested that the discrepancy may be due to severe barreling of the ring-free surface under conditions of high friction.

The upper-bound solutions, including bulge formation, were introduced by Avitzur [49], assuming exponential cusp-shaped bulge, and by Liu [51], for cosine-shaped bulge. In addition to the bulge formation, material dependency of deformation was taken into the analysis by Lee and Altan [52]. They utilized a finite mesh system for computing the flow stress distribution and minimized the total energy rate according to the provided admissible velocity field.

While these theories provided useful information in practice, more accurate and realistic solutions are needed for wider and more meaningful applications of the ring test in industry.

2. RIGID-PLASTIC FINITE-ELEMENT METHOD

A unique feature of deformation in ring compression (also in rolling and forging) is that there exists a point (or a region) along the die-workpiece interface where the velocity of the deforming material relative to the die velocity becomes zero (neutral flow point). The frictional stress usually changes its direction at the neutral flow point, but the location of this point is not known a priori. In implementing the finite-element method for the analysis of this type of problem, difficulties always exist in the formulation of boundary conditions along the die-workpiece interface. Recently, Matsumoto, Oh, and Kobayashi [56] reformulated the boundary conditions according to the direction of relative velocities at the interface, and solved the problem of ring compression with low friction. However, a difficulty was encountered for the case of high friction, because of the development of the neutral flow region (rather than the neutral flow point). In the present investigation, a variational formulation was developed for the case where the frictional stress is dependent on the relative velocity at the die-workpiece interface. This formulation, when interface friction is low, is almost identical to that developed by Matsumoto et al., and permits the treatment of neutral flow region along the interface. The finite-element solution of ring compression was then obtained under various friction conditions for several materials. Some of the results were compared with the previously published theoretical solutions and experimental results.

A. Problem formulation

Consider a body of volume, V, with the traction, $\underset{\sim}{F}$, prescribed on a part, S_F, of the surface and the velocity, $\underset{\sim}{V}$, prescribed on surface, S_u. Let S_c be the remainder of the surface where the frictional stress, $\underset{\sim}{f}$, acts and the die velocity, $\underset{\sim}{u}^D$, is given. The actual stress and velocity fields satisfy the following relations:

(a) Equilibrium conditions:

$$\sigma_{ij,j} = 0 \quad \text{(neglecting the body force)}; \tag{76}$$

(b) Compatibility conditions:

$$\dot{\varepsilon}_{ij} = \frac{1}{2}(v_{i,j} + v_{j,i}) \quad \text{and} \quad \dot{\varepsilon}_v = v_{i,i} = 0; \tag{77}$$

(c) Stress-strain rate relationship:

$$\sigma'_{ij} = \frac{2}{3}\frac{\bar{\sigma}}{\dot{\bar{\varepsilon}}}\dot{\varepsilon}_{ij} ; \tag{78}$$

where σ'_{ij} is the deviatoric stress, $\bar{\sigma}$ and $\dot{\bar{\varepsilon}}$ are the effective stress and the effective strain rates, respectively, and defined by $\bar{\sigma} = \sqrt{\frac{3}{2}\sigma'_{ij}\sigma'_{ij}}$ and $\dot{\bar{\varepsilon}} = \sqrt{\frac{2}{3}\dot{\varepsilon}_{ij}\dot{\varepsilon}_{ij}}$.

(d) Boundary conditions:

$$\begin{aligned} &\sigma_{ij}n_i = F_j \quad \text{on } S_F , \\ &v_i = V_i \quad \text{on } S_u , \\ &\sigma_{ij}n_i = f_j(\underset{\sim}{V}_R) \quad \text{on } S_c , \\ &\underset{\sim}{V}_R = \underset{\sim}{v} - \underset{\sim}{u}^D = V_R\underset{\sim}{t} . \end{aligned} \tag{79}$$

where $\underset{\sim}{n}$ is the unit outward normal to the surface, $\underset{\sim}{V}_R$ is the relative velocity between the die and the deforming body and $\underset{\sim}{t}$ is the unit base vector along the die-workpiece interface.

Let v* be any admissible velocity field satisfying the incompressibility condition $\dot{\varepsilon}^*_v = 0$ and the velocity boundary conditions, the virtual work principle gives:

$$\int_V \sigma_{ij}\dot{\varepsilon}^*_{ij}\,dV = \int_{S_F} \underset{\sim}{F}\cdot\underset{\sim}{v}^*\,dS + \int_{S_C} \underset{\sim}{f}\cdot(\underset{\sim}{V}^*_R + \underset{\sim}{u}^D)\,dS + \int_{S_u} (\sigma_{ij}n_j)V_i\,dS, \tag{80}$$

where $\underset{\sim}{V}^*_R = \underset{\sim}{v}^* - \underset{\sim}{u}^D$ is the relative velocity between the deforming material and the die, associated with the admissible velocity $\underset{\sim}{v}^*$.

For the case where the magnitude of the frictional stress, $\underset{\sim}{f}$, is specified according to the assumption that the ratio of the frictional stress to the shear yield stress, k, remains constant, $\underset{\sim}{f}$ is expressed by

$$\underset{\sim}{f}(\underset{\sim}{V}_R) = -mk\,\frac{V_R}{|\underset{\sim}{V}_R|}\,\underset{\sim}{t}\,, \tag{81}$$

where m is the friction factor $(0 \leq m \leq 1)$. Eq. (80), together with the inequality

$$\underset{\sim}{f}(\underset{\sim}{V}_R)\cdot\underset{\sim}{V}^*_R - \underset{\sim}{f}(\underset{\sim}{V}^*_R)\cdot\underset{\sim}{V}^*_R > 0, \tag{82}$$

according to Eq. (81), and the convexity and normality conditions of the yield surface,

$$(\sigma^*_{ij} - \sigma_{ij})\dot{\varepsilon}^*_{ij} \geq 0, \tag{83}$$

gives

$$\int_V \sigma^*_{ij}\dot{\varepsilon}^*_{ij}\,dv - \int_{S_F} \underset{\sim}{F}\cdot\underset{\sim}{v}^*\,dS - \int_{S_c} \underset{\sim}{f}(\underset{\sim}{V}^*_R)\cdot\underset{\sim}{V}^*_R\,dS \geq \int_{S_u} (\sigma_{ij}n_j)V_i\,dS, \tag{84}$$
$$+ \int_{S_c} \underset{\sim}{f}(\underset{\sim}{V}_R)\cdot\underset{\sim}{u}^D\,dS$$

where σ^*_{ij} is the stress associated with $\dot{\varepsilon}^*_{ij}$ and on the yield surface. Removing the constraint of incompressibility condition of an admissible velocity field $\underset{\sim}{v}^*$ (denoted by $\underset{\sim}{u}$) by introducing the Lagrange multiplier λ, the stationary value problem for the finite-element formulation is now stated as

$$\frac{\partial\Phi}{\partial \underset{\sim}{u}} = \frac{\partial}{\partial \underset{\sim}{u}} \{\int_V \bar{\sigma}\dot{\bar{\varepsilon}}\, dV - \int_{S_F} \underset{\sim}{F}\cdot\underset{\sim}{u}\, dS - \int_{S_c} \underset{\sim}{f}(\underset{\sim}{V}_R)\cdot\underset{\sim}{V}_R\, dV + \int_V \lambda\dot{\varepsilon}_v\, dV\} = 0. \qquad (85)$$

Eq. (85) is the one used in [56]. Note that in Eq. (85) the relative velocity, $\underset{\sim}{V}_R$, and the volumetric strain rate, $\dot{\varepsilon}_v$, is now defined by $\underset{\sim}{V}_R = \underset{\sim}{u} - \underset{\sim}{u}^D$ and $\dot{\varepsilon}_v = u_{i,i}$, respectively.

In order to have the stationary value, the existence and continuity of the derivatives of Φ with respect to $\underset{\sim}{u}$ is required. Therefore, no converged solution can be expected when two consecutive nodal point velocities relative to the die become zero or close to zero, by the direct application of Eq. (85). In order to overcome this difficulty, the use of velocity-dependent frictional stress is proposed as the interface condition. It is expressed by

$$\underset{\sim}{f} = -mk\left\{\left(\frac{2}{\pi}\right) \tan^{-1} \left(\frac{V_R}{a|u^D|}\right)\right\} \underset{\sim}{t}, \qquad (86)$$

where the die velocity, $\underset{\sim}{u}^D$, is equal to unity and a is a constant which is several orders less than the die velocity (say, 10^{-5}) so that the frictional stress given by Eq. (86) is almost identical to that of Eq. (81), for $|\underset{\sim}{V}_R|$ slightly larger than zero (say, $|\underset{\sim}{V}_R| > 10^{-4}$).

With the interface friction given by Eq. (86), the stationary condition is expressed by, instead of Eq. (85),

$$\frac{\partial \Phi}{\partial \mathbf{u}} = \frac{\partial}{\partial \mathbf{u}} \left\{ \int_V \bar{\sigma} \dot{\bar{\varepsilon}} \, dV + \int_V \lambda \dot{\varepsilon}_v \, dV - \int_{S_F} \mathbf{F} \cdot \mathbf{u} \, dS - \int_{S_C} \left(\int_0^{|\mathbf{V}_R|} \mathbf{f} \cdot d\mathbf{V}_R \right) dS \right\} = 0. \tag{87}$$

For the proof, note that the following inequality is used instead of Eq. (82):

$$\left\{ \int_0^{|\mathbf{V}_R^*|} \mathbf{f} \cdot d\mathbf{V}_R - \int_0^{|\mathbf{V}_R|} \mathbf{f} \cdot d\mathbf{V}_R \right\} \leq \mathbf{f}(\mathbf{V}_R) \cdot (\mathbf{V}^* - \mathbf{V}_R) . \tag{88}$$

Discretization formulations of the last term in Eq. (87) are given in the following subsection.

B. Discretization of the friction term

Denote the last term inside the brackets in Eq. (87) by

$$\Phi_f = -\int_{S_c} \left[\int_0^{|\mathbf{V}_R|} \mathbf{f} \cdot d\mathbf{V}_R \right] dS . \tag{89}$$

Let r_1 and r_2 be the radial positions of the two consecutive nodal points 1 and 2, whose velocity components are (u_{r_1}, u_{z_1}) and (u_{r_2}, u_{z_2}), respectively. The unit base vector, $\mathbf{t}$, is assigned along the die-workpiece interface as shown in Fig. 24. The relative velocities, $\mathbf{V}_{R_1}$ and $\mathbf{V}_{R_2}$ are equal to the nodal point velocities in the r-direction, respectively, namely,

$$\begin{aligned} \mathbf{V}_{R_1} &= V_{R_1} \mathbf{t} = u_{r_1} \mathbf{r}; \\ \mathbf{V}_{R_2} &= V_{R_2} \mathbf{t} = u_{r_2} \mathbf{r}. \end{aligned} \tag{90}$$

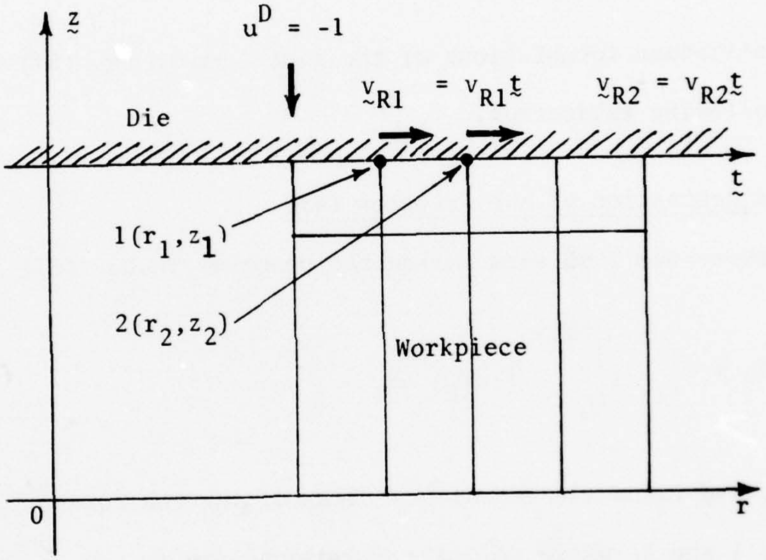

Fig. 24 Two consecutive nodal points and relative velocities at die-workpiece interface.

With a bilinear velocity distribution for a quadrilateral element, the relative velocity along the interface is a linear function of r and is expressed by

$$V_R = u_r = \frac{r - r_2}{r_1 - r_2} u_{r_1} + \frac{r_1 - r}{r_1 - r_2} u_{r_2} \; . \tag{91}$$

For the frictional stress represented by

$$\underset{\sim}{f} = -\left\{ mk \left(\frac{2}{\pi} \right) \tan^{-1} \frac{V_R}{a} \right\} \underset{\sim}{t} \; , \tag{92}$$

Φ_f, given by Eq. (89) can be written as

$$\Phi_f = \begin{cases} \displaystyle\int_{S_c} \left[\int_0^{-V_R} mk \left(\frac{2}{\pi} \right) \tan^{-1} \left(\frac{V_R}{a} \right) dV_R \right] dS & \text{for } V_R \leq 0 ; \\ \\ \displaystyle\int_{S_c} \left[\int_0^{V_R} mk \left(\frac{2}{\pi} \right) \tan^{-1} \left(\frac{V_R}{a} \right) dV_R \right] dS & \text{for } V_R \geq 0 . \end{cases} \tag{93}$$

Substituting Eq. (91) into Eq. (93) and performing integration and differentiation, the expressions necessary for the Newton-Raphson procedure are obtained as follows:

$$\frac{\partial\Phi_f}{\partial u_{r_1}} = A\cdot\left[\begin{aligned} &\left\{\tan^{-1}\frac{u_{r_2}}{a}\right\}\left\{2r_1(-3u_{r_2}a^2+u_{r_2}^3) + r_2[-3u_{r_1}u_{r_2}^2+u_{r_2}^3+3(u_{r_1}+u_{r_2})a^2]\right\} \\ &-\left\{\tan^{-1}\frac{u_{r_1}}{a}\right\}\left\{2r_1(3u_{r_1}u_{r_2}^2-3u_{r_1}^2u_{r_2}+u_{r_1}^3-3u_{r_2}a^2)\right. \\ &\qquad\qquad\qquad\qquad\left. + r_2[-3u_{r_1}^2u_{r_2}+u_{r_1}^3+3(u_{r_1}+u_{r_2})a^2]\right\} \\ &+ a\left\{r_1(5u_{r_2}^2 - 6u_{r_1}u_{r_2}+u_{r_1}^2) + 2r_2(u_{r_1}^2-u_{r_2}^2)\right\} \\ &+ \left\{\ln\frac{u_{r_2}^2+a^2}{u_{r_1}^2+a^2}\right\}\left\{r_1(a^3-3au_{r_2}^2) + r_2(-a^3+3au_{r_1}u_{r_2})\right\} \end{aligned}\right],$$

$$\frac{\partial\Phi_f}{\partial u_{r_2}} = A\left[\begin{aligned} &\left\{\tan^{-1}\frac{u_{r_2}}{a}\right\}\left\{r_1[-3u_{r_1}u_{r_2}^2+u_{r_2}^3+3(u_{r_1}+u_{r_2})a^2]\right. \\ &\qquad\qquad\qquad\left. + 2r_2(3u_{r_1}^2u_{r_2}-3u_{r_1}u_{r_2}^2+u_{r_2}^3-3u_{r_1}a^2)\right\} \\ &-\left\{\tan^{-1}\frac{u_{r_1}}{a}\right\}\left\{r_1[-3u_{r_1}^2u_{r_2}+u_{r_1}^3+3(u_{r_1}+u_{r_2})a^2] + 2r_2(u_{r_1}^3-3u_{r_1}a^2)\right\} \\ &+ a\left\{2r_1(u_{r_1}^2-u_{r_2}^2) + r_2(-5u_{r_1}^2+6u_{r_1}u_{r_2}-u_{r_2}^2)\right\} \\ &+ \left\{\ln\frac{u_{r_2}^2+a^2}{u_{r_1}^2+a^2}\right\}\left\{r_1(-a^3+3au_{r_1}u_{r_2}) + r_2(a^3-3au_{r_1}^2)\right\} \end{aligned}\right],$$

$$\frac{\partial^2\Phi_f}{\partial u_{r_1}^2} = B\cdot\left[\begin{aligned} &\left\{\tan^{-1}\frac{u_{r_2}}{a} - \tan^{-1}\frac{u_{r_1}}{a}\right\}\left\{6r_1(-3u_{r_2}a^2+u_{r_2}^3) + 6r_2(-u_{r_1}u_{r_2}^2+2u_{r_2}a^2+u_{r_1}a^2)\right\} \\ &+ a\left\{3r_2(u_{r_1}^2-3u_{r_2}^2+2u_{r_1}u_{r_2}) + 3r_1(5u_{r_2}^2-6u_{r_1}u_{r_2}+u_{r_1}^2)\right\} \\ &+ \left\{\ln\frac{u_{r_2}^2+a^2}{u_{r_1}^2+a^2}\right\}\left\{3r_1(a^3-3au_{r_2}^2) + 3r_2(au_{r_2}^2+2au_{r_1}u_{r_2}-a^3)\right\} \end{aligned}\right].$$

$$\frac{\partial^2 \Phi_f}{\partial u_{r_2}^2} = B \cdot \left[\left(\tan^{-1} \frac{u_{r_2}}{a} - \tan^{-1} \frac{u_{r_1}}{a} \right) \left\{ 6r_1 (u_{r_1}^2 u_{r_2} - u_{r_2} a^2 - 2u_{r_1} a^2) + 6r_2(-u_{r_1}^3 + 3u_{r_1} a^2) \right\} \right.$$

$$+ a \left\{ 3r_1(-3u_{r_1}^2 + 2u_{r_1} u_{r_2} + u_{r_2}^2) + 3r_2(u_{r_2}^2 + 5u_{r_1}^2 - 6u_{r_1} u_{r_2}) \right\}$$

$$\left. + \left\{ \ln \frac{u_{r_2}^2 + a^2}{u_{r_1}^2 + a^2} \right\} \left\{ 3r_1 (a^3 - 2au_{r_1} u_{r_2} - au_{r_1}^2) + 3r_2(-a^3 + 3au_{r_1}^2) \right\} \right],$$

$$\frac{\partial^2 \Phi_f}{\partial u_{r_1} \partial u_{r_2}} = B \cdot \left[\left(\tan^{-1} \frac{u_{r_2}}{a} - \tan^{-1} \frac{u_{r_1}}{a} \right) \left\{ 6r_1(-u_{r_1} u_{r_2}^2 + 2u_{r_2} a^2 + u_{r_1} a^2) \right. \right.$$

$$\left. + 6r_2(u_{r_1}^2 u_{r_2} - u_{r_2} a^2 - 2u_{r_1} a^2) \right\}$$

$$+ a \left\{ 3r_1(u_{r_1}^2 - 3u_{r_2}^2 + 2u_{r_1} u_{r_2}) + 3r_2(-3u_{r_1}^2 + 2u_{r_1} u_{r_2} + u_{r_2}^2) \right\},$$

$$+ \left\{ \ln \frac{u_{r_2}^2 + a^2}{u_{r_1}^2 + a^2} \right\} \left\{ 3r_1 (au_{r_2}^2 + 2au_{r_1} u_{r_2} - a^3) \right.$$

$$\left. \left. + 3r_2(-au_{r_1}^2 - 2au_{r_1} u_{r_2} + a^3) \right\} \right]$$

where

$$A = 2\pi \text{ mk} \left(\frac{2}{\pi} \right) \left[\frac{r_2 - r_1}{6(u_{r_2} - u_{r_1})^3} \right]$$

and

$$B = \frac{A}{(u_{r_2} - u_{r_1})} .$$

3. COMPUTATIONAL CONDITIONS

The ratio of the outer diameter, the inner diameter, and the thickness of a ring specimen was 6:3:2. The computation of ring compression was performed for several materials under various values of m in Eq. (86) for interface friction ($a = 10^{-5}$). The materials were selected from several references and are tabulated, with their stress-strain relationships, in Table 7(a).

Table 7(a)

Materials and their stress-strain curves used for computation

No.	Material	Stress-strain relation	Initial yield stress	Reference
1	Commercially pure aluminum	$\bar{\sigma}/Y_0=(1. + \frac{\bar{\varepsilon}}{0.3193})^{0.34}$	Y_0 = 15,500 psi (106.86 MN/m^2)	[48]
2	O.F.H.C. copper	$\bar{\sigma}/Y_0=(1. + \frac{\bar{\varepsilon}}{0.3518})^{0.28}$	Y_0 = 42,000 psi (289.56 MN/m^2)	[48]
3	Al.1100F	$\bar{\sigma}/Y_0=(1. + 0.768\bar{\varepsilon})$	Y_0 = 16,500 psi (113.76 MN/m^2)	[56]
4	Annealed 1100 Al.	$\bar{\sigma}/Y_0=(1. + \frac{\bar{\varepsilon}}{0.05205})^{0.3}$	Y_0 = 9,100 psi (62.74 MN/m^2)	[52]

The stress-strain curves corresponding to the materials given in Table 7(a) are shown in Fig. 25.

The friction conditions and the mesh system used for computation are given in Table 7(b).

Table 7(b)

Interface friction condition and mesh system

No.	Material	Die-workpiece interfacial friction condition	Mesh system
1	Commercially pure aluminum	$m = 0.2; 0.12$ with $k = Y_0/\sqrt{3}$ $m = 0.12$ with $k = \bar{\sigma}/\sqrt{3}$	Fig. 7.3(b)
2	O.F.H.C. copper	$m = 0.6, 1.0$ with $k = Y_0/\sqrt{3}$ $m = 1.0$ with $k = \bar{\sigma}/\sqrt{3}$	Fig. 7.3(b)
3	Al.1100F	$m = 0.5$ with $k = Y_0/\sqrt{3}$	Fig. 7.3(a)
4	Annealed 1100 aluminum	$m = 0.25; 1.0$ with $k = \bar{\sigma}/\sqrt{3}$	Fig. 7.3(b)

The two mesh systems used in calculation are shown in Figs. 26(a) and (b). Both systems consist of 96 elements and 117 nodal points each. Fig. 26(a) is the same mesh as that in [56], while in Fig. 26(b) smaller elements were used near the die-workpiece interface and both corners because of the large gradient of strain rate there and possible folding formations at corners.

The non-steady-state deformation problems in ring compression was analyzed in a step-by-step manner by treating it quasi-linearly during each incremental deformation. The reduction in height at each step is 1%. The solution of velocity fields at the first step of [56] ($m = 0.3$) was used as an initial guess for all the friction conditions. The measure of the convergence is represented by the quantity $\|\Delta \underset{\sim}{u}\|/\|\underset{\sim}{u}\|$ where $\Delta \underset{\sim}{u}$ is the error vector found during iterations and the Euclidean vector norm is defined by $\|u\| = \sqrt{\sum_{i=1}^{n} (u_{r_i}^2 + u_{z_i}^2)}$, where N = total number

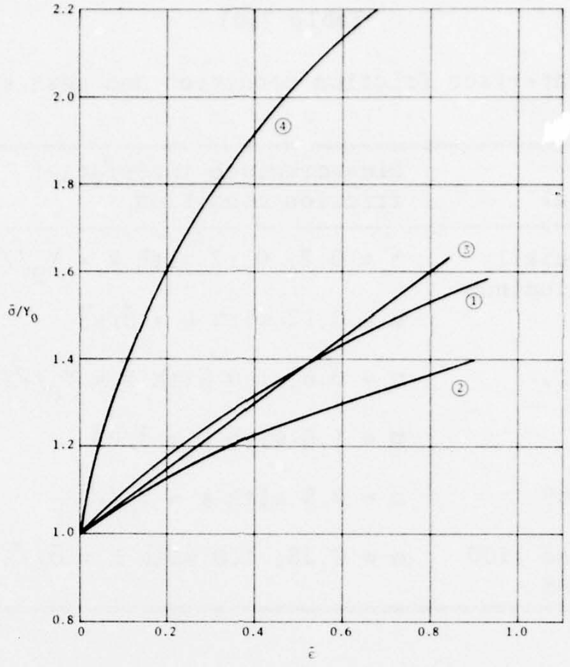

Fig. 25 Stress-strain relationships for (1) commercially pure aluminum, (2) O.F.H.C. copper, (3) Al. 1100-F, and (4) Annealed al. 1100.

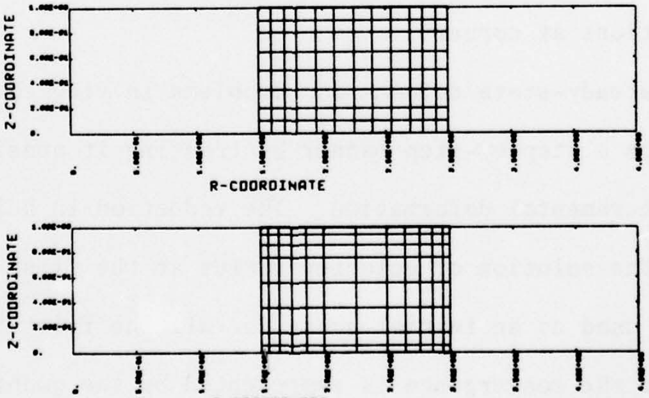

Fig. 26 Mesh systems used for computation.

of nodal points. The solution obtained from the previous step was then used as an initial guess for the subsequent step. Normally, 8 to 30 iterations were required for the first step to reach the accuracy of $\Delta \underset{\sim}{u} / \underset{\sim}{u} \leq 0.00005$, depending on the difference of friction factor, m, between the present case and initial guess. For subsequent steps, only 3 to 5 iterations were necessary to reach the same accuracy. Some additional iterations were required during steps where inside or outside folding was formed.

4. RESULTS AND DISCUSSION

The computed results are shown in Fig. 27 in terms of changes of minimum internal diameter as functions of reduction in height. The figure revealed that the geometrical changes differ depending upon the selection of the shear yield stress, initial or current, for the same m value. The difference becomes significant for large reductions in height for both m = 0.12 and m = 1.0. It is also seen that the geometrical changes are affected by the material property as indicated by the curves of m = 1.0 for copper and for annealed aluminum.

A comparison of the present numerical solutions with those by the upper-bound method [49], [50] was shown in Fig. 28. For low friction, the two solutions coincide with each other for small reduction range, but deviate considerably for large reductions. It is interesting to note a coincidence of the two solutions for m = 0.12. The numerical solution for this case was obtained using the current shear yield stress. For high friction discrepancies of the two are more significant.

Experimental data taken from the literature [47], [50] were also

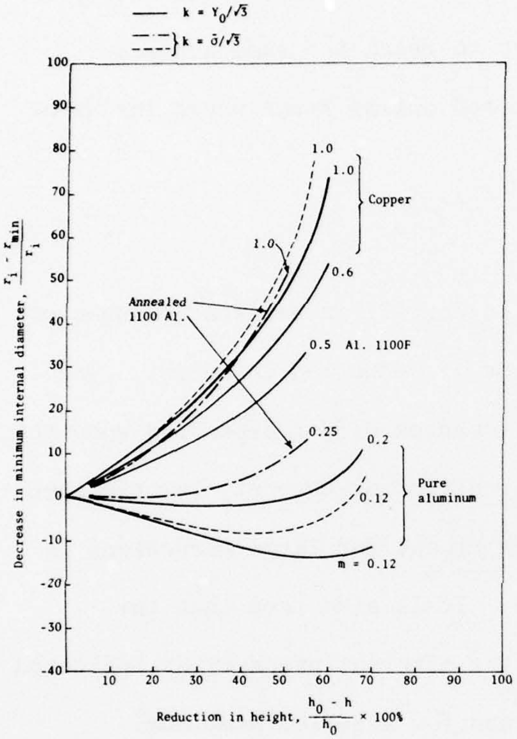

Fig. 27 Changes of minimum internal diameter as functions of reduction in height (finite-element solution).

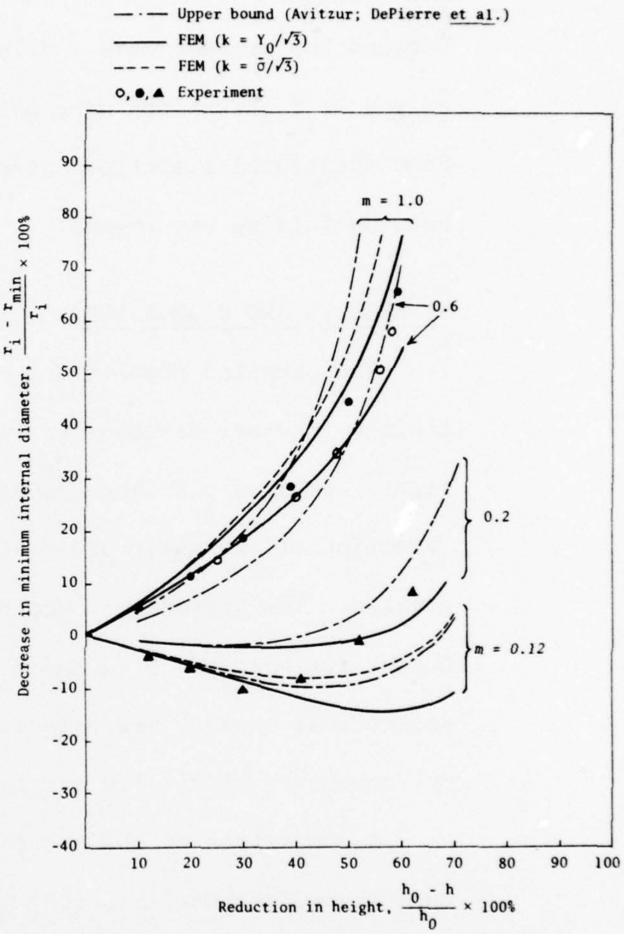

Fig. 28 Comparison of the finite-element solution with the upper-bound solution [49], [50]. Experimental data: ○ - copper [50], ▲ - copper, ● - pure aluminum [48].

plotted in the figure. Interpretation of this particular comparison for low friction is that both solutions suggest the increase of friction as reduction in height increases. However, the interpretation of experimental results for high friction depends on the theoretical solutions. According to the upper-bound solution, the m-value is close to 1.0 in the beginning of compression, and the friction decreases as the deformation increases. On the other hand, the present numerical solution suggests the opposite, namely, the m-value is about 0.6 in the beginning and tends to increase as the reduction in height increases.

In Fig. 29 the present results were compared with another upper-bound solution [51]. It is obvious that this upper-bound solution is not acceptable even for practical applications.

Another comparison was given in Fig. 30. The upper-bound solution for annealed aluminum by Lee and Altan [52] is in good agreement with the present finite-element solution. Experimental data show that the m-values for this experiment remain almost constant, and m = 1 for the dry condition and m = 0.25 under the lubricated condition. The load-displacement relationships computed using these m-values were compared with measurements in Fig. 31. Although the theoretical curves predicted higher load values than the experiment, the present numerical solution gives closer predictions than those by Lee and Altan. Note that the displacement readings in the experiments were not corrected for elastic deflection of the testing machine as reported in [52].

The finite-element method not only provides overall quantities, such as geometrical changes of specimens and load-displacement curves, but also reveals the detail of the deformation characteristics. Fig. 32

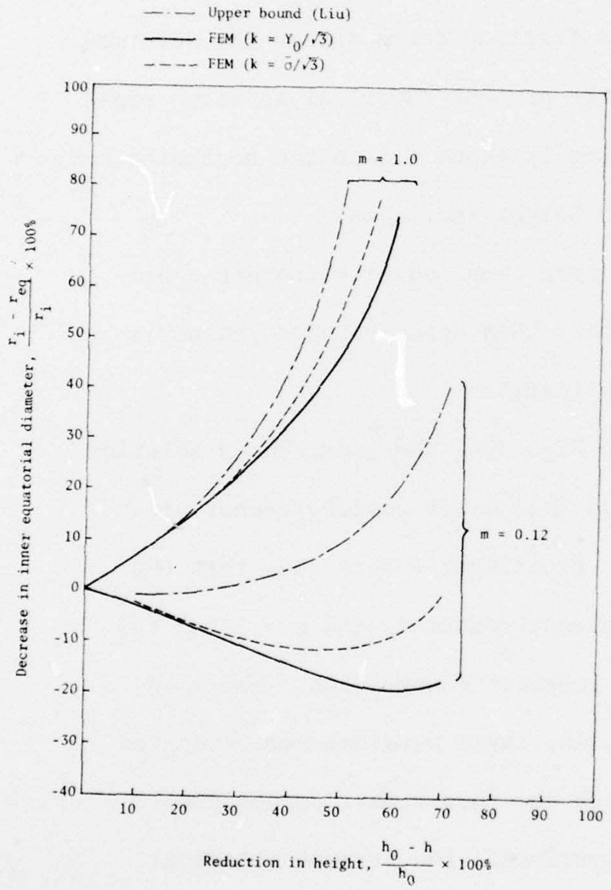

Fig. 29 Comparison of the finite-element solution with the upper-bound solution [51].

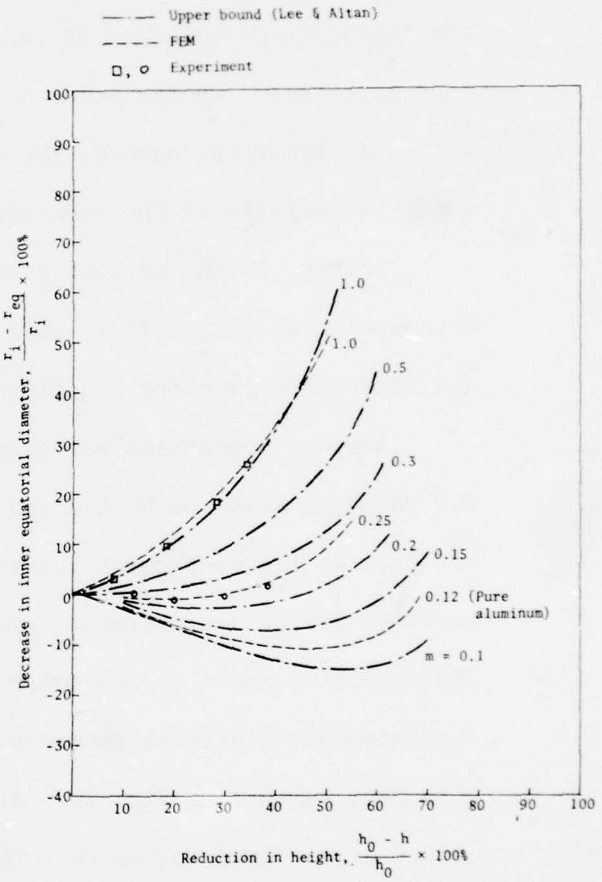

Fig. 30 Comparison of the finite-element solution with the upper-bound solution [52].

AD-A078 987 CALIFORNIA UNIV BERKELEY DEPT OF MECHANICAL ENGINEERING F/G 13/8
RIGID-PLASTIC FINITE-ELEMENT ANALYSIS OF PLASTIC DEFORMATION IN--ETC(U)
AUG 79 C C CHEN , S KOBAYASHI F33615-77-C-5111
UNCLASSIFIED , AFML-TR-79-4105 NL

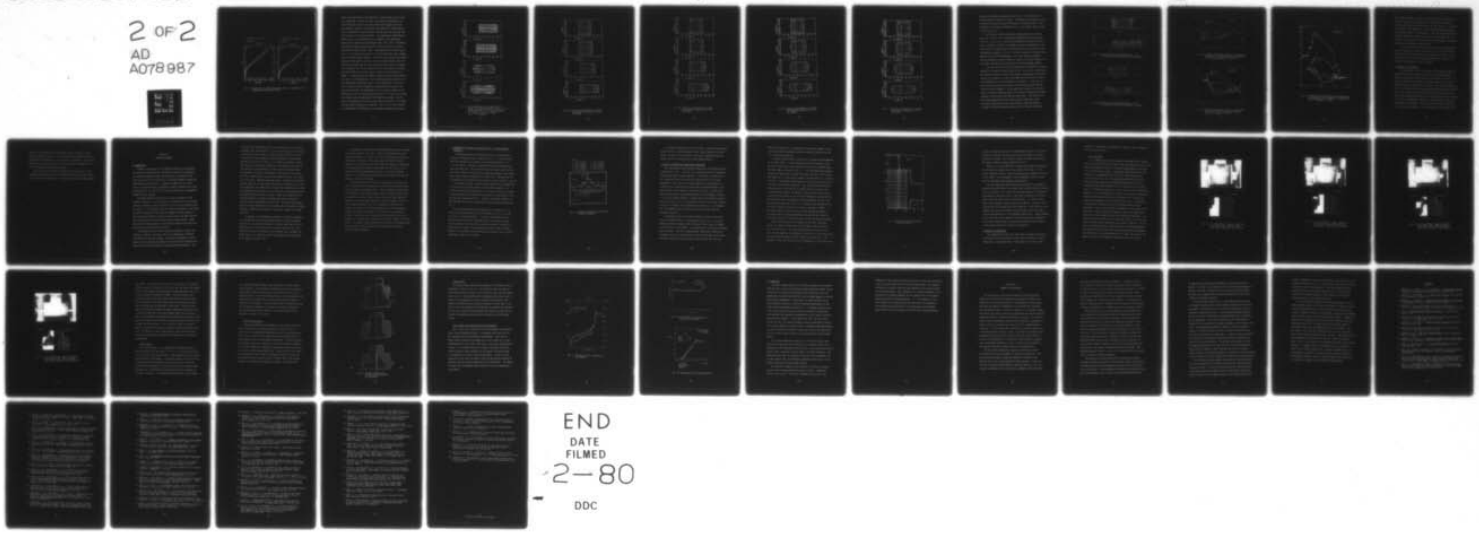

2 OF 2
AD
A078987

END
DATE
FILMED
2-80
DDC

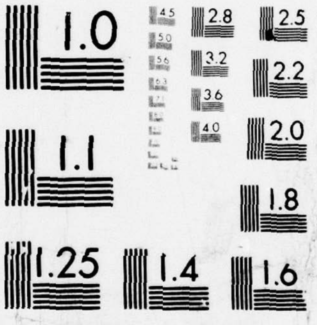

MICROCOPY RESOLUTION TEST CHART
NATIONAL BUREAU OF STANDARDS-1963-A

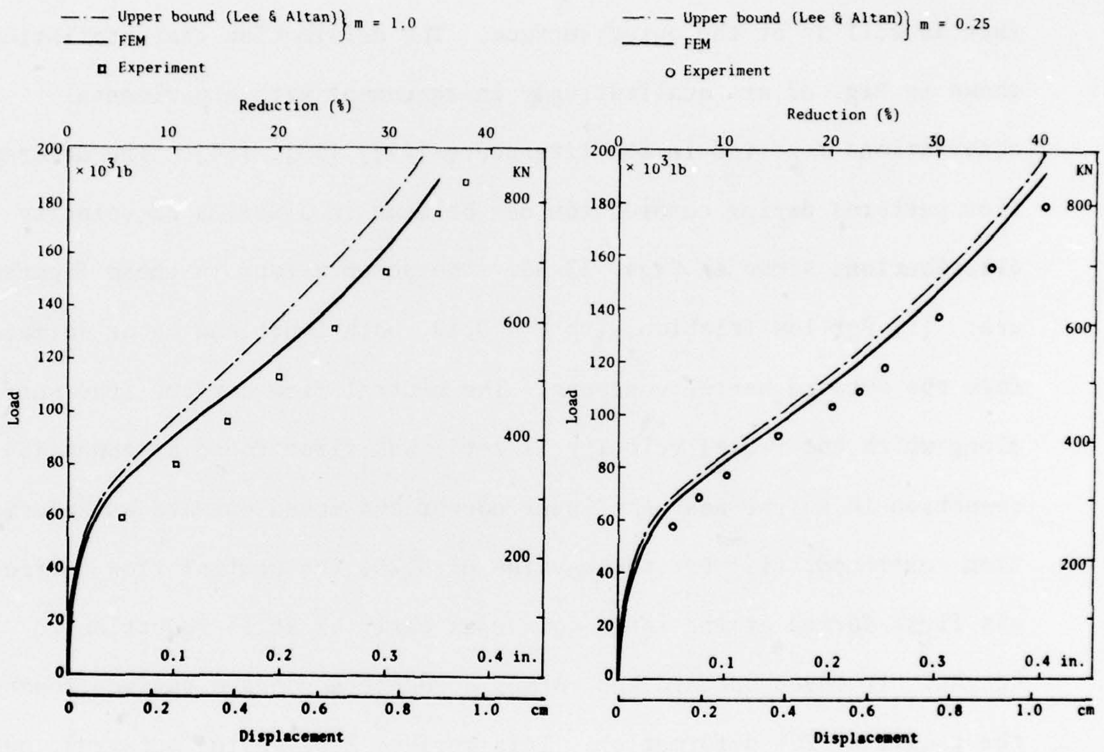

Fig. 31 Comparison for load-displacement curves: experiments and upper-bound solution from [52].

shows grid distortions at 50% reduction in height under various interface conditions. For low friction, the outward flow dominates, but with increasing friction, the neutral flow point appears along the die-workpiece interface, resulting in both inward and outward barreling. Furthermore, for high friction, folding occurs at the inner surface as well as at the outer surface. The deformation characteristics shown in Fig. 32 are qualitatively in agreement with experimental observations reported in the literature [47], [53], [54]. The deformation patterns during compression can be seen in a series of velocity distributions shown in Figs. 33-36. The observations in these figures are: (i) For low friction with m = 0.12, both inner and outer surfaces form the outward barrel contours. The neutral flow surface (the surface along which the radial velocity is zero) was first found at about 45% reduction in height near the inner corner and moved outward as deformation continued; (ii) For the m-value of 0.25, the neutral flow surface was first formed at the inner corner as early as at 3% reduction in height. It moved outward and formed a complete concave surface towards the z-axis at 20% deformation. This surface kept moving outwards, but the shape changed and became convex at 50% deformation. The motions of this neutral surface resulted in an outward barrel contour of the inner surface before 20% deformation, and a flat inner surface at 50% deformation; (iii) For cases of high friction (m = 0.6 and 1.0), neutral flow surfaces moved outward before 20% reduction in height, and then moved in the opposite direction as the reduction increases. The shapes of these neutral surfaces are different: for m = 0.6 a convex surface was formed before 35% deformation, and gradually changed into concave

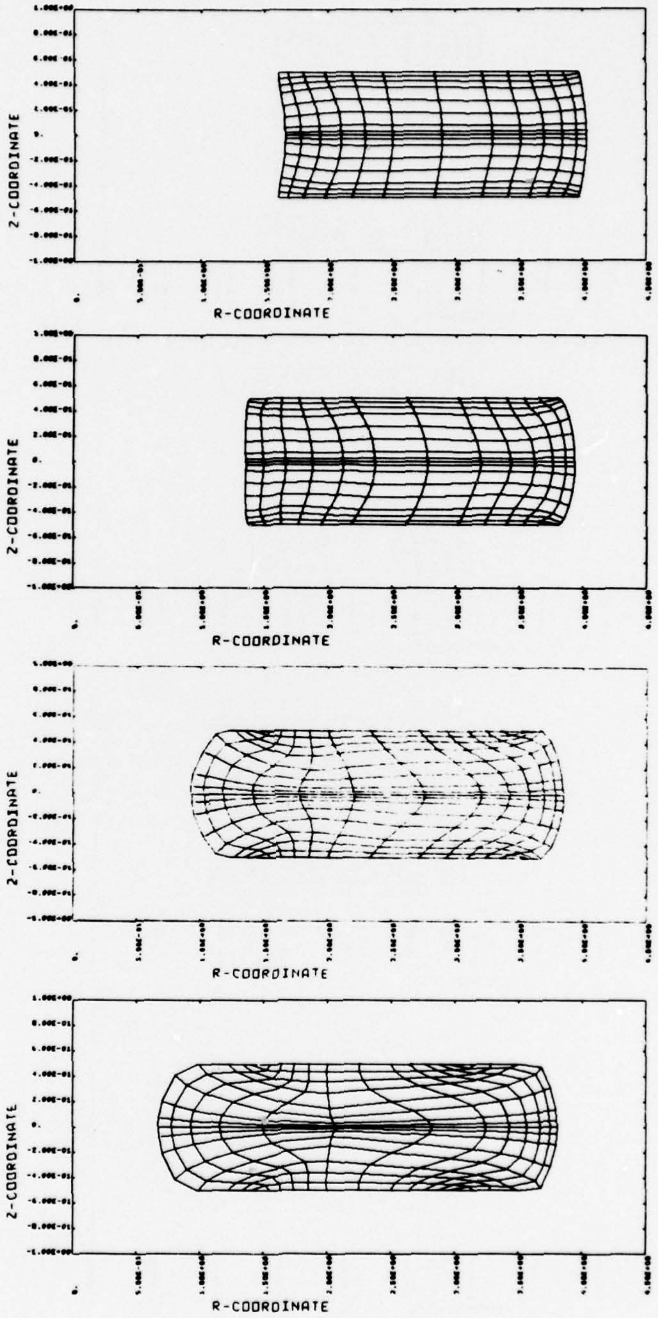

Fig. 32 Grid distortions at 50% reduction in height for various m-values. (a) m - 0.12 (pure aluminum), (b) m = 0.25 (annealed Al. 1100), (c) m = 0.6 (copper), (d) m = 1.0 (copper).

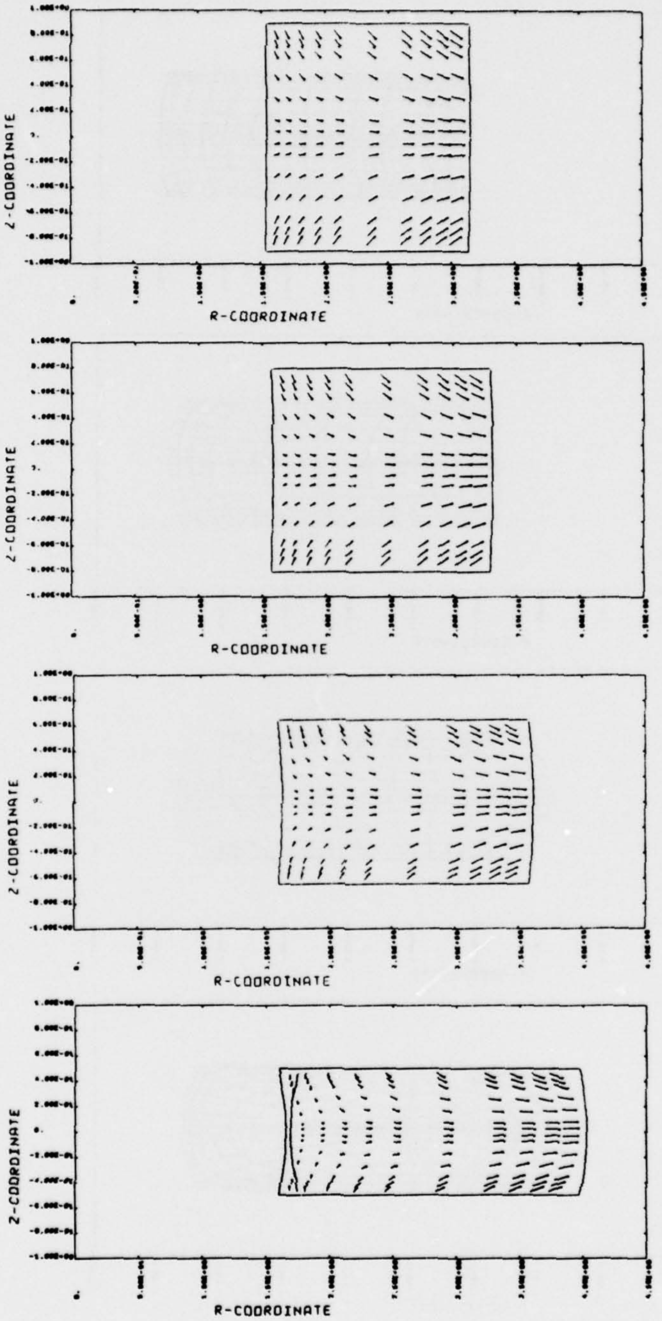

Fig. 33 Velocity distributions at various reductions in height for m = 0.12 ($k = \bar{\sigma}/\sqrt{3}$).

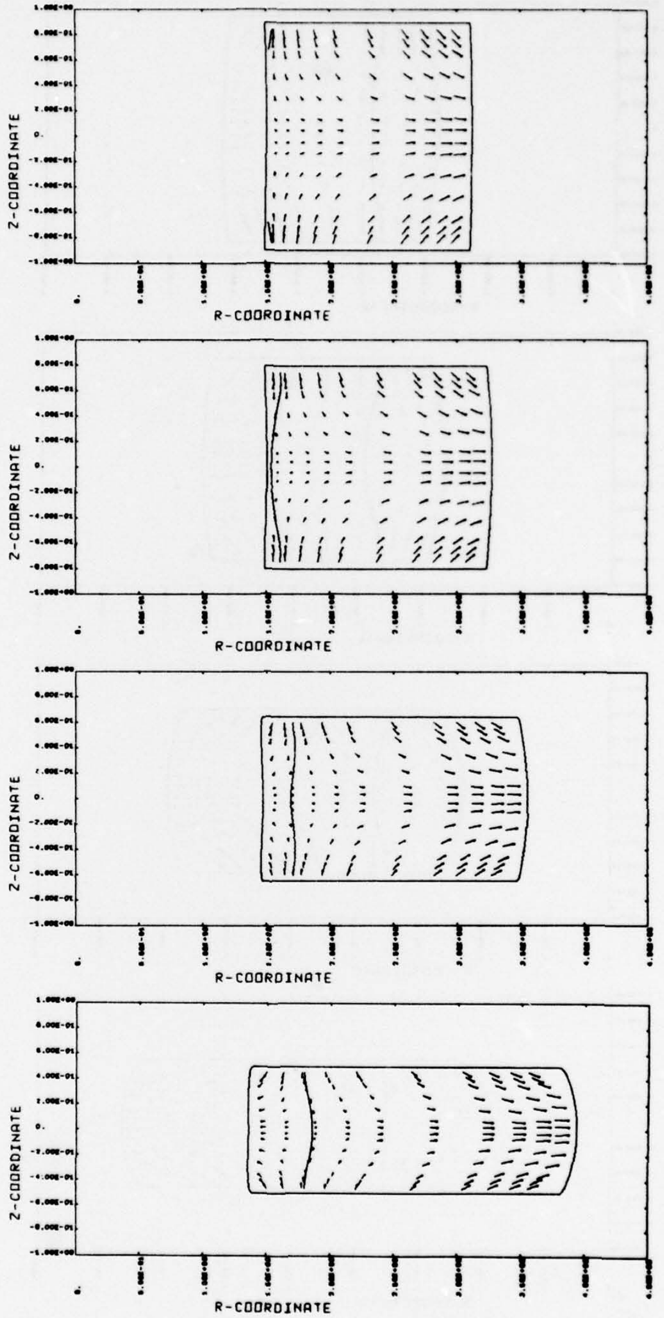

Fig. 34 Velocity distributions at various reductions in height for m = 0.25 ($k = \bar{\sigma}/\sqrt{3}$).

101

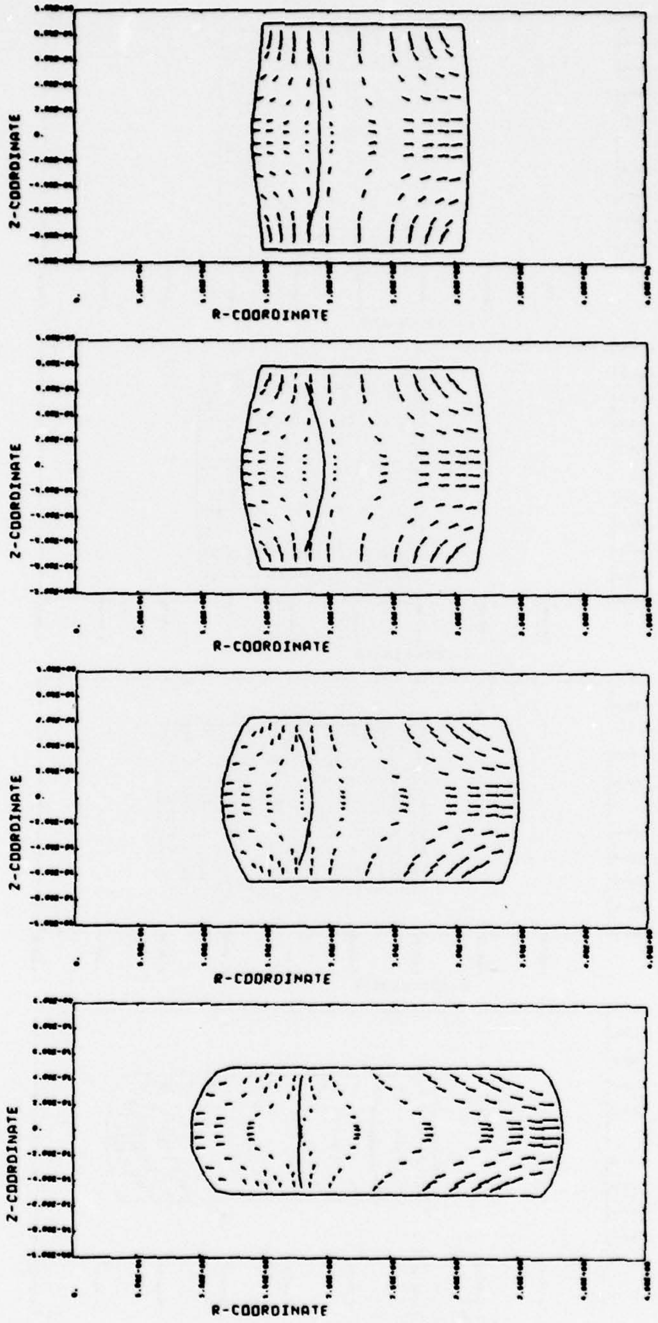

Fig. 35 Velocity distributions at various reductions in height for m = 0.6 ($k = Y_0/\sqrt{3}$).

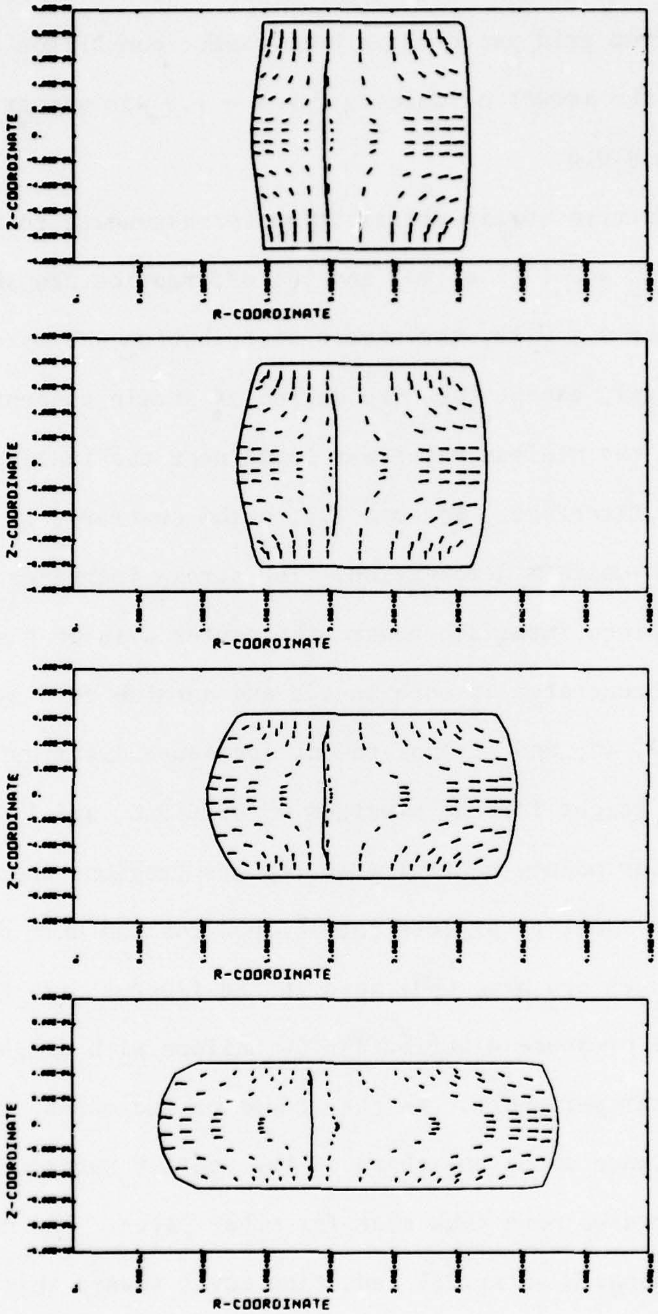

Fig. 36 Velocity distributions at various reductions in height for $m = 1.0$ $(k = \bar{\sigma}/\sqrt{3})$.

surface as deformation continued, while for m = 1.0, the surface remained almost flat during all stages. The formation of folding can also be observed from grid patterns in both cases; comparison shows, at 50% deformation, the amount of folding for m = 1.0 was almost twice as large as that for m = 0.6.

The effective strain distribution corresponding to two extreme cases (m = 0.12 and 1.0) at 20% and 50% deformation are shown in Figs. 37 and 38. For m = 0.12, the strain distribution was more or less uniform, in general, except for some degree of strain concentration at outside corners; the minimum value was found near the inside corner of the die-workpiece interface. For m = 1.0, onthe contrary, it revealed large degrees of non-uniform deformation. The strain increases gradually from die-workpiece interface toward the center axis of the workpiece and was highly concentrated at both inside and outside folding surfaces.

Figs. 39, 40, and 41 show the die pressure distributions at various reductions in height for the m-values of 0.2, 0.6, and 1.0, respectively. The neutral flow point, neutral flow regions (regions where the relative velocity V_R is equal to or less than 0.0005 for the unit die velocity) and folding zones are also indicated in the figures. In Fig. 39, initially the die pressure distribution is uniform with slight increase toward the outer periphery. As the reduction increases, the die pressure at a distance about one-third of the contact surface from the inner periphery increases more than that for other parts. The neutral flow point which appeared after 28% reduction moves toward this point. A so-called "friction hill" was then formed at about 70% reduction in height, in which the peak pressure was at the neutral flow point.

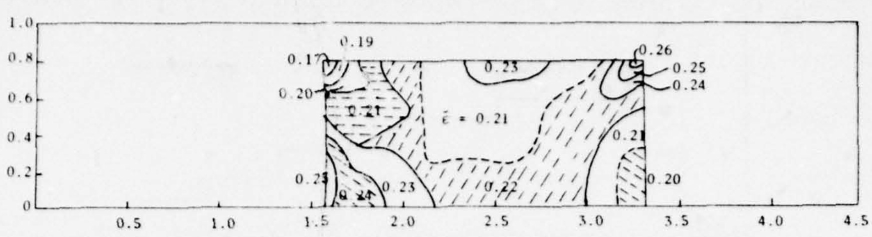

20% reduction

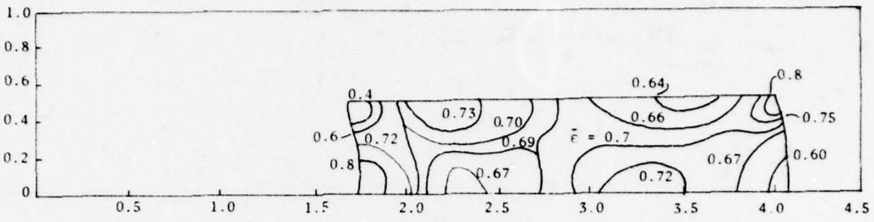

50% reduction

Fig. 37 Effective strain distributions for m = 0.12 (k = $Y_0/\sqrt{3}$) at 20% and 50% reductions in height.

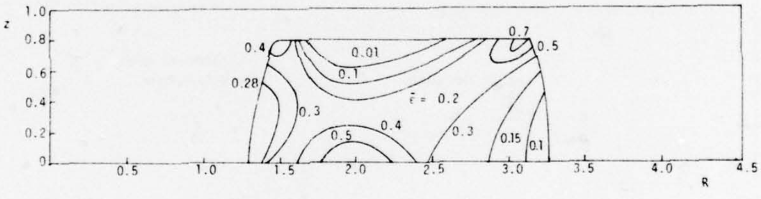

20% reduction

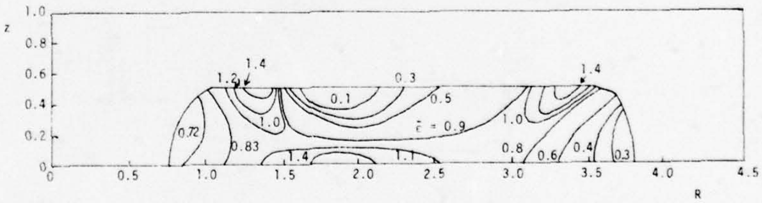

50% reduction

Fig. 38 Effective strain distributions for m = 1.0 (k = $Y_0/\sqrt{3}$) at 20% and 50% reductions in height.

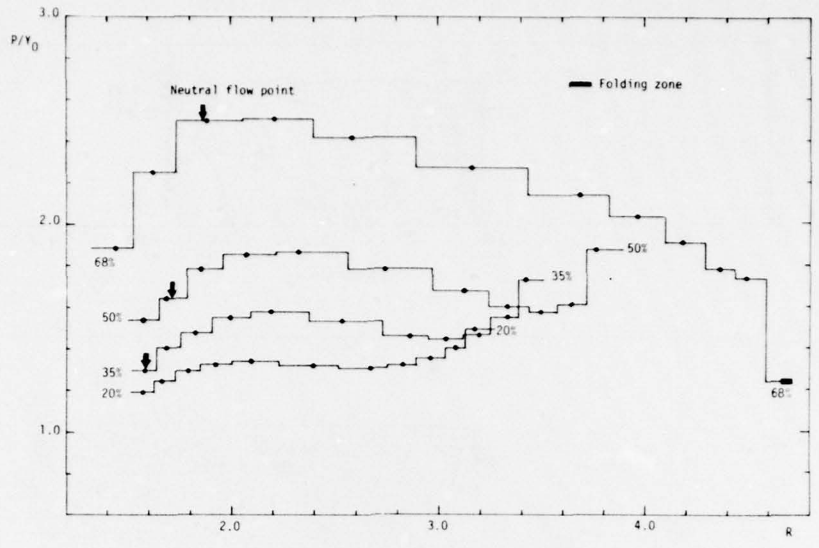

Fig. 39 Pressure distributions along the die-workpiece interface at several reductions in height for m = 0.2 (pure aluminum, $k = Y_0/\sqrt{3}$).

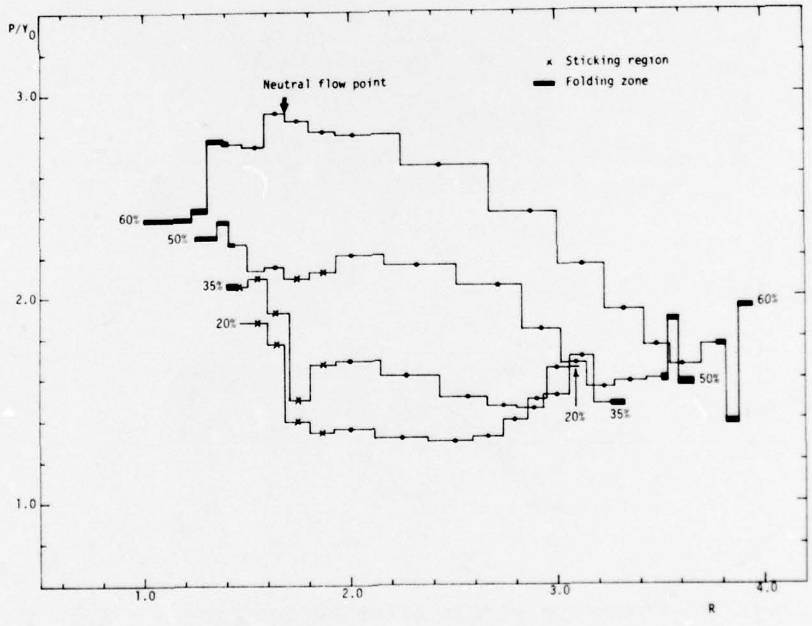

Fig. 40 Pressure distributions along the die-workpiece interface at several reductions in height for m = 0.6 (copper, $k = Y_0/\sqrt{3}$).

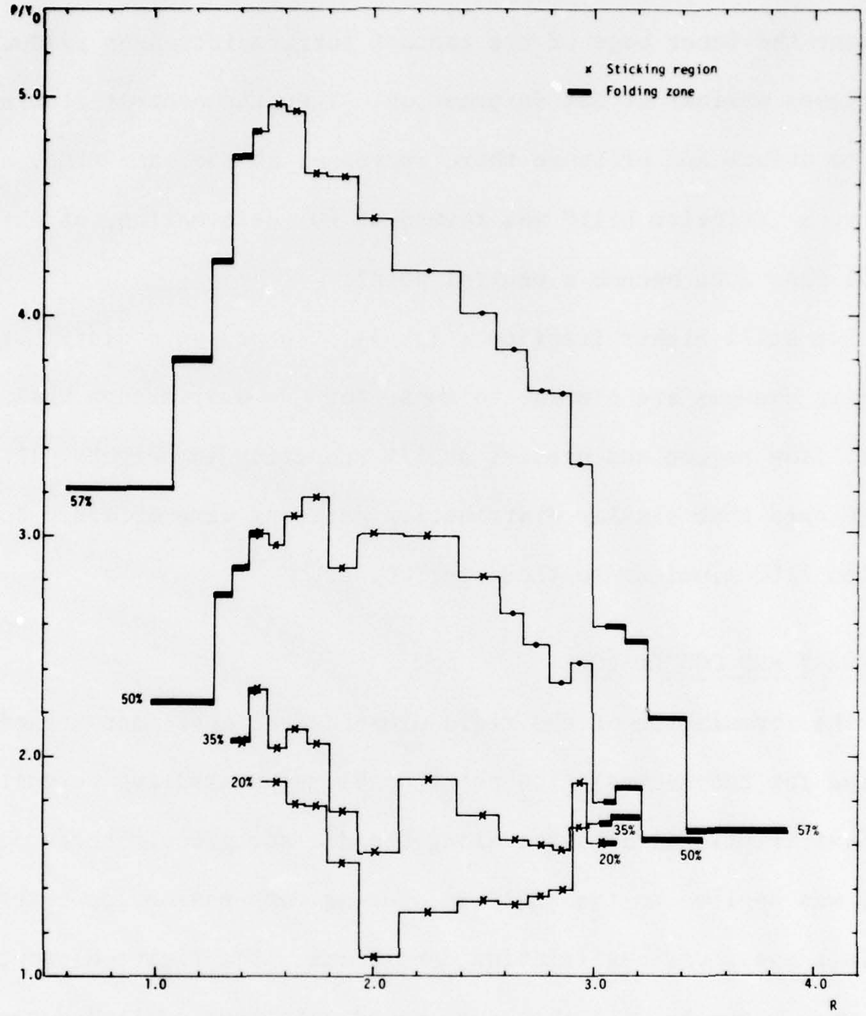

Fig. 41 Pressure distribution along the die-workpiece interface at several reductions in height for m = 1.0 (copper, $k = \bar{\sigma}/\sqrt{3}$).

With higher friction (m = 0.6), the initial pressure distribution is uniform (not shown in the figure), but then the pressure becomes minimum inside the neutral flow region, as seen in Fig. 40. The pressure near the inner edge of the contact surface increases gradually and becomes maximal at 35% deformation. Then the neutral flow region began to deform and pressure there increases at the same time, and finally, a "friction hill" was formed at 60% deformation, at which the neutral flow zone became a neutral point.

For still higher friction (Fig. 41) the pressure distributions and their changes are similar to those for m = 0.6, except that the neutral flow region was present at 57% reduction in height. It must be mentioned that similar distribution patterns were obtained for annealed 1100 aluminum to those for copper.

5. SUMMARY AND CONCLUSIONS

The formulation of the rigid-plastic finite-element method was modified for the neutral flow point problems by assuming velocity dependent frictional stresses along the die-workpiece interface. The method was applied to the analysis of ring compression for several materials under various friction conditions. The finite-element solutions were compared with the upper-bound solutions published previously. It was shown conclusively that the solutions by Lee and Altan [52], among other upper-bound solutions, are closest to the present solutions in terms of the geometrical changes of ring specimens and the load-displacement relationships. The present finite-element solutions revealed the detailed mechanics in ring compression, particularly with respect to the formation of neutral flow points, neutral flow zones, and free surface barreling. It was found that the dominant factor for deformation characteristics is friction at the interface. The materials property has a significant effect on the geometrical changes but not on the die pressure distribution patterns.

The success of the present formulation for the analysis of ring compression promises solutions of the other neutral flow point problems, such as rolling and forging, by the rigid-plastic finite-element method.

Section VI

CLOSED-DIE FORGING

1. INTRODUCTION

Forging in closed dies is an important operation in the shaping of metals into useful objects. The process involves the compression of a specimen between the upper and lower dies, restriction of the metal flows to fill the closed cavity, and flash formation through the gap between the closing dies. In order to completely fill the die cavity, more material than is apparently needed is normally used in the forging process. The flash due to this excess material is subsequently trimmed from the forging.

The flash formation itself can also create resistance to the escape of materials. It will build up a very high value of the forging load and, therefore, force the material to fill all the recesses of the die cavity. It is important, then, to adjust the dimension of the flash so that the extrusion of the materials through the flash opening is more restrictive than the filling of the die cavity, and that the forging load required is still not high enough to break the dies. Thus, the aim of the flash design is to provide the minimum flash required to give the best filling of the die cavity.

The prediction of the load in closed-die forging is usually very difficult to obtain. Therefore, most of the mathematical solutions are suitable for open-die forging. Prandtl [57] considered an ideal plastic solid in plane-strain between two rough dies and obtained solutions for the stress distribution and average forging pressure. This case was later considered by Hill, Lee, and Tupper [58], Green [59], Alexander [60], and Bishop [61]. For closed-die forging at the finishing stage, the actual plastic deformations were found mainly at the flash portion, with exceptions of minor adjustments of the forging material to fill the die cavity; it is therefore reasonable to apply the results of the open die forging of a flat plate or solid disk to the studies of flash deformation in the closed-die forging process. The approximate solutions for forgings of flat plate or solid disk, based on a simple state of stress, were proposed by Seibel [4], Nadai [62], Sachs [63], Schroeder and Webster [64]. Solutions of closed-die forging, based on the slab method, were given by Kobayashi et al. [65] and by Kobayashi and Thomsen [66], in which they assumed that all plastic deformation are restricted to the flash and to the materials of the forging from which the flash is formed. More recent applications of the slab analysis to closed-die forgings were made by Altan and Fiorentino [67] and Akgerman and Altan [68]. The upper-bound methods based on certain admissible velocity fields were also applied to forging problems by Johnson [69], Kudo [70], and several authors in the USSR [73]-[74].

In addition to the mathematical analysis, an empirical approach to the prediction of closed-die forging load has also been proposed by Schey [71], in which the formula $P = \bar{\sigma}A_tC_f$ is used, where P is the forging load, $\bar{\sigma}$ is the average flow stress of the metal, A_t is the cross-section area of the forging at the parting line, including the flash, and C_f is a constraint factor which depends on the complexity of the shapes (see Spies [72]).

Experimental studies on the closed-die forgings can also be found in several references [75]-[78]. Gubkin [75] and Semenov [76] conducted experiments to determine the zones of various kinds of plastic deformation in forgings. They investigated the effect of flash geometry on the maximum load for the closed-die forgings. Kondratenko [77] and Mertens [78] conducted experiments for the studies of grid distortion during the deformation process in closed-die forgings. Kasuza et al. [79] observed the material flow in plane-strain and axisymmetric rim-web type forgings.

The present studies utilized the same material (pure lead) and dies as those used in the experiments of plane-strain closed-die forgings by Lyapunov and Kobayashi [80]. Their experimental observations were compared with the present finite-element solutions which include grid patterns, velocity fields, forging loads, and flash formations. Although the finite-element analyses of open-die forgings, with relatively simple geometries, have been conducted by Zienkiewicz and Godbole [25] and Price [22], the applications of these techniques to problems of closed-die forgings is still practically nonexistent because of the difficulties in dealing with the complexities of die geometries, the large rigid portions, and the rapid changes in velocity fields. The present study revealed the possibility of the applications of rigid-plastic finite-element method to the analysis of these extremely complex problems.

2. EXPERIMENT BY LYAPUNOV AND KOBAYASHI [80]: DIE AND WORKPIECE GEOMETRIES

A schematic diagram of the apparatus used in the experiment by Lyapunov and Kobayashi [80] is shown in Fig. 42. A 2-inch (5.08 cm) long lead specimen with a square cross-section measuring 1.3 in. × 1.3 in. (3.30 cm × 3.30 cm) is placed inside the cavity between the upper and lower dies. The cross-section of the cavity, when two dies are closed, consists of portions of a tapered rectangular cross-section and a tapered flange extended from its upper face. Specifications of the dimensions of the upper and lower dies are given in detail in Fig. 42.

As described in [80], the plane-strain constraint was accomplished by the use of two parallel platens, one of which was made of 1-in. (2.54-cm) thick tublex tempered glass. In order to minimize the effect of friction between the specimens and platens, each end surface of the specimens was lubricated with oil. However, the contact surfaces of the specimens and dies were cleaned with acetone and dried before each test.

The forging operations were performed by a 160,000-lb (72.7 T) Tinius Olsen testing machine with a slow speed of 0.05 in. (1.27 mm) per minute, at room temperature. A series of photographs of grid patterns were taken and the load-displacement curves were recorded. The grid patterns were then used to obtain the particle velocities by projecting the negatives of the photographs onto a sheet of tracing paper of 10X enlargement and connecting the grid points for the several incremental stages of the forgings.

Dimensions:

a: 0.34 in. (0.864 cm)
b: 0.375 in. (0.953 cm)
c: 0.75 in. (1.905 cm)
d: 0.782 in. (1.986 cm)
e: 1.2 in. (3.048 cm)
f: 1.207 in. (3.066 cm)
g: 1.75 in. (4.445 cm)
h: 1.76 in. (4.471 cm)

i: 0.5 in. (1.270 cm)
j: 0.46 in. (1.168 cm)
k: 0.35 in. (0.889 cm)
ℓ: 0.5 in. (1.270 cm)
m: 0.28 in. (0.711 cm)
n: 0.17 in. (0.432 cm)
o: 0.32 in. (0.813 cm)

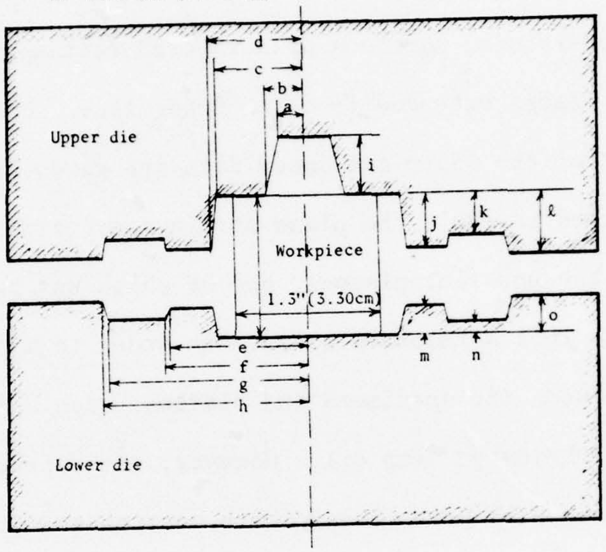

Fig. 42 Schematic diagram of plane-strain closed-die forging.

The results obtained from this experiment, including grid patterns, velocity fields, load-displacement curves, flash dimensions, and the height variations of the specimen, were used in comparison with the present results of rigid-plastic finite-element analysis.

3. ANALYSIS TECHNIQUE AND COMPUTATION CONDITIONS

The rigid-plastic finite-element formulation with modified penalty constraint (Eq. (18)) was used in the present analysis of closed-die forging under plane-strain conditions. The problem is characterized by a large near-rigid zone along the center portion of the cavity, especially at the initial die filling stage; this rigid portion is subjected to a large portion of force-free prescribed boundary at the upper surface of the workpiece inside the die cavity. To deal with this type of problem, the proposed method of rigid treatment (Section II.2) was used, which assigns a limited value of the effective strain rate $\dot{\bar{\varepsilon}}_0$ (say, $\dot{\bar{\varepsilon}}_0 = 10^{-3}$) in the equation of stress-strain rate relationship for all elements lying inside the rigid zone, i.e., for elements with the computed value of effective strain rate $\dot{\bar{\varepsilon}}$ less than the assigned value of $\dot{\bar{\varepsilon}}_0$.

The specimen used in the present analyses is made of pure lead which is characterized by a rigid-perfectly plastic (i.e., non-work-hardening) material behavior with the constant flow stress Y_0 assumed to be 2,500 psi (17.236 MN/m^2). Two extreme cases of friction conditions were considered: the first assumed perfect lubrication between the interfaces of the die and workpiece so that no frictional force exists; the second assumed a sticking condition which states that once the material touches the die, the material is completely adhered to the die and any relative movement between the material particle and the die is therefore prohibited.

The mesh system initially consists of 208 elements interconnected at 238 nodal points. A very fine mesh was used for elements lying below the inner corner of the upper die, and also for elements along the free surface, as shown in Fig. 43. The non-steady-state forging process was analyzed by a step-by-step manner with the size of increment equal to 1% of the initial height of the specimen (i.e., 0.013 in.; 0.033 cm). An arbitrary initial guess of the velocity fields was provided for the first-step iterations. The solution obtained from the previous step was then used as an initial guess for the next step. As deformation continued, the material along the free surface moved towards the side surface of the die, and subsequently touched the die. For steps where the die-workpiece touching phenomenon did not occur during the previous step, only 5 to 7 iterations were required for the solution in order to achieve an accuracy of $\|\Delta \underset{\sim}{u}\|/\|\underset{\sim}{u}\| \leq 0.00008$. It was found, however, that the velocity fields changed dramatically for steps when the touching phenomenon occurred, and the number of iterations required to achieve the same accuracy increased accordingly.

After the side cavity of the upper die was almost completely filled, the material inside the lower die began to move sideward to fill the lower cavity. The flash formation started when the side cavity of the upper die was completely filled, and it became appreciable once the material touched the upper corner of the lower die. This happened at about the 27th step of the deformation in the present cases.

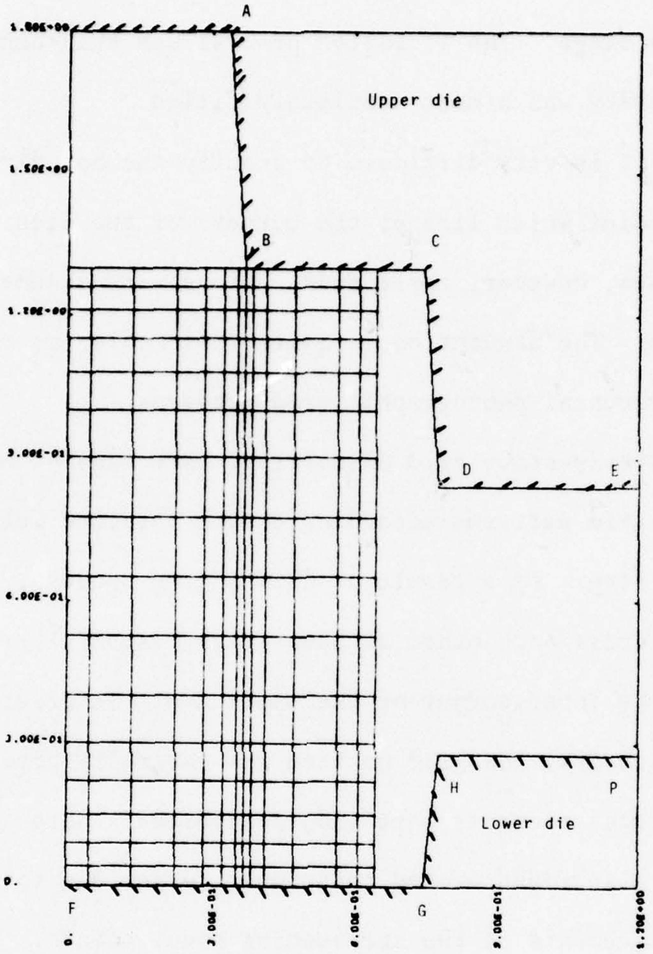

Fig. 43 Mesh system for plane-strain closed-die forging.

In order to properly deal with the deformation mechanics of the flash formation, three more horizontal grid lines were added to the mesh system at this stage. The iteration process was than continued until the central cavity was almost completely filled.

Usually, it is very difficult to specify the boundary conditions of the nodal point which lies at the corners of the dies. In the present analyses, however, these nodal points were assumed to be fixed at the corners. The assumption is quite reasonable, as may be seen from the experimental photographic grid patterns.

The non-steady-state grid distortions were made by continuously modifying the grid patterns according to the obtained velocity distributions at each step. As a result of this adding process, the elements may happen to cross each other at some stage, especially for the elements around the inner corner of the upper die. In order to avoid these cross elements, the grid pattern was carefully checked at every step and the cross elements were then readjusted. Note that very tiny elements were also found around this inner corner due to the large relative displacements of the surrounding nodal points. These problems may be solved by a more elaborate device of the element arrangement, or by using a mesh system with mixed type elements, but this aspect of the problem remains for further investigations.

4. RESULTS AND DISCUSSION

The computational results for both cases of perfect lubrication and sticking friction were made in terms of grid distortion, velocity distribution, load-displacement, flash geometry, and axial height variations. Experimental observations in [80] were used in comparison with the present results.

Grid distortion

Fig. 44 shows a series of grid patterns obtained from the computational results at the 6th, 14th, 26th, 30th, and 32nd steps, respectively. Each step represents a 0.013-in. (0.033-cm) displacement of the upper die (the lower die was fixed). Experimental observations of the grid distortions, at approximately the 5th, 16th, 23rd, and 33rd steps, are also shown in Fig. 44. The comparison shows that the computed results are very similar to the experimental observations, and the experimental frictional condition falls in between these two extreme cases. The following features were made according to the provided grid patterns: (i) At the beginning of forging, the specimen is compressed between the upper and lower dies and the material at the upper die corners flows sideways to fill the side cavity, while a large portion of the material along the center of the specimen remains almost stationary. For the case of perfect lubrication, the movements of the nodal points along the upper die surface is faster than those nodal points at the side surface because of no frictional constraints. The corner cavity of the upper die was completely filled, at the 8th step, before the nodal points touched the side surface of the die. For the cases of sticking friction, on the other hand, the folding phenomenon was found first and the side nodal point touched the die subsequently. The sticking friction condition resulted in a small die cavity at the upper die corner, which cannot be completely filled, as shown in

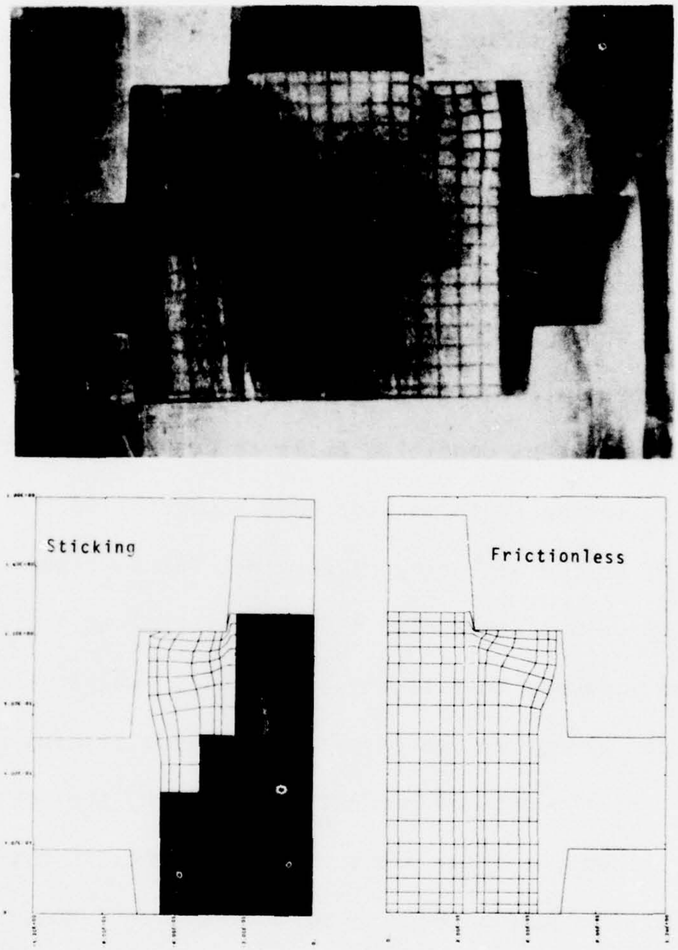

Fig. 44 (a) Grid patterns. Upper: experiment (5th step); Lower: FEM (6th step, dark portion indicates rigid elements).

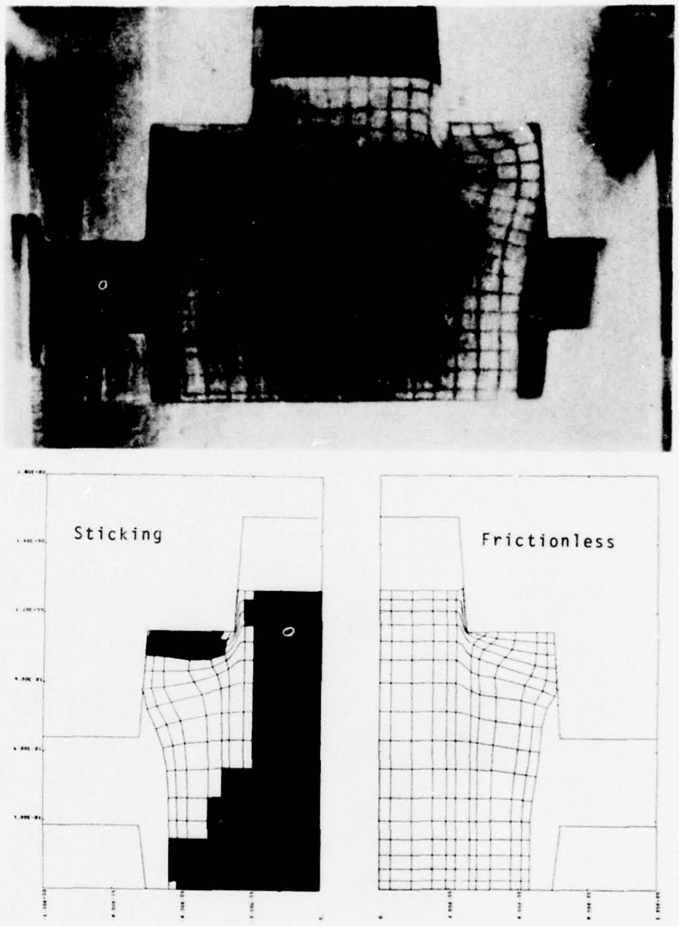

Fig. 44 (b) Grid patterns. Upper: experiment (16th step); Lower: FEM (14th step, dark portion indicates rigid elements).

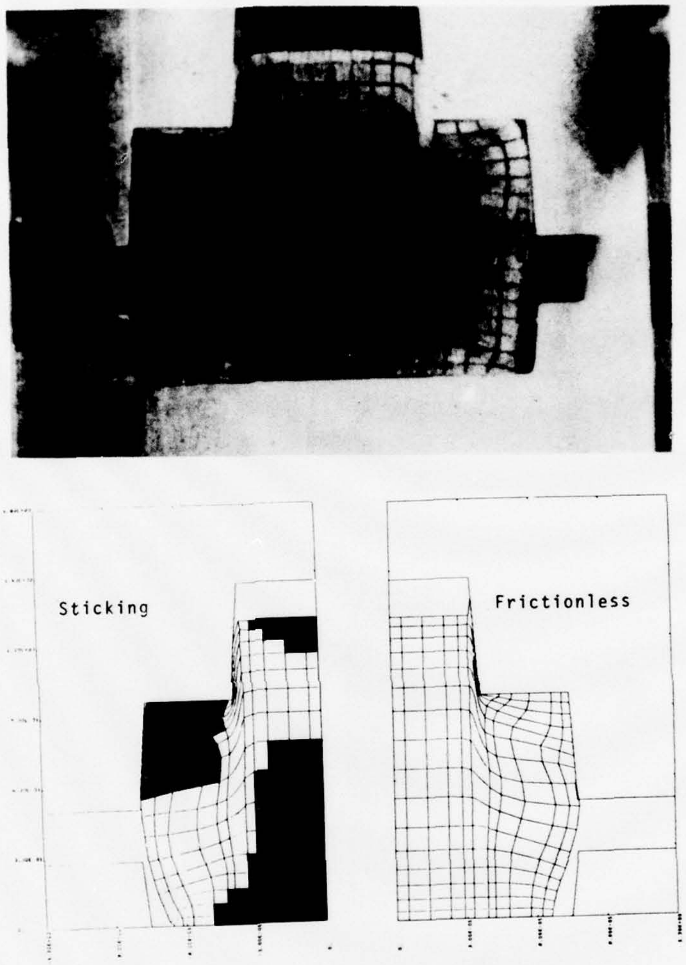

Fig. 44 (c) Grid patterns. Upper: experiment (23rd step); Lower: FEM (26th step, dark portion indicates rigid elements).

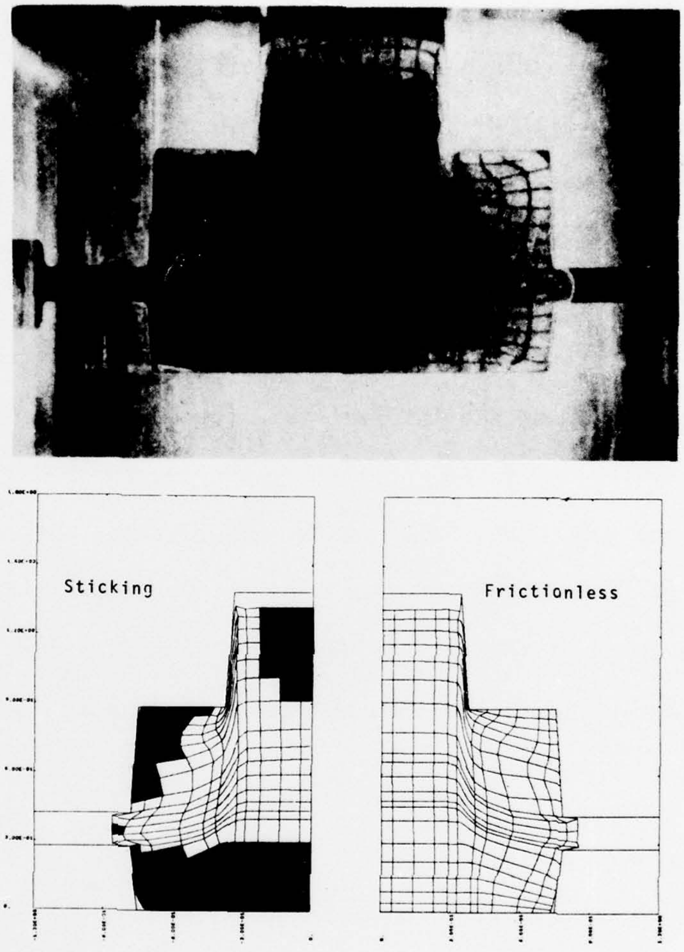

Fig. 44 (d) Grid patterns. Upper: experiment (33rd step); Lower: FEM (32nd step, dark portion indicates rigid elements).

Fig. 44(b). (ii) When the side cavity of the upper die is essentially filled, which was at the 26th to 27th steps for both cases, the material starts to flow through the gap between the upper and lower dies, and a small portion of the flash is formed. This metal flow is then restricted, and the filling process of the lower die cavity becomes more significant. Note that a small cavity at the lower die corner was still found, at the 32nd step, in both cases. (iii) When both upper and lower side cavities are almost completely filled, which was at about the 32nd step, the process becomes similar to extrusion in which a large portion of the materials are forced to flow upward to fill the central cavity; the flash portion between the upper and lower dies increases at the same time. (iv) At the final stage, the central cavity is completely filled and the process involves only flash formation. The analysis of this stage requires a very fine mesh system inside the flash portion; and this has not been done in the present investigation.

Rigid regions

The rigid elements, i.e., elements with the computed value of effective strain rate less than 10^{-1} ($\dot{\bar{\varepsilon}} \leq 0.1$), are also shown in Fig. 44, for the case of sticking friction. The dark portions in the figure represent these rigid elements. For earlier stages up to the 7th step, a large portion of the workpiece remains rigid, and the deforming elements were found mainly at the side portion of the workpiece under the upper die; this deforming region enlarges and moves downward as the process continues. For deformations from the 10th to 26th steps, the original deforming elements under the upper die surface become rigid gradually; this rigid portion enlarges and finally occupies the entire upper corner at the 26th step, as shown in Fig. 44(c); the deforming region, on the other hand, shifts to the lower portion of the workpiece and the elements at the lower corner start to deform, as indicated in the figures. Then, the lower cavity is completely filled and the deforming elements at the lower corner become rigid again; the deforming region is now mainly at the central portion of the workpiece, as shown in Fig. 44(e).

Velocity distribution

Velocity distributions corresponding to grid patterns described above, for the case of sticking friction, are given in Fig. 45, together with the experimental measurement of the flow patterns from [80]. Fig. 45 shows that the computed velocity distributions are in good agreement with the experimental observations. Material particles at the upper corner moves sideways in the earlier stages and changes its direction downward in subsequent stages when the particle velocity of the lower corner becomes appreciable. The particles at the central portion under the inner corner of the upper die start to rotate and move upward when the lower die cavity is almost filled; the particle velocity at the lower corner becomes zero again, at the same time.

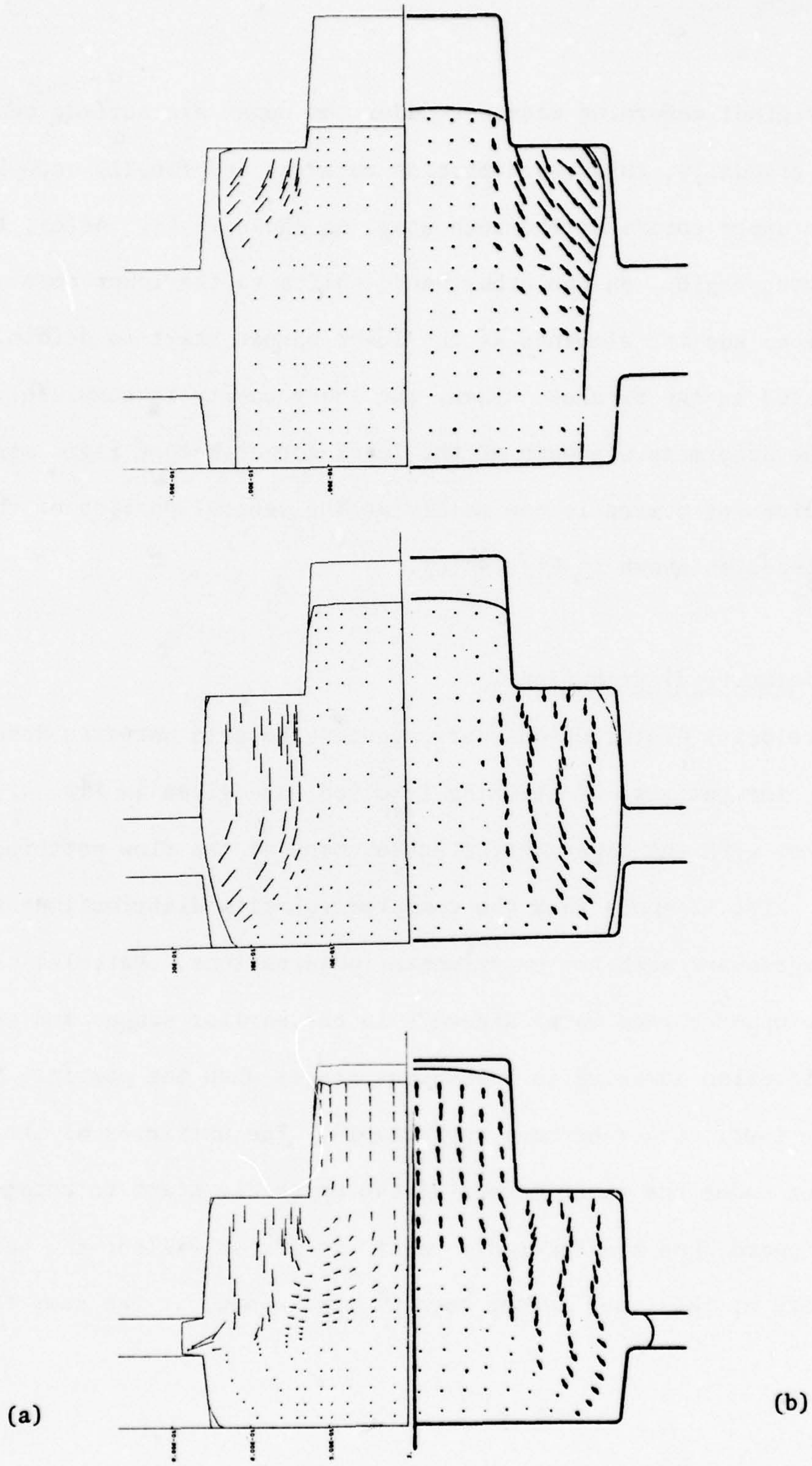

Fig. 45 Velocity distributions;
(a) FEM (sticking friction);
(b) experiment.

Forging loads

The forging loads obtained from computation are compared with the experimental results in Fig. 46. The predicted values for both perfect lubrication and sticking friction cases are lower than the experimental values. The deviations may be explained by the excess load required in the experiment in order to overcome the frictional force between the specimen and the constraining plates at both ends; it may also be due to the additional load required in squeezing the materials to flow into the small cavities between the constraint plates and the die and in maintaining the plane-strain conditions for the forging process.

Axial height variations and the flash dimensions

Fig. 47 gives the variations of the axial height of the workpiece under various deformation stages. The computational results are in good agreement with the experimental measurements. Note that the height remains practically unchanged for the die stroke up to 10 mm (approximately the 31st step); after this, a relatively large particle velocity in the upward direction was found at the upper half of the central position, which resulted in an increase of the axial height of the workpiece, as can be seen from the figure. In Fig. 48, the geometries of the flash are shown in terms of gap distance between the upper and lower dies and the dimensions of the flash width. The comparison shows that the computed results match well with the experimental measurements.

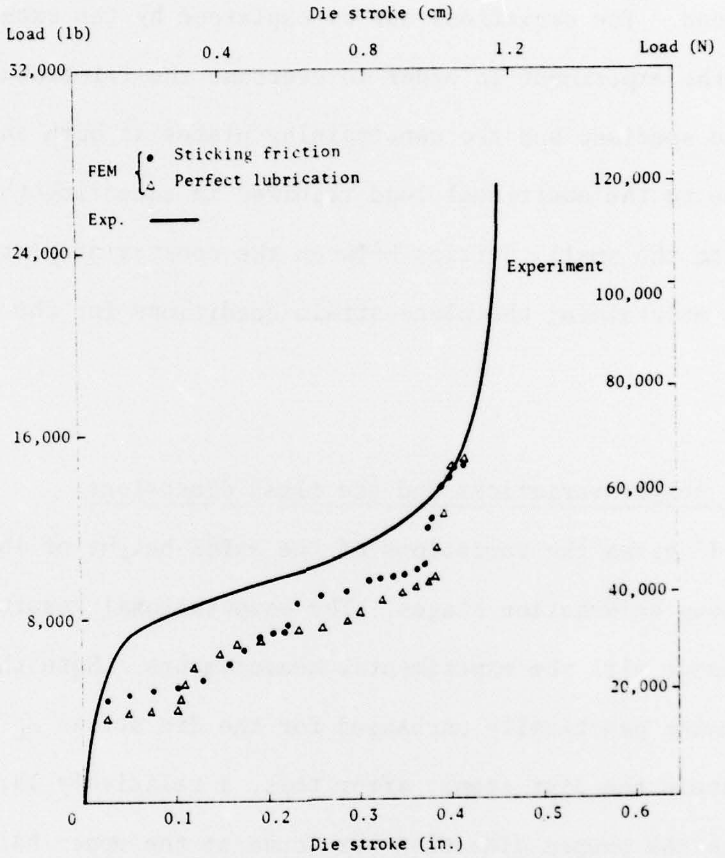

Fig. 46 Forging loads as a function of die stroke.

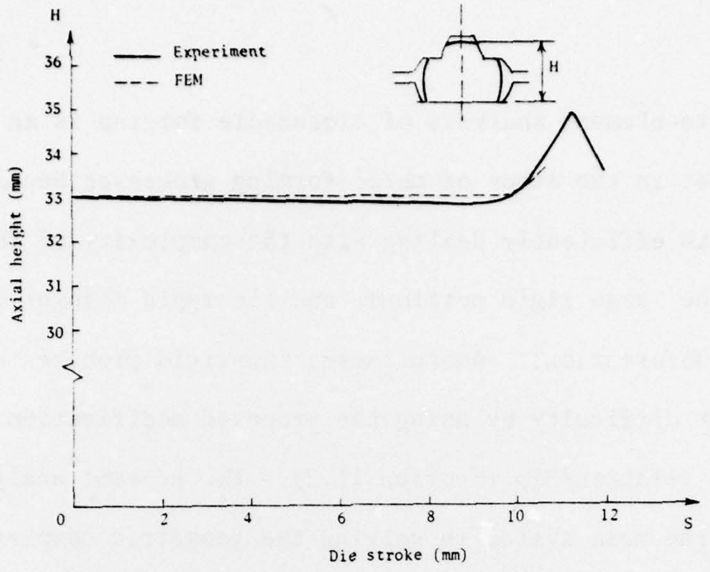

Fig. 47 Axial height of the specimen as a function of die stroke.

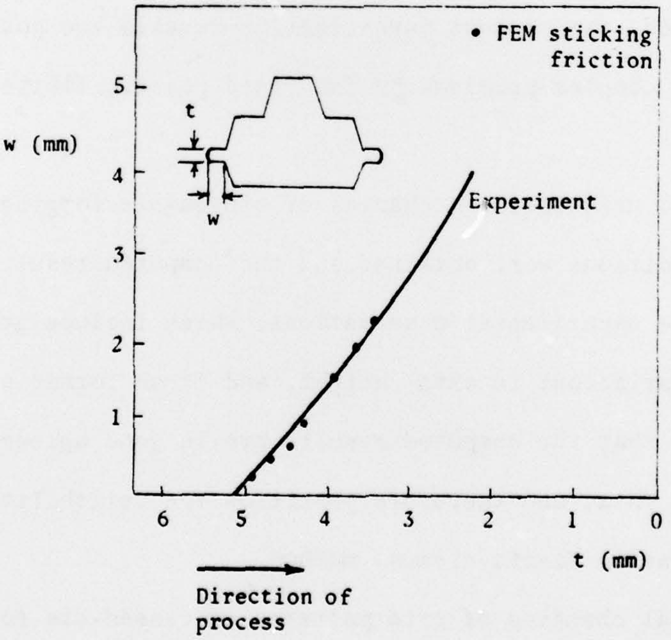

Fig. 48 Comparison of the flash dimensions.

5. CONCLUSION

The finite-element analysis of closed-die forging is an extremely difficult facet in the study of metal-forming processes because of the difficulties in efficiently dealing with the complexity of the die geometries, the large rigid portions, and the rapid changes in velocity field during deformations. Among these, the rigid problems can be solved without difficulty by using the proposed modification of the stress-strain relationship (Section II.2). The present analysis utilized a very fine mesh system in solving the geometric complexities. Grid patterns were examined and readjusted at every step to avoid the possible cross elements. It was found that, when the nodal points touched the die, the iteration numbers increased dramatically because of the rapid changes in velocity fields. Although further improvements are still required, the present investigation reveals the possibility of solving these complex problems by the rigid-plastic finite-element method.

The detailed deformation mechanics of closed-die forging under plane-strain conditions were obtained and the computed results were compared with the experimental observations, which include grid patterns, forging loads, variations in axial height, and flash formations. The comparison shows that the computed results are in good agreement with the experimental data, and therefore justifies the reliability of the present rigid-plastic finite-element method.

The continual changing of grid patterns in closed-die forgings revealed the following deformation stages in detail: compression filling, and extrusion. The plastic deformation portions of the workpiece at each stage were further explained in terms of the distributions of rigid elements and the velocity distributions. The detailed information on forging loads and flash geometries were also furnished by the present method. This information is extremely important in the selection of a suitable geometry for the workpiece and in the proper design and control of flash dimensions. It is of interest to note that although the present analysis was made under the assumption of two extreme friction conditions, the rigid-plastic finite-element method itself can also incorporate any other friction representation.

Section VII

SUMMARY AND CONCLUSIONS

The rigid-plastic finite-element method has been successfully applied to the problems of axisymmetric extrusion and drawing, ring compression, and closed-die forging. The formulation of the minimum principle and methods of imbedding the incompressibility constraint were discussed in detail. Particular attention, in the finite-element formulation, was given to the penalty constraint term, when the Gaussian quadrature numerical integration technique is employed. The original penalty function formulation requires reduced numerical integration in order to avoid the possible over-constraint of the incompressibility conditions. This over-constraint problem can be resolved, however, if the modified penalty function is used. The present investigation also suggested an efficient method in dealing with the rigid elements involved in the computation. This method of rigid treatment, combined with the modified convergence criteria, provides fast convergence of the iterative solutions, thereby reducing the computing time.

The four nodal quadrilateral elements with bilinear velocity distributions were used throughout the present investigations. The discretization procedures change the minimum or stationary value problems into a set of simultaneous nonlinear equations. These equations were solved by Newton-Raphson's iterative technique. The time required in computation for each iteration depends on the machine and the number of elements and their arrangement. The number of iterations required to obtain the desired convergence solution depends on the problem itself, as well as on the initial guess provided. In order to reduce the computing time without sacrificing accuracy, coarser elements were used when the strain rate gradients are small, whereas finer elements were necessary for large gradients. In general, the required computing time is reasonable and the accuracy of the obtained solutions is satisfactory in comparison with the experimental results.

Both steady-state (extrusion and drawing) and non-steady-state (ring compression and forging) deformation problems were analyzed by using the present finite-element techniques. The non-steady-state problems were solved by a step-by-step deformation process in which the grid distortions and effective strains were obtained by incrementally adding the computed velocities and effective strain rates at every step. For the analysis of steady-state problems, instead of using the step-by-step analysis technique, the flow lines and corresponding effective strains were constructed at every iteration, the flow stresses changed accordingly, and the iterative procedures were repeated until the desired converging solution was achieved. Work-hardening material behavior, as well as the interfacial friction conditions, can also be treated efficiently.

The analysis of two-pass operations in extrusion and drawing processes was made by the present finite-element method, which reveals the effects of the previous deformation history on the flow patterns of the current pass. The deformation characteristics during the second pass were generally closer to those of non-work-hardening materials, in comparison with first-pass deformation, for both extrusion and drawing. The axial stress along the axis of extrusion and drawing was found to be greater in tension for the second pass than that during the first pass, suggesting an increasing possibility of center-burst formation in multipass processes.

For neutral flow problems such as ring compression and rolling, the boundary conditions along the die-workpiece interface are not well prescribed. The difficulties were resolved by assuming the velocity dependent interfacial frictions. The corresponding minimum principle and discretization formulations were made and applied to the problems of ring compression. The results revealed that the inner diameter changes of the ring specimen are highly dependent on the friction conditions. Although material properties appear to affect the geometry change, it is found, however, that their effects on the velocity and die pressure patterns are insignificant. A series of velocity patterns were also given, indicating the detailed material flow under the influence of friction conditions. The present results match well with the upper-bound solutions for small frictions, but differ greatly for large friction conditions, which indicates that most of the upper-bound solutions did not handle properly the situation of severe barreling and the formation of surface folding under conditions of large friction.

The closed-die forging problems were analyzed by further modification of the program for two extreme cases of perfect lubrication and sticking friction. The series of grid patterns and velocity distributions were presented and compared with the experimental observations. Results indicate that the forging process may be characterized by the stages of compression, filling, and extrusion. Each stage has its own deformation characteristics, as can be seen from the figures of rigid portions and velocity distributions. The forging loads and flash geometry obtained by the present analysis are very useful for the selection of a suitable geometry of the workpiece and for proper design and control of the forging processes.

The successful application of the present rigid-plastic finite-element method reveals a new avenue in the course of analysis of various metal-forming processes. Results obtained from this method are extremely valuable in preparing the workpiece, designing the equipment, controlling the process, and preventing product defects. Although the present work was conducted for rate-insensitive materials under room temperature operations, the modification of the present method to incorporate strain-rate and temperature effects is possible. This may require a new variational formulation, but the basic principles and the finite-element techniques remain the same. The present investigation employed the friction law of constant interfacial friction factor, but it is also possible to incorporate any other friction representations. Although further investigations are still required in order to solve complex problems with a minimum of computing time, it is appropriate to make the conclusion that the present rigid-plastic finite-element method is indeed an efficient and accurate method and is, therefore, a powerful tool for industrial applications.

REFERENCES

1. Thomsen, E. G., Yang, C. T., and Kobayashi, S., Mechanics of Plastic Deformation in Metal Processing, Macmillan, New York, 1963.

2. Johnson, W., and Mellor, P. B., Engineering Plasticity, Van Nostrand Reinhold Company, London, 1973.

3. Hoffman, O., and Sachs, G., Introduction to the Theory of Plasticity for Engineers, McGraw-Hill Book Co., New York, 1953.

4. Siebel, E., "The plastic forming of metals," translated by J. H. Hitchcock, reprinted from Steel, 43-48, October 16, 1933-May 7, 1934.

5. Hill, R., The Mathematical Theory of Plasticity, Clarendon Press, Oxford, 1950.

6. Lee, E. H., "The theoretical analysis of metal-forming problems in plane-strain," J. Appl. Mech. 19, 97-103, 1953.

7. Johnson, W., and Kudo, H., Mechanics of Metal Extrusion, Manchester University Press, 1962.

8. Hill, R., "On the state of stress in a plastic-rigid body at the yield point," Phil. Mag. 42, 868-875, 1951.

9. Zienkiewicz, O. C., The Finite-element Method, 3rd ed., McGraw-Hill Book Co. (London), 1977.

10. Strang, G., and Fix, G. J., An Analysis of the Finite-element Method, Prentice-Hall, Englewood Cliffs, N.J., 1973.

11. Tong, P., and Rosettos, J. N., Finite-element Method, MIT Press, Cambridge, Mass., 1977.

12. Lee, C. H., "Numerical analyses of the mechanics of plastic deformation problems," Ph.D. dissertation, University of California, Berkeley, 1970.

13. Lee, C. H., and Kobayashi, Shiro, "Analyses of axisymmetric upsetting and plane-strain side-pressing of solid cylinders by the finite-element method," Trans. ASME, J. of Engrg. for Ind. 93, 445-454, 1971.

14. Lee, C. H., and Kobayashi, Shiro, "Elastoplastic analysis of plane-strain and axisymmetric flat-punch indentation by the finite-element method," Int. J. Mech. Sci. 12, 349-370, 1970.

15. Lee, C. H., Iwasaki, H., and Kobayashi, S., "Calculation of residual stresses in plastic deformation processes," Trans. ASME, J. of Engrg. for Ind. 95, 282-291, 1973.

16. Lee, C. H., Masaki, S., and Kobayashi, Shiro, "Analysis of ball indentation," Int. J. Mech. Sci. 14, 417-426, 1972.

17. Lee, C. H., and Kobayashi, S., "New solutions to rigid-plastic deformation problems using a matrix method," Trans. ASME, J. of Engrg. for Ind. 95, 865-873, 1973.

18. Lee, C. H., and Kobayashi, S., "Deformation mechanics and workability in upsetting solid circular cylinders," Proc. North Amer. Metalworking Res. Conf., Hamilton, Canada, vol. 1, 185-204, May 1973.

19. Oh, S. I., and Kobayashi, S., "Workability of aluminum alloy 7075-T6 in upsetting and rolling," Trans. ASME, J. Engrg. for Ind., 800-806, 1976.

20. Lee, S. H., and Kobayashi, S., "Rigid-plastic analysis of bore expanding," Proc. 15th Int. Mech. Tool Design and Res. Conf., 561, 1975.

21. Kim, J. H., and Kobayashi, S., "Deformation analysis of axisymmetric sheet metal forming processes by the rigid-plastic finite element method," in Mechanics of Sheet Metal Forming (D. P. Koistinen and N. M. Wang, eds.), Plenum Press, New York, pp. 341-362, 1978.

22. Price, J. W. H., "A study of dieless drawing and isothermal forming," Ph.D. dissertation, Imperial College, London, 1977.

23. Price, J. W. H., and Alexander, J. M., "A study of the isothermal forming or creep forming of a titanium alloy," 4th North Amer. Metalworking Res. Conf., Battelle, Columbus, Ohio, 1976.

24. Price, J. W. H., and Alexander, J. M., "The finite-element analysis of two high temperature metal deformation processes," 2nd Int. Symp. on Finite-element Methods in Flow Problems, Santa Margherita, Ligure, Italy, 715-720, 1976.

25. Zienkiewicz, O. C., and Godbole, P. N., "Flow of plastic and visco-plastic solids with special reference to extrusion and forming processes," Int. J. Num. Meth. in Engng. 8, 3-16, 1974.

26. Zienkiewicz, O. C., and Godbole, P. N., "Viscous, incompressible flow with special reference to non-Newtonian (plastic) fluids," in Chapter 2, Finite Elements in Fluids (R. H. Gallagher et al., eds.), Wiley, New York, 1975.

27. Zienkiewicz, O. C., "Visco-plasticity, plasticity, creep, and visco-plastic flow (problems of small, large, and continuing deformation)," Int. Conf. Computational Methods in Nonlinear Mechanics, Texas, 1974.

28. Washizu, K., *Variational Methods in Elasticity and Plasticity*, Pergamon Press, New York, 1950.

29. Shah, S. N., "Numerical analysis of metal-forming processes," Ph.D. dissertation, University of California, Berkeley, 1975.

30. Kobayashi, S., Lee, C. H., and Oh, S. I., "Workability theory of materials in plastic deformation processes," USAF Technical Report AFML-TR-73-192, 1973.

31. Zienkiewicz, O. C., and Godbole, P. H., "A penalty function approach to problems of plastic flow of metals with large surface deformation," J. Strain Analysis 10, 180-181, 1975.

32. Bathe, K.-J., and Wilson, E. L., *Numerical Methods in Finite-element Analysis*, Prentice-Hall, Englewood Cliffs, N.J., 1976.

33. Dahlquist, Germund, and Björck, Åke, *Numerical Method*, translated by Ned Anderson, Prentice-Hall, Englewood Cliffs, N.J., 1974.

34. Oden, T. J., *Finite Elements of Nonlinear Continua*, McGraw-Hill Book Co., New York, 1972.

35. Rall, L. B., *Computational Solution of Nonlinear Operator Equations*, Wiley, New York, 1969.

36. Cauchy, A. L., "Méthode générale pour la résolution des systémes d'équations simultanees," *C. R. Acad. Sci. Paris* *25*, 536-538.

37. Fletcher, R., and Reeves, C. M., "Function minimization by conjugate gradients," *Computer J*. *7*, 149-154.

38. Daniel, J. W., "The conjugate gradient method for linear and nonlinear operator equations," *SIAM J. Numerical Anal*. *4*, 10-25.

39. DePierre, V., and Gurney, F., "A method for determination of constant and varying friction factors during ring compression tests," *Trans. ASME, J. of Lubrication Technology*, 482-488, July 1974.

40. Chen, C. C., Oh, S. I., and Kobayashi, Shiro, "Ductile Fracture in Axisymmetric Extrusion and Drawing," AFML-TR-77-97, June 1977.

41. Shabaik, A. H., and Thomsen, E. G., "Investigation of the application of the visioplasticity methods of analysis to metal deformation processes," Final Report, Part II, Department of the Navy, 1968.

42. Kunogi, M., "On plastic deformation of hollow cylinders under axial compressive loading," *J. of Scientific Res. Inst*. *2*, 1954 (in Japanese).

43. Kudo, H., "An analysis of plastic compressive deformation of lamella between rough places by energy method," Proc. of the 5th Japan Nat'l Congr. for Appl. Mech., 75-78, 1955.

44. Avitzur, B., "Forging of hollow disks," Israel J. of Tech. 2, 295, 1964.

45. Hawkyard, J. B., and Johnson, W., "An analysis of the changes in geometry of a short hollow cylinder during axial compression," Int. J. Mech. Sci. 9, 163, 1967.

46. Male, A. T., and Cockroft, M. G., "A method for the determination of the coefficient of friction of metals under conditions of bulk plastic deformation," J. of the Inst. of Metals 93, 38, 1964-65.

47. Male, A. T., and DePierre, V., "The validity of mathematical solutions for determining friction from the ring compression test," J. of Lubrication Technology, 389-397, July 1970 (also AFML Technical Report AFML-TR-69-28).

48. Sawl, G., Male, A. T., and DePierre, V., "A new method for determination of material flow stress values under metalworking conditions," AFML Technical Report, AFML-TR-70-19, 1970.

49. Avitzur, B., "Bulge in hollow disk forging," AFML Technical Report, AFML-TR-69-261, 1969.

50. DePierre, V., Gurney, F., and Male, A. T., "Mathematical calibration of the ring test with bulge formulation," AFML Technical Report, AFML-TR-72-37, 1972.

51. Liu, J. Y., "An analysis of deformation characteristics and interfacial friction condition in simple upsetting of rings," Trans. ASME, J. of Engrg. for Ind. 94, 1149-1156, 1972.

52. Lee, C. H., and Altan, T., "Influence of flow stress and friction upon metal flow in upset forging of rings and cylinders," Trans. ASME, J. of Engrg. for Ind. 94, 775-782, 1972.

53. Jain, S. C., and Bramley, A. N., "Speed and frictional effects in hot forging," Proc. Inst. Mech. Engrs. 182(39), pt. 1, 783-798, 1967-68.

54. Kobayashi, S., Lee, C. H., and Jain, S. C., "Analytic prediction of defects occurrence in simple and complex forging," Technical Report, AFML-TR-70-90, 1970.

55. Lahoti, G. D., and Kobayashi, S., "On Hill's general method of analysis for metalworking processes," Int. J. Mech. Sci. 16, 521, 1974.

56. Matsumoto, H., Oh, S. I., and Kobayashi, S., "A note on the matrix method for rigid-plastic analysis of ring compression," Proc. of the 18th MTDR Conf., London, pp. 3-9, September 1977.

57. Prandtl, L., "Anwendungsbeispiele zu einem Henckyschen Satz über plastische Gleichgewicht," Z. Angew. Math. Mech. 3, 401-406, 1923.

58. Hill, R., Lee, E. H., and Tupper, S. J., "A method of numerical analysis of plastic flow in plane-strain and its application to the compression of a ductile material between rough plates," Trans. ASME, J. Appl. Mech. 18(73), 46-52, 1951.

59. Green, A. P., "A theoretical investigation of the compression of a ductile material between smooth flat dies," Phil. Mag. 42, 900, 1951.

60. Alexander, J. M., "The effect of Colomb friction in the plane-strain compression of plastic-rigid material," J. Mech. Phys. Solids 3, 233-245, 1955.

61. Bishop, J. F. W., "On the effect of friction on compression and indentation between flat dies," J. Mech. Phys. Solids 6, 132-144, 1958.

62. Nadai, A., "The forces required for rolling steel strips under tension," Trans. ASME, J. Appl. Mech. 6(61), 1939.

63. Sachs, G., von W. Eisbein, Mitwirkung, Kuntze, W., and Lincicus, W., "Spanlose Formung der Metalle," Mitt. Deut. Material Prufungsanstalten, Supplement 16, K. W. Inst. Metall. Forschung, Julius Springer, Berlin, Germany, p. 93, 1931.

64. Schroeder, W., and Webster, D. A., "Press-forging thin sections: Effect of friction, area, and thickness on pressure required," Trans. ASME, J. Appl. Mech. 16(71), 289-294, 1949.

65. Kobayashi, S., Herzog, R., Lapsley, J. T. Jr., and Thomsen, E. G., "Theory and experiment of press forging axisymmetric parts of aluminum and lead," Trans. ASME, Series B, J. of Engrg. for Ind. 81, 228-238, 1959.

66. Kobayashi, S., and Thomsen, E. G., "Approximate solutio s to a problem of press forging," Trans. ASME, Series B, J. of Engrg. for Ind. 81, 217-227, 1959.

67. Altan, T., and Fiorentino, R. J., "Prediction of loads and stresses in closed-die forging," Trans. ASME, J. of Engrg. for Ind., Series B, 93(2), 477-484, 1971.

68. Akgerman, N., and Altan, T., "Modular analysis of geometry and stresses in closed-die forging: application to a structural part, Trans. ASME, J. of Engrg. for Ind., Series B, 94, 1025-1035, 1972.

69. Johnson, W., "Over-estimates of load for some two-dimensional forging operations," Proc. 3rd U.S. Congr. Appl. Mech., ASME (New York), pp. 571-579, 1958.

70. Kudo, H., "Studies on forging and extrusion process, I," Kokenshuho University, Tokyo, vol. 1, p. 37, 1958.

71. Schey, J. A., "Principles of forging design," American Iron and Steel Institute, New York, 1964.

72. Spies, K., "The preforms in closed-die forging and their preparation by reduced rolling," Ph.D. dissertation, Technical University. Hanover, Germany, 1957 (in German).

73. Stepanski, L. G., "Estimation of loads and strains in processes of metal treatment under pressure," Kuznechno-Shtampovochnoe proizvodstro 3, 1959 (in Russian).

74. Goon, G. Ya., "Conform transformations and variational methods in the theory of metal treatment under pressure," Ph.D. dissertation, Sverdlovsk, 1965 (in Russian).

75. Gubkin, S. I., "Theory of fundamentals of metal treatment under pressure," Moscow, 1947 (in Russian).

76. Semenov, E. I., "Investigation of closed-die forging and extrusion," Ph.D. dissertation, 1973 (in Russian).

77. Kondratenko, V. G., "Investigation of strains and stresses in closed-die forging," Candidate of Technical Sciences Dissertation, Moscow, 1971 (in Russian).

78. Mertens, K. K., "Investigation of strains and loads in the last operation of press forging," Candidate of Technical Science Dissertation, Leningrad, 1967 (in Russian).

79. Kasuza, Y., Tsutumi, S., and Saiki, H., "Material flow in sunken forging dies," *Sosei-to-kako* *14*, 876, 1973; *Sosei-to-kako* *15*, 147, 1974.

80. Lyapunov, N. I., and Kobayashi, Shiro, "Metal flow in plane-strain closed-die forging," Proc. of 5th North Amer. Metalworking Res. Conf., p. 114, May 1977.

*U.S.Government Printing Office: 1979 — 657-084/301